

**CHARACTERIZATION OF Sn-Bi-Co LOW TEMPERATURE SOLDER
ALLOY**

LINA SYAZWANA BINTI KAMARUZZAMAN

**FACULTY OF ENGINEERING
UNIVERSITI MALAYA
KUALA LUMPUR
2023**

CHARACTERIZATION OF Sn-Bi-Co LOW TEMPERATURE
SOLDER ALLOY

LINA SYAZWANA BINTI KAMARUZZAMAN

DISSERTATION SUBMITTED IN FULFILMENT OF THE
REQUIREMENTS FOR THE DEGREE OF MASTER OF
ENGINEERING SCIENCE

FACULTY OF ENGINEERING
UNIVERSITI MALAYA
KUALA LUMPUR

2023

UNIVERSITI MALAYA

ORIGINAL LITERACY WORK DECLARATION

Name of Candidate: Lina Syazwana binti Kamaruzzaman

Matric No: 17143728/2

Name of Degree: Master of Engineering Science

Title of Project Paper/Research Report/Dissertation/Thesis ("this Work"):

Characterization of Sn-Bi-Co Low Temperature Solder Alloy

Field of Study: Engineering Material

I do solemnly and sincerely declare that:

- (1) I am the sole author/writer of this Work;
- (2) This Work is original;
- (3) Any use of any work in which copyright exists was done by way of fair dealing and for permitted purposes and any excerpt or extract from, or reference to or reproduction of any copyright work has been disclosed expressly and sufficiently and the title of the Work and its authorship have been acknowledged in this Work;
- (4) I do not have any actual knowledge nor do I ought reasonably to know that the making of this work constitutes an infringement of any copyright work;
- (5) I hereby assign all and every rights in the copyright to this Work to the University of Malaya ("UM"), who henceforth shall be owner of the copyright in this Work and that any reproduction or use in any form or by any means whatsoever is prohibited without the written consent of UM having been first had and obtained;
- (6) I am fully aware that if in the course of making this Work I have infringed any copyright whether intentionally or otherwise, I may be subject to legal action or any other action as may be determined by UM.

Candidate's Signature

Date: 06/04/2023

Subscribed and solemnly declared before,

Witness's Signature

Date: 6/4/2023

Name:

Designation:

CHARACTERIZATION OF Sn-Bi-Co LOW TEMPERATURE SOLDER

ALLOY

ABSTRACT

Sn-Bi solder had Bi-rich phase that brittle and prone to fracture during service. As the result, the excessive hardness and brittleness of Sn-Bi solder alloy could easily deteriorate the solder mechanical properties which then strongly influence the solder joint and packaging components continuing reliability. Systematic investigation on the impact of alloying Co element using flux doping technique on both microstructure and mechanical properties of Sn-58Bi solder alloy and the study of the effect of Sn-58Bi-Co/Cu solder joints microstructure when varying aging duration are conducted. The melting temperature of the solder are evaluated using differential scanning calorimeter (DSC) while the solder microstructure and IMC is characterized by scanning electron microscope (SEM), energy dispersive X-ray spectroscopy (EDX) and build-in image analyser. The crystalline structure of the solder was analysed using XRD. Tensile test and Vickers hardness test used to characterize the solder mechanical properties. All characterization of the Sn-Bi-Co solder are assessed and correlated with Sn-Bi solder to note to any enhancement. The microstructure of all Sn-58Bi-xCo solders did not show significant different compared to Sn-58Bi solder. Sn-58Bi-1.5Co solder shown excellence mechanical properties with 60.29 ± 0.18 MPa tensile strength and 19.52 ± 0.47 HV microhardness value. After 56 days of thermal aging, the IMC layer of Sn-58Bi-xCo/Cu solder joints become flattening. It is highly anticipated that this new Sn-Bi-Co alloy can be applied in low temperature soldering and heat sensitive electronic devices, thus replacing lead-containing solder alloy.

Keywords: Lead-free solder, Sn-Bi based solder, microstructure properties, tensile properties and thermal aging.

PENCIRIAN PATERI ALOI Sn-Bi-Co BERSUHU RENDAH

ABSTRAK

Bahagian yang kaya dengan Bi dalam aloi pateri Sn-Bi bersifat rapuh dan terdedah kepada keretakan semasa penggunaannya. Akibatnya, kekerasan dan kerapuhan aloi pateri Sn-Bi yang berlebihan menyebabkan kemerosotan sifat mekanikal sambungan pateri yang lebih mudah seterusnya menjejaskan kebolehpercayaan komponen sambungan dan pembungkusan pateri itu dalam jangka masa panjang. Selain itu, apabila aloi pateri Sn-Bi disertakan dengan substrat Cu, terdapat pengasingan Bi di antara muka Cu/Cu₃Sn. Perkembangan aloi pateri Sn-Bi-Co yang baru dijangka dapat menyelesaikan masalah yang timbul disebabkan oleh bahagian yang kaya dengan Bi. Oleh itu, penyiasatan sistematik mengenai kesan penambahan elemen aloi Co terhadap kedua-dua sifat mikrostruktur dan mekanikal aloi pateri Sn-58Bi serta kajian mengenai kesan perubahan tempoh penuaan terhadap kekuatan tegangan sambungan pateri Sn-58Bi-Co/Cu dijalankan. Suhu lebur dan pepejal pateri dinilai menggunakan *differential scanning calorimeter (DSC)* manakala mikrostruktur pateri dikaji menggunakan *scanning electron microscope (SEM)*, *energy dispersive X-ray spectroscopy (EDX)* dan penganalisis imej binaan. Struktur habluran pateri dikaji menggunakan *x-ray diffraction (XRD)*. Ujian tegangan dan ujian kekuatan Vickers digunakan untuk mengkaji sifat mekanikal pateri. Semua perincian pateri Sn-Bi-Co dinilai dan dibandingkan dengan pateri Sn-Bi untuk menilai sebarang penambahbaikannya. Mikrostruktur kesemua pateri Sn-58Bi-xCo juga tidak menunjukkan perubahan ketara dibandingkan dengan pateri Sn-58Bi. Pateri Sn-58Bi-1.5Co menunjukkan sifat-sifat mekanikal yang terbaik dengan 60.29 ± 0.18 MPa kekuatan tegangan dan 19.52 ± 0.47 HV nilai kekuatan mikro. Selepas 56 hari penuaan terma, sabatian antara logam sambungan pateri Sn-58Bi-xCo/Cu menjadi kearah perataan. Adalah sangat dijangkakan agar aloi baru Sn-Bi-Co ini boleh digunakan dalam

pematerian suhu rendah dan peranti elektronik sensitif haba, kemudian mampu menggantikan aloi pateri yang mengandungi plumbum.

Kata kunci: Pateri bebas plumbum, aloi berasaskan Sn, sifat-sifat mikrostruktur, sifat-sifat ketegangan dan penuaan terma.

Universiti Malaya

ACKNOWLEDGEMENT

I would like to thank everyone who had help me throughout this research journey. My deepest appreciation to my supervisor, Dr. Goh Yingxin for her vital advice, guidance and vast patience throughout the progress. Besides I would also like to prompt my gratitude to my loving parent and friends who had helped and reassurance me throughout the completion of my research. Special thanks to Ms. Norzirah, Ms. Hartini, Ms. Sarimaniza, Mr. Mohd Nazarul Zaman, Mr. Zam, Mr. Mohd Asri, Mr. Taufik, Ms. Nur Kamisah, Ms. Nik Fasihah, Mr. Mohamad Shukri, Miss Lee Ee Lynn, Miss Goh Yi Sing and Mr. Zhou Ding for their kind helped and guidance to smoothen my research progress. Lastly, a big thanks to the financial support through the project GPF046A-2019.

Universiti Malaysia

TABLE OF CONTENT

| | |
|---|------|
| ORIGINAL LITERACY WORK DECLARATION | ii |
| ABSTRACT | iii |
| ABSTRAK | iv |
| ACKNOWLEDGEMENT | vi |
| TABLE OF CONTENT | vii |
| List of Figures | xi |
| List of Tables | xv |
| List of Symbols and Abbreviations | xvi |
| List of Appendices | xvii |
| CHAPTER 1: INTRODUCTION | 1 |
| 1.1 Background | 1 |
| 1.2 Problem Statement | 4 |
| 1.3 Objectives | 5 |
| 1.4 Research Outline | 5 |
| CHAPTER 2: LITERATURE REVIEW | 7 |
| 2.1 Lead-free Solder | 7 |
| 2.1.1 Binary and Ternary Composition Solder | 8 |
| 2.2 Sn-based Solder Properties | 9 |

| | |
|--|-----------|
| 2.2.1 Phase Diagram and Melting Temperature | 10 |
| 2.2.2 Microstructure Properties | 17 |
| 2.2.3 Mechanical Properties..... | 23 |
| 2.2.4 Interfacial and Aging Studies | 28 |
| 2.2.5 Summary..... | 38 |
| 2.3 Method of Improving Solder Performances | 41 |
| 2.3.1 Flux Doping Technique | 41 |
| 2.3.2 Directional Solidified Method | 41 |
| 2.3.3 Powder Metallurgy Method..... | 41 |
| 2.4 Effect of Alloying Element on Lead-Free solder | 42 |
| 2.4.1 Properties and Criteria of Alloying Selection..... | 42 |
| 2.4.2 Bismuth, Bi..... | 45 |
| 2.4.3 Cobalt, Co | 46 |
| CHAPTER 3: METHODOLOGY..... | 47 |
| 3.1 Introduction | 47 |
| 3.2 Sample Preparation..... | 48 |
| 3.2.1 Thermal Characterisation, Microstructure Characterisation, Composition and Crystalline Structure Studies, Interfacial Studies, and Vickers Hardness Test | 50 |
| 3.2.2 Tensile Test..... | 51 |
| 3.3 Sample Characterisation..... | 51 |
| 3.3.1 Thermal Properties..... | 51 |
| 3.3.2 Microstructure Properties | 52 |

| | |
|---|-----------|
| 3.3.3 Composition and Crystalline Structure Studies | 52 |
| 3.3.4 Mechanical Properties..... | 53 |
| 3.3.5 Interfacial and Aging Studies | 54 |
| CHAPTER 4: RESULTS AND DISCUSSION..... | 58 |
| 4.1 Introduction | 58 |
| 4.2 Thermal Characterisation | 58 |
| 4.3 Microstructure Properties | 60 |
| 4.4 Composition and crystalline structure studies | 66 |
| 4.5 Mechanical Properties | 67 |
| 4.5.1 Tensile Properties | 67 |
| 4.5.2 Fractography Studies | 71 |
| 4.5.3 Microhardness..... | 76 |
| 4.6 Interfacial and Aging Studies | 78 |
| 4.6.1 Interfacial Studies | 78 |
| 4.6.2 Thermal Aging Studies | 82 |
| CHAPTER 5: CONCLUSION AND RECOMMENDATIONS | 89 |
| 5.1 Conclusion..... | 89 |
| 5.2 Recommendations | 90 |
| REFERENCES | 92 |
| APPENDIX A: List of Publications and Paper Presented | 98 |
| Published research paper..... | 98 |
| Published review paper | 99 |

| | |
|--|-----------|
| Participating and presented in Virtual Centre of Advanced Materials (CAM) Postgraduate Symposium 2021 | 99 |
| APPENDIX B: Raw data from differential scanning calorimeter (DSC) curved..... | 101 |
| APPENDIX C: X-ray diffraction analysis (XRD) graph of cobalt powder..... | 102 |
| APPENDIX D: Stress-strain plot raw data | 103 |
| APPENDIX E: Vickers hardness indentation images..... | 105 |
| APPENDIX F: Pictures of machines/lab equipment's used | 109 |

Universiti Malaya

LIST OF FIGURES

| | |
|--|----|
| Figure 2.1: Ag-Sn phase diagram (Qu et al., 2013) | 11 |
| Figure 2.2: Sn-Ag-Cu ternary diagram (Liang, Dariavach & Shangguan, 2007)..... | 12 |
| Figure 2.3: Zn-Sn phase diagram (Gornakova et al., 2009)..... | 13 |
| Figure 2.4: In-Sn phase diagram (Brittles et al., 2015)..... | 14 |
| Figure 2.5: (a) DSC curves of eutectic Sn-Bi solder and (b) Binary phase diagram of Sn-Bi solder (Liu et al., 2016) | 15 |
| Figure 2.6: Co-Sn-Bi ternary diagram (Hu et al., 2022) | 17 |
| Figure 2.7: As-cast SEM microstructure of (a) Sn-3.0Ag; (b) Sn-3.5Ag; (c) Sn-4.0Ag and (d) Sn-5.0Ag solders (Tunthawiroon & Kanlayasiri, 2019) | 18 |
| Figure 2.8: SEM image cross sectional sample of bulk microstructure of (a) as-received solder and (b) after 1 x reflow of SAC105 (Leong & Haseeb, 2016)..... | 19 |
| Figure 2.9: SEM image of Sn-9Zn solder alloy (Ren, Wilding & Collins, 2016)..... | 20 |
| Figure 2.10: Sn-52In solder matrix microstructure (Li et al., 2016a)..... | 20 |
| Figure 2.11: SEM microstructure image of (a) eutectic Sn-Bi solder bulk, (b) magnified eutectic Sn-Bi solder bulk, (c) Sn element mapping and (d) Bi element mapping (Liu et al., 2016)..... | 22 |
| Figure 2.12: (a) Sn-58Bi solder alloy microstructure (Chen et al., 2016), (b) Eutectic Sn-58Bi/Cu solder lamellar structure (Ren, Wilding & Collins, 2016) | 22 |
| Figure 2.13: SEM image of Sn-58Bi solder alloy fracture surface at (a) 25°C, (b) 125°C, (c) 0.0004 s ⁻¹ strain rate and (d) 0.05 s ⁻¹ strain rate (Chen et al., 2016)..... | 27 |
| Figure 2.14: Bi-Cu-Sn ternary system (“Bi-Cu-Sn System”, n.d.) | 30 |
| Figure 2.15: Intermetallic layer morphologies of (a) Sn-3.0Ag; (b) Sn-3.5Ag; (c) Sn-4.0Ag and Sn-5.0Ag solders with Cu substrate (Tunthawiroon & Kanlayasiri, 2019) .. | 32 |
| Figure 2.16: SAC (a) cross sectional micrograph after 1 x reflow and (b) cross sectional image after aging at 150 °C for 720 h (Leong & Haseeb, 2016) | 33 |

| | |
|---|----|
| Figure 2.17: Microstructure of Sn-52In/Cu (a) as-soldered interface and (b) after aging at 55 °C for 480 hours interface (Li et al., 2016a). | 35 |
| Figure 2.18: SEM images of reflowed Sn-58Bi/Cu solder joint at 160 °C for 10 s (a) before and (b) after aged at 30 days (Wang, Li & Huang, 2017). | 37 |
| Figure 3.1: Methodology flow chart | 48 |
| Figure 3.2: Pictures of flux doping technique sample preparation process | 49 |
| Figure 3.3: Flux doping technique schematic diagram | 50 |
| Figure 3.4: Schematic diagram of tensile test specimens | 51 |
| Figure 3.5: Samples for microstructure observation..... | 52 |
| Figure 3.6: Samples of before and after tensile test..... | 54 |
| Figure 3.7: Samples for pure Sn-58Bi/Cu and Sn-58Bi-Co/Cu solder joint intermetallic studies and thermal aging studies..... | 55 |
| Figure 3.8: Schematic diagram of reflow process..... | 56 |
| Figure 3.9: Schematic diagram of aging process | 57 |
| Figure 4.1: DSC curve with average melting temperature of Sn-58Bi-xCo solder alloy | 59 |
| Figure 4.2: Average melting temperature of Sn-58Bi-xCo solder alloy..... | 59 |
| Figure 4.3: SEM images of (a) Sn-58Bi, (b) Sn-58Bi-1.0Co, (c) Sn-58Bi-1.5Co and (d) Sn-58Bi-2.0Co solder alloy..... | 61 |
| Figure 4.4: Element mapping of Sn-58Bi-1.0Co solder alloy. | 62 |
| Figure 4.5: Element mapping of Sn-58Bi-1.5Co solder alloy | 62 |
| Figure 4.6: Element mapping of Sn-58Bi-2.0Co solder alloy | 63 |
| Figure 4.7: Line scanning of Sn-58Bi-1.0Co solder alloy | 64 |
| Figure 4.8: Line scanning of Sn-58Bi-1.5Co solder alloy | 64 |
| Figure 4.9: Line scanning of Sn-58Bi-2.0Co solder alloy | 65 |
| Figure 4.10: XRD plot of pure Sn-58Bi solder and Sn-58Bi-xCo solder | 67 |

| | |
|--|----|
| Figure 4.11: Modulus of elasticity of pure Sn-58Bi solder and Sn-58Bi-xCo (x = 1.0, 1.5 and 2.0) solder..... | 70 |
| Figure 4.12: Tensile strength of pure Sn-58Bi solder and Sn-58Bi-xCo (x = 1.0, 1.5 and 2.0) solder..... | 71 |
| Figure 4.13: (a) Side view and (b) cross-section view of fractured surface observations position..... | 72 |
| Figure 4.14: SEM images of pure Sn-58Bi solder tensile fractured surface side view at (a) 0.0005 s ⁻¹ , (b) 0.001 s ⁻¹ and 0.0025 s ⁻¹ strain rates..... | 73 |
| Figure 4.15: SEM images of pure Sn-58Bi solder tensile fractured surface cross-section view at (a) 0.0005 s ⁻¹ , (b) 0.001 s ⁻¹ and 0.0025 s ⁻¹ strain rates | 74 |
| Figure 4.16: SEM images of tensile fractured surface side view of (a) pure Sn-58Bi, (b) Sn-58Bi-1.0Co, (c) Sn-58Bi-1.5Co and (d) Sn-58Bi-2.0Co solders at 0.0005 s ⁻¹ strain rate..... | 75 |
| Figure 4.17: SEM images of tensile fractured surface cross-section view of (a) pure Sn-58Bi, (b) Sn-58Bi-1.0Co, (c) Sn-58Bi-1.5Co and (d) Sn-58Bi-2.0Co solders at 0.0005 s ⁻¹ strain rate..... | 76 |
| Figure 4.18: SEM images of (a) pure Sn-58Bi/Cu solder, (b) Sn-58Bi-1.0Co/Cu solder, (c) Sn-58Bi-1.5Co/Cu solder and (d) Sn-58Bi-2.0Co/Cu solder at 6000× magnification | 79 |
| Figure 4.19: Element mapping of (a) pure Sn-58Bi/Cu, (b) Sn-58Bi-1.0Co/Cu, (c) Sn-58Bi-1.5Co/Cu and (d) Sn-58Bi-2.0Co/Cu solder joint | 80 |
| Figure 4.20: IMC thickness of pure Sn-58Bi/Cu and Sn-58Bi-Co/Cu solder joint after thermal aging for 0, 28, and 56 day(s) | 84 |
| Figure 4.21: SEM images of Sn-58Bi-1.5Co/Cu solder joint after thermal aging for (a) 0, (b) 14, (c) 28, (d) 42, (e) 56 and (f) 70 day(s)..... | 85 |

| | |
|--|-----|
| Figure 4.22: IMC thickness of Sn-58Bi-1.5Co after thermal aging for 0, 14, 28, 42, 56 and 70 day(s)..... | 86 |
| Figure 4.23: Element mapping of Sn-58Bi-1.5Co/Cu solder joint after thermal aging for (a) 0, (b) 28, (c) 56 and (d) 70 day(s)..... | 87 |
| Figure A.1: 1 st page of published research paper..... | 98 |
| Figure A.2: 1 st page of published review paper..... | 99 |
| Figure A.3: Abstract for Centre of Advanced Materials (CAM) postgraduate symposium 2021..... | 100 |
| Figure A.4: Centre of Advanced Materials (CAM) postgraduate symposium 2021 participating certificate..... | 100 |
| Figure C.1: XRD graph of cobalt powder..... | 102 |
| Figure F.1: Pictures of lab apparatus used for sample preparation and observation..... | 109 |
| Figure F.2: Pictures of machine used to analyse the samples..... | 110 |

LIST OF TABLES

| | |
|---|-----|
| Table 2.1: Sn-1.0Ag-0.5Cu and Sn-3.0Ag-0.5Cu solders properties (Cheng, Huang & Pecht, 2017)..... | 23 |
| Table 4.1: Average amount of Co detected from the line scanning..... | 66 |
| Table 4.2: Tensile properties of Sn-58Bi solder alloy at different strain rates | 68 |
| Table 4.3: Average microhardness values | 77 |
| Table 4.4: Average IMC thickness of Sn-58Bi-Co with Cu substrates | 81 |
| Table B.1: Melting temperature of pure Sn-58 solder and Sn-58Bi-xCo (x=1.0, 1.5 and 2.0) solders raw data | 101 |
| Table D.1: Pure Sn-58Bi solder elongation, modulus of elasticity and tensile strength raw data | 103 |
| Table D.2: Sn-58Bi-1.0Co solder modulus of elasticity and tensile strength raw data | 103 |
| Table D.3: Sn-58Bi-1.5Co solder modulus of elasticity and tensile strength raw data | 104 |
| Table D.4: Sn-58Bi-2.0Co solder modulus of elasticity and tensile strength raw data | 104 |
| Table E.1: 1 st and 2 nd image of Vickers hardness indentation on the solder surface | 105 |
| Table E.2: 3 rd and 4 th image of Vickers hardness indentation on the solder surface | 106 |
| Table E.3: 5 th image of Vickers hardness indentation on the solder surface | 107 |
| Table E.4: Pure Sn-58Bi solder hardness value raw data | 107 |
| Table E.5: Sn-58Bi-1.0Co solder hardness value raw data..... | 108 |
| Table E.6: Sn-58Bi-1.5Co solder hardness value raw data..... | 108 |
| Table E.7: Sn-58Bi-2.0Co solder hardness value raw data..... | 108 |

LIST OF SYMBOLS AND ABBREVIATIONS

| | | |
|--------------------------------|---|---|
| Sn | : | Tin |
| Bi | : | Bismuth |
| Co | : | Cobalt |
| Sn-Bi | : | Tin-bismuth |
| Sn-Bi-Co | : | Tin-bismuth-cobalt |
| Cu | : | Copper |
| Sn-Bi-Co/Cu | : | Tin-bismuth-cobalt solder and copper substrate |
| DSC | : | Differential scanning calorimeter |
| SEM | : | Scanning electron microscope |
| EDX | : | Energy dispersive X-ray spectroscope |
| IMC | : | Intermetallic compound |
| RoHs | : | Restriction of Hazardous Substance |
| WEEE | : | Waste from Electrical and Electronics Equipment |
| wt. % | : | Weight percentage |
| EDM | : | CNC wire electric discharge machining |
| H ₂ SO ₄ | : | Sulphuric acid |
| vol. % | : | Volume percentage |
| CAM | : | Centre of Advanced Materials |
| JCPDS | : | Joint Committee on Powder Diffraction Standards |
| XRD | : | X-ray Diffraction |

LIST OF APPENDICES

| | |
|--|-----|
| APPENDIX A: List of Publications and Paper Presented | 98 |
| APPENDIX B: Raw data from differential scanning calorimeter (DSC) curved | 101 |
| APPENDIX C: X-ray diffraction analysis (XRD) graph of cobalt powder..... | 102 |
| APPENDIX D: Stress-strain plot raw data | 103 |
| APPENDIX E: Vickers hardness indentation images..... | 105 |
| APPENDIX F: Pictures of machines/lab equipment's used | 109 |

Universiti Malaysia

CHAPTER 1: INTRODUCTION

1.1 Background

Lead-free Sn-based solder alloy has been actively studied to replace lead-containing solder alloy. Lead-containing solder alloys are known to cause health and environmental issues due to high toxicity possess by lead element where the improper handling and decomposition of high toxicity element could cause harmful effect on environment safety and human health.

Sn-Bi solder alloy is one of the alternatives gaining considerable attention among researchers due to its low melting temperature, satisfying tensile strength, intense creep resistance, good joint strength, and high hardness. Nonetheless, Sn-Bi solder alloy have few flaws which need to be further studied for improvement. Sn-Bi solder have poor ductility and thermo-mechanical properties while easily segregate the solder joint during service. These advantages caused the Sn-Bi solder to have much finite application in low soldering compared to Sn-Ag-Cu solder. Application of Sn-Bi solder narrowed towards low soldering applications which does not include in drop-shock and thermal cycling performance (Ribas et al., 2017).

At low temperatures, Sn-Bi solder alloy has huge issue when high strain rates are applied and also led to poor ductility (Maruya et al., 2017). This also infers that Sn-Bi solder alloy is profoundly reliant to strain rate (Chen et al., 2016). Even the ductility of Sn-Bi solder alloy is weaker despite having more prominent strength compared to Sn-Ag-Cu solder alloy (Wang et al., 2017). Then, regardless of enhancing the Sn-Bi solder mechanical properties, the present of Bi element in the solder composition caused coarsening and embrittlement (Wang et al., 2017; Mokhtari & Nishikawa, 2016). The brittle nature of Bi element also influences the solder mechanical properties by segregating at the solder joint (Yang et al., 2019; Mokhtari & Nishikawa, 2016). These

Most recommended techniques that could enhance Sn-Bi solder alloy mechanical properties are by alloying additional element such as Al, Zn, In, Ag and Cu in the Sn-Bi solder alloy composition (Yang et al., 2020; Ribas et al., 2017; Silva et al., 2017). Yang et al. likewise expressed that the eutectic Sn-Bi solder alloy can maintained its low melting temperature even by added some small amount of alloying element in the Sn-Bi solder alloy composition (Yang et al., 2020). Sn-58Bi solder melting temperature was 139 °C (Liu & Tu, 2020; Yang et al., 2016). By alloying Zn, Al and Ag, respectively into Sn-58Bi solder, the melting temperature of Sn-58Bi-0.7Zn, Sn-58Bi-3Al and Sn-58Bi-0.5Ag were 142.0 °C, 136.3 °C and 138.2 °C, respectively (Yang et al., 2016). Liu, Y., The melting temperature of Sn-58Bi with 2 wt.% of Al also slightly increased by several degree (Liu & Tu, 2020). These imply that depending on the minor alloying elements amount added into Sn-Bi solder, the solder melting temperature could raise or lowered by ± 10 °C.

A eutectic Sn-Bi solder microstructure consist of typical eutectic lamellar structure of Sn-rich and Bi-rich phase, respectively (Wang et al., 2019; Chen et al., 2016). Alam et al. reported that increasing amount of Cu alloying addition into Sn-56.5Bi solder results in refinement of Sn-rich and Bi-rich regions (Alam et al., 2019). The lamellar spacing of Sn-Bi-Cu solder becoming refined (Alam et al., 2019). 0.5 wt. % of Sb also refine the Sn-58Bi solder grain size (Kang et al., 2021). Then, 2 wt. % addition of Ga into Sn-58Bi and Sn-40Bi solder changed the Sn-rich dendrites morphology from unfaceted to faceted (da Silva et al., 2019). Hu et al. stated that 0.5 wt. % addition of Al₂O₃ particles into Sn-58Bi solder did not change the lamellar microstructure of Sn-58Bi solder (Hu et al., 2015). Spherical primary Sn-rich phase in Sn-58Bi solder increases by alloying In into the solder while Sn-58Bi-4In solder forms Bi-In phase (Kang et al., 2021).

In terms of mechanical properties, 0.5 wt. % alloying addition of Sb, Ag and Cu and into Sn-57.7Bi solder recorded the elongation of 42%, 18% and 24%, respectively

compared Sn-58Bi solder with 10% elongation only (Sakuyama et al., 2009). Li et al. reported that the elongation of Sn-58Bi-0.1Er solder increased from 15.34% to 50.18% compared to Sn-58Bi solder (Li et al., 2020). Increased in the elongation, indicated the enhancement of the solder ductility. Compared to tensile test on Sn-45Bi solder alloy, Sn-45Bi solder alloy with alloying addition of 2.6 wt.% of Zn, enhanced the solders ductility by more than double (Zhou et al., 2019). 1-2 wt. % alloying addition of Sb into Sn-52Bi solder successfully preserving the ductility of Sn-52Bi solder while enhanced the ultimate tensile strength by 20% (Paixão et al., 2020).

By minor alloying of Co element into Sn-Bi solder, Co is anticipated to lessen the brittle nature of Bi and lowered the Cu_3Sn intermetallic compound layer growth rate to pattern a reliable solder joint. Co is also expected to improve Sn-Bi solder mechanical properties without increasing Sn-Bi solder melting temperature drastically and eventually could be applied for Sn-Pb solder replacement and low temperature soldering application.

Therefore, in this dissertation, Co was used as an additional alloying element in Sn-58Bi solder alloy. The melting temperature of Sn-58Bi-xCo solder was studied by using differential scanning calorimeter (DSC). Then, the effect of minor alloying Co on the microstructure properties and fractography of the solder were observed by scanning electron microscope (SEM) while the energy dispersive X-ray spectroscopy (EDX) was used to analysed composition of the element and the intermetallic compound (IMC) of the solder alloys. The built-in image analyser software in an Olympus SZX10 stereoscope was used to determine the thickness of the IMC formed. Tensile test and Vickers hardness test were also conducted to assess the Sn-Bi-Co solder alloy mechanical properties. Lastly, microstructure of Sn-Bi-xCo/Cu solder joints under varying aging duration was analysed by SEM and EDX.

1.2 Problem Statement

Co element had structure of hexagonal closed pack (hcp) that could positively improve and give better heterogenous nucleation sites of Sn-rich phases in the solder (Jiang et al., 2020). The microstructure of Sn-9Zn solder was refined and homogenised by alloying Co into the solder (Jiang et al., 2020). 0.1 wt. % alloying addition of Co into Sn-3Ag-0.5Cu solder also result in grain refinement (Sujan et al., 2014). Haseeb et al. reported that after reflow, only 0.18 and 0.75 wt. % were detected after 0.5 and 1.5 wt. % of Co nanoparticles were alloyed into Sn-3.8Ag-0.7Cu solder, respectively (Haseeb et al., 2011). Co alloying addition effect the solder microstructure differently based on the amount of Co added and the solder incorporated with. As the microstructure of a solder could influence its mechanical properties, the effect of Co alloying addition on the Sn-58Bi solder microstructure should be studied.

In terms of mechanical properties, there reported literature on Co as additional alloying element into lead free solder was still scarce. However, Co element is anticipated to strengthen the mechanical properties and improve wetting of Sn-Bi solder (Vakanas et al., 2015). Alloying addition of 2 wt.% of Co nanoparticles into Sn-3Ag-0.5Cu solder results in higher tensile strength and lower ductility compared to Sn-3Ag-0.5Cu solder (Bashir et al., 2016). The microhardness of Sn-3.8Ag-0.7Cu solder marginally increase by alloying Co nanoparticles (Tay et al., 2011). Reported literature also agreed that addition of nanoparticles effectively result in strengthening effect of the solders (Tay et al., 2011). The mechanical properties of Sn-Bi-Co solder should also be studied to observe the effect of Co alloying addition into Sn-58Bi solder.

The alloying addition of Co changed the morphology of intermetallic layer forms in Sn-Ag-Cu solder joint (Tay et al., 2011; Haseeb & Leng, 2011; Sujan et al., 2014). The typical scalloped type of Cu_6Sn_5 intermetallic compound layer form at the solder joint

changed into a planar type after Co diffused into the intermetallic compound layer (Bashir et al., 2016). Co could inhibit the Cu_3Sn growth while extending nucleation and reducing the Cu_3Sn layer after annealing because Co has high affinity for Sn compared to Cu (Cheng, Huang & Pecht, 2017). Maintaining such a low melting temperature and preventing Cu_3Sn layer growth through ternary alloying advantageously avoids brittle fractures in the solder joints while protecting the heat-sensitive components and substrate. However, the effect of microstructure of the solder joint with Co alloying addition after prolongs serviceability have not been reported.

1.3 Objectives

There are three objectives for this research. The objectives are listed below:

1. To investigate the effects of Co addition on the microstructure of Sn-58Bi solder alloy
2. To study the effects of Co addition on the mechanical properties of Sn-58Bi solder alloy
3. To investigate the effect of varying aging duration on the microstructure of Sn-Bi-Co/Cu solder joints

1.4 Research Outline

This dissertation is divided into five chapters. Chapter 1 states the clarification of the brief overall review of the research. This will be incorporated with the problem statement, objectives, and thoughts to solve the problem and accomplish the objectives. The literature review on the relevant works is presented in chapter 2. In this chapter, stated the specification of the study of related project that had been conducted. This is important to precisely understand lead-free solder, Sn-based solder, Sn-58Bi solder, alloying elements and metallization behaviours and properties. This literature review will give the overview of the expected results and give the information in analysing the results data.

Then, chapter 3 will show step by step process from how to develop Sn-Bi-xCo (where $x = 1.0, 1.5, 2.0$ wt. %) solder until ventures for analysis and portray the solder. The characterisation tests are significant to gather solid information for future utilised. Results and discussion will be compiled in chapter 4. This chapter will reveal the results which shows the microstructure and mechanical properties of Sn-Bi-Co solder which gives the further understanding through analysis process. Then, further discussion on the data analysis will be done in this chapter to accomplish the objectives and solved problem statement of this research. Finally, chapter 5 will wrap up all outcomes and discussions to conclude on the valuable findings that earned by completing this research. Suggestion for future utilisation also is incorporated to ad-lib the shortcoming of this research.

CHAPTER 2: LITERATURE REVIEW

2.1 Lead-free Solder

In the past decades, lead-containing solder have been widely used due to its excellence properties including good reliability, good manufacturability, low melting temperature and satisfactory wettability while still consuming lower cost (Wang et al., 2019; Tunthawiroon & Kanlayasiri 2019; Cheng, Huang & Pecht, 2017; Hou et al., 2019). However, lead-free solder alloy has been prevalently introduced and used in electronic devices to replace lead-containing solder (Vianco, Rejent, & Grant, 2004). This is due to the hazardous properties of lead which have a highly toxic element that arise health and environmental concerns (Hou et al., 2019; Yang et al., 2019; Silva et al., 2017; Liu et al., 2016).

These concerns make it crucial to develop lead-free solder alternatives with an environmentally friendlier elements which followed the Restriction of Hazardous Substance (RoHs) and Waste from Electrical and Electronics Equipment (WEEE) Directives in the rapid development and innovation of solder composition to substitute lead-based solder with other alloying elements (Wang et al., 2019; Tunthawiroon & Kanlayasiri 2019; Cheng, Huang & Pecht, 2017). Some countries also had banned the uses of lead such as in Europe, they already banned uses of lead after July 2017 (Takao, Yamada & Hasegawa, 2004; Ramos, et al., 2020; Shrestha et al., 2014). While Japan sticks into the amendment of regulation in Waste Disposal Law and the implementation of Electric Appliance Recycling Law which entitled them to the replace lead with a safer material (Takao, Yamada & Hasegawa, 2004).

Development of lead-free solder alternative should have lower melting temperature compared to 63Sn-37Pb to allow it to be paired with a cheaper component molding compound and printed board laminate materials (Vianco, Rejent & Grant, 2004). Higher melting temperature gives a drawback in tenacity of flux residues increase and

higher maintenance costs to soldering component (Vianco, Rejent & Grant, 2004). Unfortunately, Maruya et al. reported that compared with Sn-Pb solder, lead-free solder has a higher melting point (Maruya et al., 2017). Besides, due to latest trends of miniaturization of lead-free electronic products, thermal damage to components and laminate materials when using high melting temperature material solder need to be avoided (Vianco, Rejent & Grant, 2004; Leong & Haseeb, 2016).

This solder melting temperature also would affect the soldering performance and process (Cheng, Huang & Pecht, 2017; Ren, Wilding & Collins, 2016). Then, the lead-free alternative solder also should have a solidus temperature of equal to or less than eutectic temperature of 63Sn-37Pb solder which is 183°C (Vianco, Rejent & Grant, 2004). The pastry range of the solder alloy should be minimised to preferably to less than 10°C (Vianco, Rejent & Grant, 2004). Thus, having lower melting temperature, adequate solidus temperature, minimised pastry range than 63Sn-37Pb solder and excellence mechanical properties as well as low overall cost consumption need to be taken into consideration in developing a better lead-free solder alternative. This is to ensure that the lead-free solder alternative could replace the lead solder alloy especially for low melting temperature application.

2.1.1 Binary and Ternary Composition Solder

Rapid innovation of lead-free solder composition is composed of two or three alloying elements which creates a binary or ternary composition for solder, respectively. The compositions of the solder alloy are mostly Sn-based solder added with any other suitable metal element (Vianco, Rejent & Grant, 2004). Selection of any addition of minor alloying element depending on the element properties itself which used to improve the properties and characteristics of the solder composition that could substitute Sn-Pb solder to lead-free solder (Tunthawiroon & Kanlayasiri, 2019). However, additional alloying

element could also lead to lower mechanical properties due to its complex microstructure (Tunthawiroon & Kanlayasiri, 2019).

Then, during soldering, ternary composition solder would easily incline to the formation of multiple intermetallic layers and phases which could altered the solder joints mechanical properties (Tunthawiroon & Kanlayasiri, 2019). Some examples of binary composition solder are Sn-Ag, Sn-Cu, Sn-Zn, Sn-In and Sn-Bi while the examples of ternary composition solder are Sn-Ag-Cu, Sn-Ag-Bi, Sn-Bi-Cu and Sn-Cu-Ni. Some of the solder compositions which had been studied in the past will be elaborated in the future section.

2.2 Sn-based Solder Properties

The weight percentage of each element in a composition significantly affect the properties of the composition. Sn as the primary alloying element in lead-free solder alloy become the most promising studies among researcher due to its inexpensive and good wettability (Yang et al., 2016). Similar like the ternary solder composition, high alloying elements contents in Sn-based solders caused some brittle intermetallic phases which would lessen the pre-soldering solders and solder joint ductility and strength (Tunthawiroon & Kanlayasiri, 2019).

Difference in metallurgical characteristics of Sn-based solder than Sn-Pb solder alloy are influenced by the 5% small hard intermetallic strengthening particles where the plasticity deformation happens in the Sn phase (Bieler & Lee 2017). However, problem arise when current circuit board and die design are mostly based on Sn-Pb low melting temperature and soft properties while Sn has harder properties than Pb which eventually makes Sn-based solders stronger than Sn-Pb alloy (Bieler & Lee, 2017). The Sn-based solder development would need to take into accounts these properties to create a better performances solder alloy eventually for low melting temperature solder. Thus, other section will elaborate the phase diagram, thermal properties, microstructure properties,

tensile and hardness properties and interfacial studies of elements in a lead-free solder composition which could be beneficial in this research.

2.2.1 Phase Diagram and Melting Temperature

Phase diagrams explain the relationship between temperature, phases and compositions of a material or alloy in equilibrium condition. Through phase diagram, the melting temperature and phase transition of the alloy could be predicted based on its composition. Phase diagram could be presented in unary, binary and ternary system. An alloy was considered low melting temperature when its soldering temperature below 200 °C (Ribas et al., 2017). Low melting temperature could protect the heat sensitive electronic devices from deteriorate while consuming less energy during soldering (Maruya et al., 2017). Besides, lesser thermal stress and warpage during assembly could also be achieved with lower melting temperature (Ribas et al., 2017). However, most commercially available lead-free solder alloy had higher melting temperature compared to lead solder alloy.

As for Sn-Ag solder alloy, different weight content of Ag in a composition highly influenced the microstructure and intermetallic layer formation of Ag_3Sn phase in Sn-Ag solder where the addition of 4 wt. % Ag, eventually increased its melting temperature by 0.5 °C (Tunthawiroon & Kanlayasiri, 2019; Ren, Wilding & Collins, 2016). The high melting temperature caused difficulty when applied the solder with some electronic components which have low heat tolerance (Takao, Yamada & Hasegawa, 2004; Ren, Wilding & Collins, 2016). Figure 2.1 show the phase diagram of Sn-Ag solder. Figure 2.1 also show that the solubility of Ag in Sn higher than 3.5 % when the soldering temperature exceeding 250 °C (Qu et al., 2013).

The most famous Sn-Ag solder composition among researcher is Sn-3.5Ag solder with melting temperature of 221°C (Silva et al., 2017). The melting temperature of Sn-3.5Ag is the lowest compared with other hypereutectic and hypoeutectic Sn-Ag

composition which make it preferable in electronic industry (Tunthawiroon & Kanlayasiri, 2019). The expansion and contraction due to temperature changes of Sn-3.5Ag also influenced the solder properties of good resistance and ductility to creep and fatigue (Achari, Paruchuri & Shangguan, 1999).

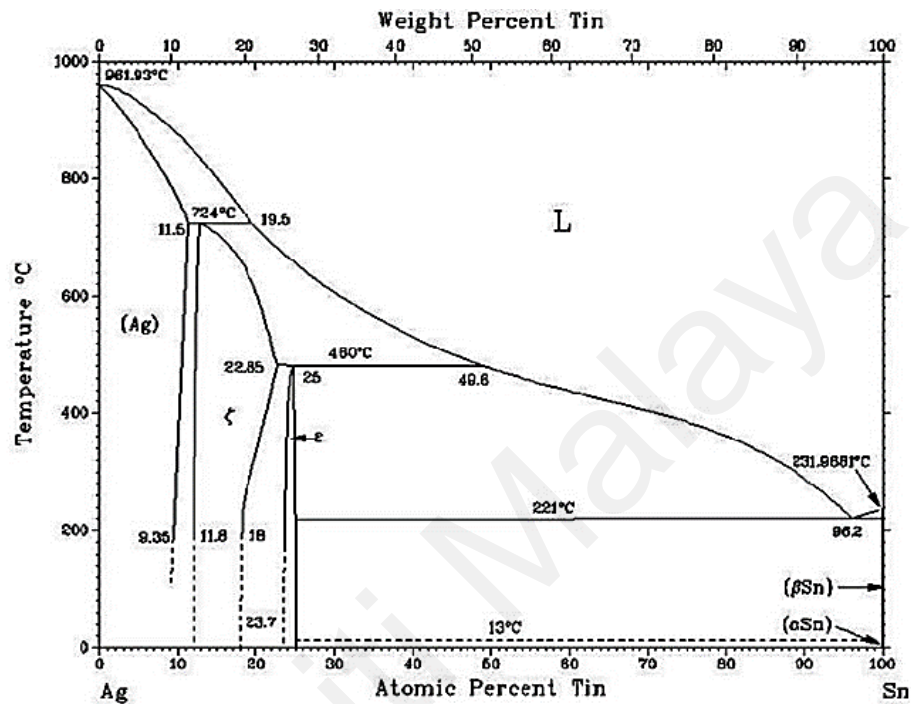


Figure 2.1: Ag-Sn phase diagram (Qu et al., 2013)

When Cu alloyed into Sn-Ag solder, the near eutectic composition of Sn-Ag-Cu as shown in Figure 2.2 has melting temperature of 217-221 °C which then became a problem to the heat sensitive electric components (Tunthawiroon & Kanlayasiri, 2019; Ren, Wilding & Collins, 2016). Sn-Ag-Cu solder usually used in plated-through hole (PTH), some flip chip, ball grid arrays (BGA), small outline package (SOP) and surface mount technology (SMT) applications (Cheng, Huang & Pecht, 2017). However, its melting temperature of 217-221 °C is quite higher than Sn-Pb melting temperature, which could cause thermal warpage on smaller and thinner area array board and components (Wang et al., 2019). The melting temperature could be reduced with some low addition of wt.% of Cu but merely increased when the wt.% is more than 1 (Ren, Wilding & Collins, 2016).

High liquidus temperature of Sn-1.0Ag-0.5Cu requires the solder to be reflowed higher than Sn-3.8Ag-0.7Cu solder alloy (Leong & Haseeb, 2016). Sn-3.0Ag-0.5Cu melting temperature of 217-220 °C during solder reflowing operation is considered very high which causes the electronic components that are attached with the printed circuit board to be easily damaged (Silva et al., 2017). The solder liquidus temperature of 221 °C upon assembling with ultra-thin package results in active warpage on PCB and package substrate (Ribas et al., 2017). Sn-3.0Ag-0.5Cu is also among the lead-free solders' first choice for reflow application which could offer better compositions in terms of wettability, drainage, operating temperatures, and thermal fatigue resistance (Cheng, Huang & Pecht, 2017).

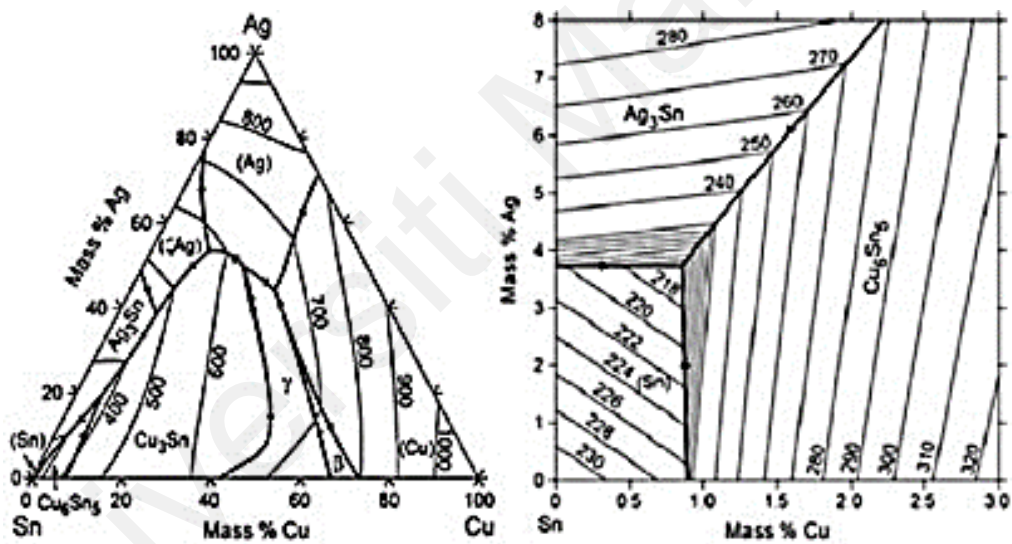


Figure 2.2: Sn-Ag-Cu ternary diagram (Liang, Dariavach & Shangguan, 2007)

The eutectic Sn-Pb solder alloy could also be replaced and substituted with Sn-Zn solder alloy without much increase in the cost and melting temperature (Ramos et al., 2020). The melting temperature of Sn-Zn is 198 °C, having properties of lower toxicity with similar fatigue and creep resistance with Pb-containing solders (Hou et al., 2019; Ramos et al., 2020). Figure 2.3 shows that the melting temperature of Sn-Zn solder is 200 °C (Gornakova et al., 2009). While in contrast with Sn-Ag-Cu solder, Sn-Zn solder alloy

materials have lower cost processing temperature which is less than 200 °C (Ren, Wilding & Collins, 2016).

Sn-9Zn solder alloy composition is the most famous wt.% of Zn composition for Sn-Zn solder alloy that had been studied previously. Sn-9Zn solder alloy have low processing and melting temperature where the melting temperature is 198-199 °C which is corresponding to Sn-37Pb alloy (Wang et al., 2019; Hou et al., 2019; Vianco, Rejent & Grant, 2004; Liu et al., 2016; Ren, Wilding & Collins, 2016).

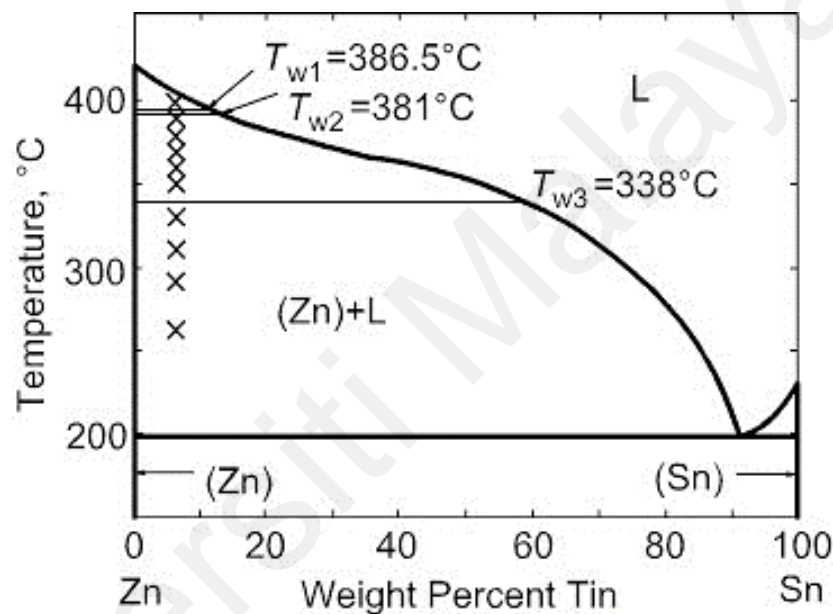


Figure 2.3: Zn-Sn phase diagram (Gornakova et al., 2009)

Figure 2.4 show the phase diagram of Sn-In binary system. Specifically, Sn-52In or also known as eutectic In-48Sn in wt. % has soldering temperature of less than 183 °C which is 118 °C (Wang et al., 2019; Li et al., 2016; Silva et al., 2017; Li et al., 2016a). This low melting point property is an advantageous point to make Sn-52In solder alloy replace the existing lead-containing solder alloys in microelectronic assemble interconnection application (Mokhtari & Nishikawa, 2013; Takao, Yamada & Hasegawa, 2004; Tian et al., 2018).

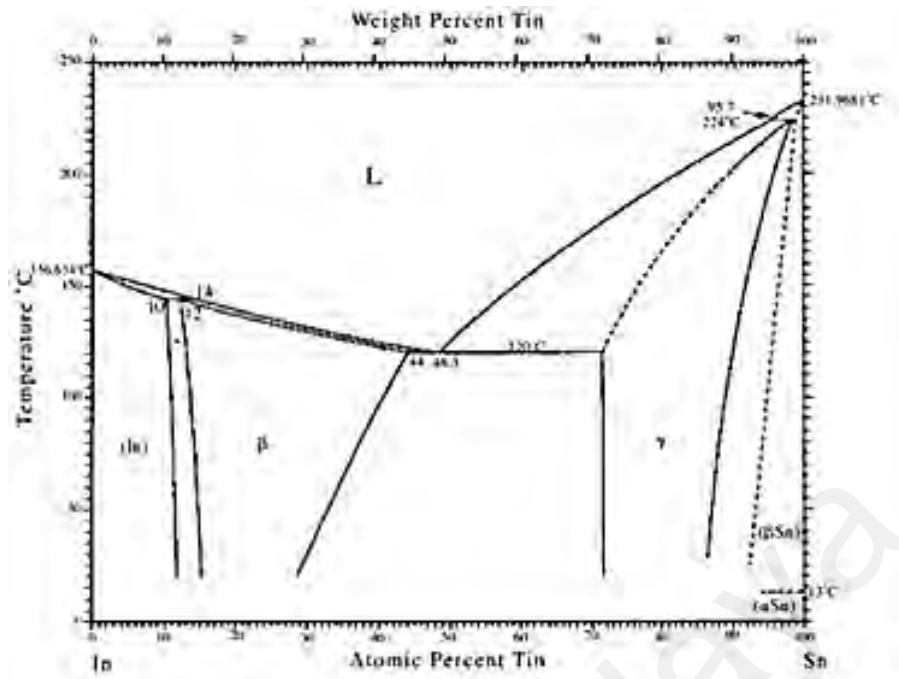


Figure 2.4: In-Sn phase diagram (Brittles et al., 2015)

Based on Figure 2.5 (b), the melting temperature of Sn-Bi is 138 °C which is lower than Sn-Pb solder (Ren, Wilding & Collins, 2016; Yang et al., 2016). While the Sn-Bi nanoparticles melting temperature is 135 °C which also recorded a lower melting temperature than the bulk alloy (Liu et al., 2016). These melting temperatures of Sn-Bi solder which is close to 140 °C is agreeable with both eutectic Sn-Bi solder DSC curve and binary phase diagram eutectic point as shown in Figure 2.5 (Liu et al., 2016). Maintaining its low temperature is crucial because when the temperature increase, the Sn-Bi solder alloy could easily coarsen and could cause drop in the mechanical strength (Yang et al., 2016). However, Abaqus software calculated that the eutectic phase of Sn-Bi solder has a lower mechanical strength than the primary β -Sn phase (Silva, Garcia & Spinelli, 2017). This affirms that the alloy soundness is influence by both eutectic characteristics and fraction of Sn-Bi solder alloy (Silva, Garcia & Spinelli, 2017).

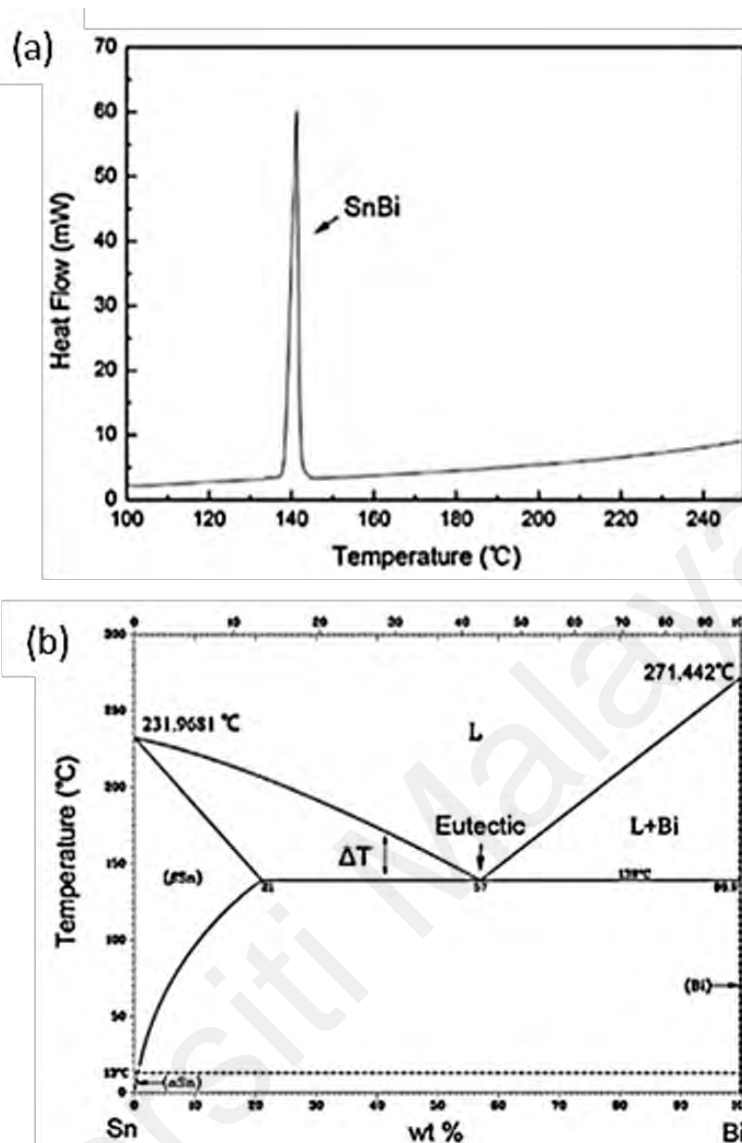


Figure 2.5: (a) DSC curves of eutectic Sn-Bi solder and (b) Binary phase diagram of Sn-Bi solder (Liu et al., 2016)

The coefficient of thermal expansion, CTE of a eutectic Sn/Bi is 1/3 lower than eutectic Sn/Pb where its CTE value is 15 ppm/°C (Ren, Wilding & Collins, 2016). Lower CTE value could lessen the local thermal mismatch of the eutectic Sn-Bi when soldering on material surfaces with low CTE values while improving the solder joint thermal fatigue life (Ren, Wilding & Collins, 2016). It also an important factor that need to be considered for plating in thought holes applications and low temperature soldering of high performances computers mainframes (Silva, Garcia & Spinelli, 2017). However, during flow soldering process, fillet lifting of the joint defect gives some drawbacks on Sn-Bi solder joint reliability (Takao, Yamada & Hasegawa, 2004). While to enable reflow

profiles with lower than 200 °C peak temperature, the Bi content in Sn-Bi should be equal to 40 wt. % or higher. Thus, high content of Bi-rich phase or Bi content needs to be suppressed without increasing the Sn content to avoid enlarging the melting range of the solder due to the liquidus temperature increases as also shown in Figure 2.8 (Liu et al., 2016).

The most famous wt. % of Sn-Bi solder compositions among researchers is Sn-58Bi solder alloy due to its promising characteristics. The fact that the suitable temperature of solder alloy for a low temperature packaging must be less than 180 °C (Liu et al., 2016), make this Sn-58Bi solder alloy one of the best candidates due to the low melting temperature of 138 – 139 °C (Wang et al., 2019; Vianco, Rejent & Grant, 2004; Yang et al., 2019). Besides, for Sn-57Bi solder alloy, the eutectic composition form around 138 °C where when the composition decrease in Bi content changes its liquidus temperature from eutectic composition (Ribas et al., 2017). Figure 2.6 show the ternary diagram of Co-Sn-Bi. Based on Figure 2.6, crystallization regions of FCC_A1, Co₃Sn₂ and CoSn was dominant for the liquidus projection (Hu et al., 2022). These show that when Co was added into Sn-Bi system, ternary compound would not be form.

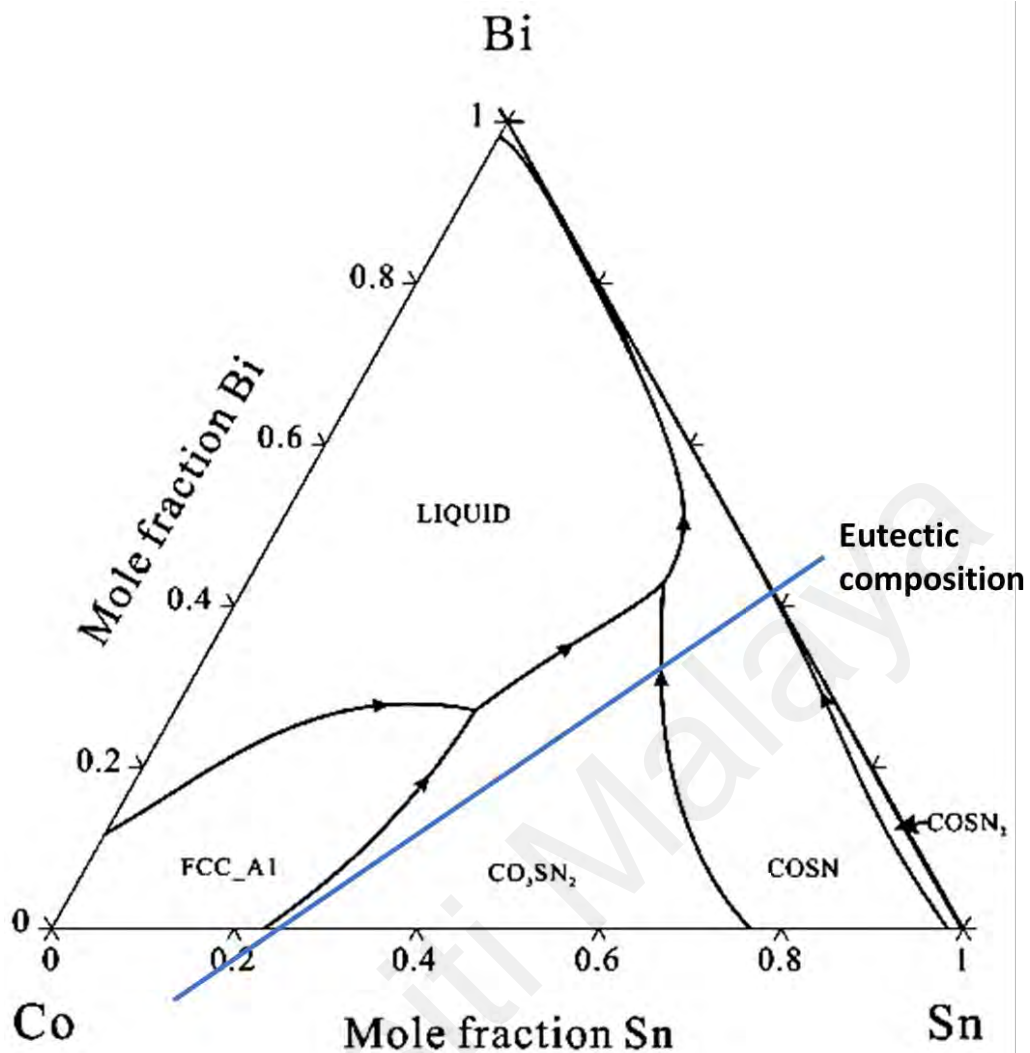


Figure 2.6: Co-Sn-Bi ternary diagram (Hu et al., 2022)

2.2.2 Microstructure Properties

Most reported literature studied the microstructure of the solder alloy by conducting scanning electron microscope (SEM) or field emission scanning electron microscopy (FESEM). Studies on microstructure properties such as the solder morphology, grain size, particle distribution and grain-boundary phases are importance because it could affect the mechanical properties of the solder alloy. Energy dispersive X-ray spectroscopy (EDX) would be paired together to analysed the solder composition and its intermetallic compound formation.

For Sn-Ag solder alloy, less activation energy is needed in the formation of Ag_3Sn than Cu_6Sn_5 which in return contributed to the finer and uniformity of the microstructure

distribution of Ag_3Sn (Tunthawiroon & Kanlayasiri, 2019). Mitigation of coarse microstructure formation due to the presence of the plate-like Ag_3Sn could also affect the mechanical properties of the solders (Tunthawiroon & Kanlayasiri, 2019). Based on Figure 2.7 (a), the dark colour area represents the $\beta\text{-Sn}$ phase where it is surrounded by fine lamellar network of the eutectic structure (Tunthawiroon & Kanlayasiri, 2019).

Figure 2.7 (b) showed $\beta\text{-Sn}$ phase was the dominant phase, with uniformly distributed fine eutectic microstructure of Ag_3Sn which is formed by hypoeutectic microstructure during the rapid cooling of solder fabrication (Tunthawiroon & Kanlayasiri, 2019). However, different variation of cooling rates during soldering could alter the uniformity of the fine eutectic microstructure distribution (Tunthawiroon & Kanlayasiri, 2019). Figure 2.7 (c) and (d) showed that Ag_3Sn large plate like phase is formed around $\beta\text{-Sn}$ phase in both Sn-4.0Ag and Sn-5.0Ag solders where the large fraction of the Ag_3Sn phase is contributed by the increase of Ag content (Tunthawiroon & Kanlayasiri, 2019).

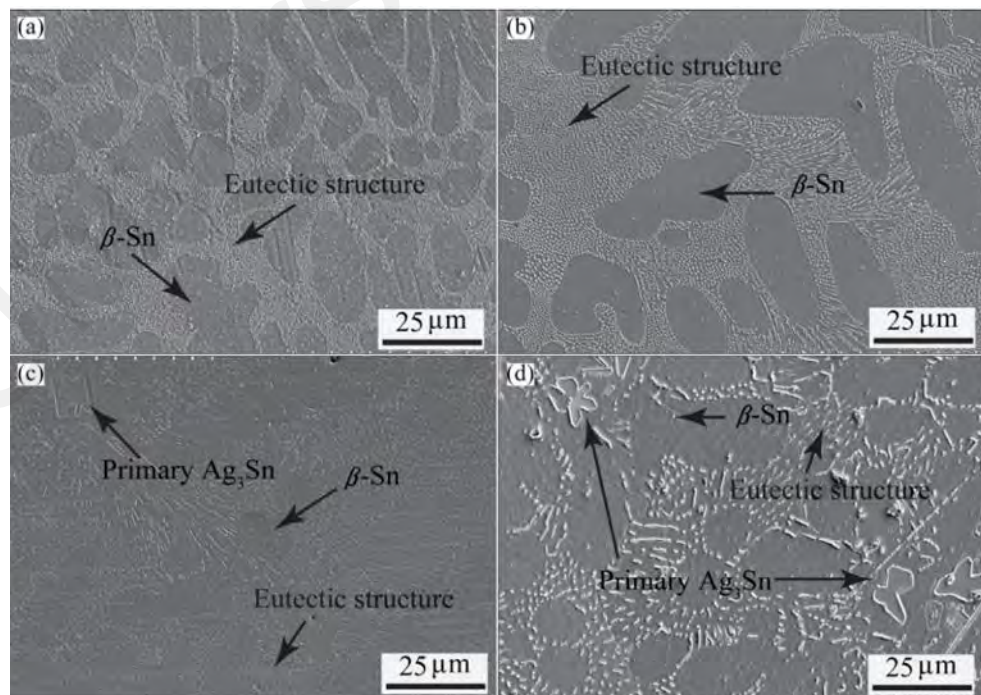


Figure 2.7: As-cast SEM microstructure of (a) Sn-3.0Ag; (b) Sn-3.5Ag; (c) Sn-4.0Ag and (d) Sn-5.0Ag solders (Tunthawiroon & Kanlayasiri, 2019)

In the form of Sn-Ag-Cu solder alloy, Figure 2.8 show the SEM image of Sn-1.0Ag-0.5Cu on Cu substrate. The as-received solder image portrayed that the darker contrast phase is Cu_6Sn_5 while the higher contrast is the primary Sn phase (Leong & Haseeb, 2016). It is also clearly shown that Ag_3Sn particles present in the solder with the formation of continuous network of Cu_6Sn_5 (Leong & Haseeb, 2016). After 1 × reflowed, Cu_6Sn_5 and Ag_3Sn particles become larger as can be seen in Figure 2.8 (b) (Leong & Haseeb, 2016).

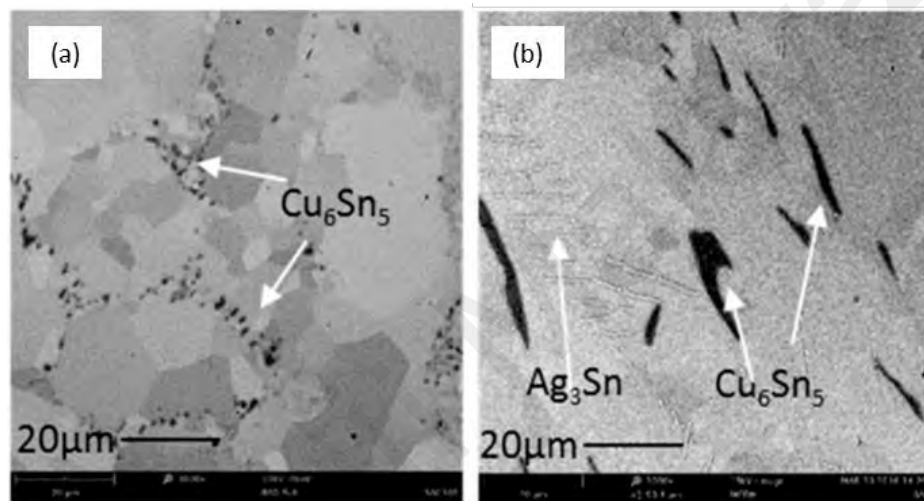


Figure 2.8: SEM image cross sectional sample of bulk microstructure of (a) as-received solder and (b) after 1 x reflow of SAC105 (Leong & Haseeb, 2016)

Other than that, the colonies development in the boundaries of the eutectic Sn-Zn alloy are also very thin compared with Sn-Cu alloy (Ramos et al., 2020). The present of Zn in the Sn-Zn composition result in a poor corrosion resistance due to the Zn-rich precipitates dissolutions existed in the composition eutectic and primary phases (Ren, Wilding & Collins, 2016). While corrosion resistance is one of the important properties in selecting a solder alloy because solders usually would be exposed to corrosion media and media (Liu et al., 2016). Generally, the microstructure of Sn-9Zn solder alloy exhibits near eutectic structure which constituted by Sn-Zn eutectic mixture with needle-shaped Zn-rich precipitates uniformly distributed in the Sn-rich matrix (Liu et al., 2016; Ramos et al., 2020; Ren, Wilding & Collins, 2016).

The SEM image of Sn-9Zn microstructure image is shown in Figure 2.9. The needle-shaped Zn-rich precipitates plays crucial role to the overall corrosion and mechanical properties of Sn-Zn solder where the Zn-rich precipitates are unfavourable to the solder corrosion behaviour (Liu et al., 2016). A better microstructure of Sn-Zn solder alloy could be modified by studying the mechanism of the IMC forming elements which influence the solder corrosion resistance (Liu et al., 2016).

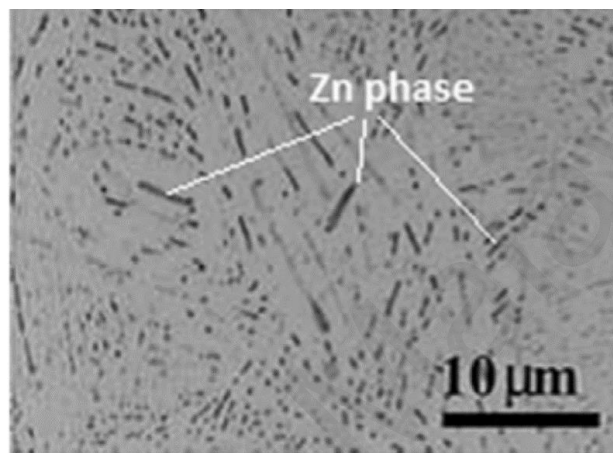


Figure 2.9: SEM image of Sn-9Zn solder alloy (Ren, Wilding & Collins, 2016)

Then, the microstructure image of Sn-52In solder matrix is shown in Figure 2.10. The dark region is identified as In-rich β phase, while the bright region is Sn-rich γ phase which is also indicated by EDX analysis (Li et al., 2016a). This is possible as referring to Sn-In system phase diagram, both element of Sn and In are intersoluble (Li et al., 2016a).

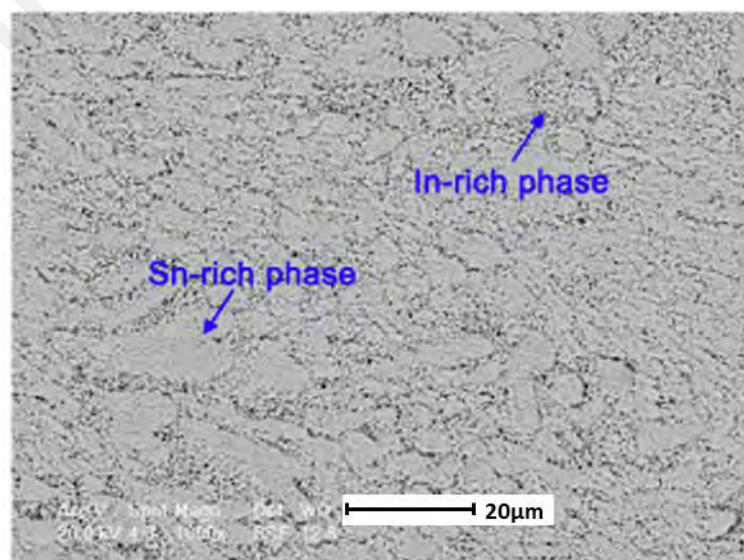


Figure 2.10: Sn-52In solder matrix microstructure (Li et al., 2016a)

Besides, the microstructure of the binary eutectic Sn-Bi characterised as a complex regular structure which is composed of irregular lamellar structure of two phases arranged in alternating not-flat plates (Silva, Garcia & Spinelli, 2017). While the eutectic Sn-Bi microstructure have two types of regions with a complex regular microstructure which are consist of regular repeating pattern zones and other random orientation zones (Silva, Garcia & Spinelli, 2017). Pb-Bi and Bi-Cd solder alloy systems also have a similar structure as this eutectic Sn-Bi microstructure (Silva, Garcia & Spinelli, 2017). However, Wang, F. et. al. reported that Sn-Bi solder alloy of eutectic solution constituted of Bi phase and lamellar β -Sn phase (Wang et al., 2019). While Sn-Bi solid solution consisted of β -Sn phase and Bi particles (Wang et al., 2019).

Then, hypo-eutectic solution composed of primary β -Sn phase and eutectic phase (Wang et al., 2019). Figure 2.11 shows the SEM microstructure and element mapping of Sn-Bi eutectic solder alloy of the solder paste after reflowing. Figure 2.11 (b) shows that the Sn-Bi eutectic solder bulk exhibit structure of homogeneous reticulate where it is mostly consists of Bi-rich phase and Sn-rich phase in the reticulate structure (Liu et al., 2016). The element mapping presented in Figure 2.11 (c) and (d) show the distribution of Sn and Bi elements in the solder bulk respectively (Liu et al., 2016). Ren, Wilding & Collins reported that the crystal structure of Sn-Bi consists of body-centred tetragonal β -Sn and rhombohedral Bi (Ren, Wilding & Collins, 2016).

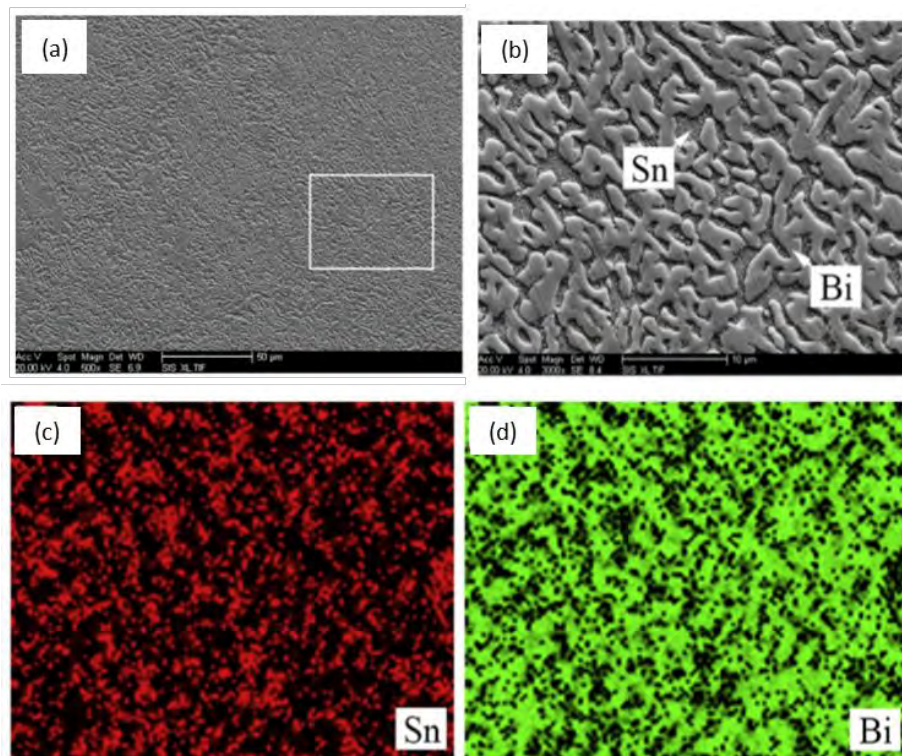


Figure 2.11: SEM microstructure image of (a) eutectic Sn-Bi solder bulk, (b) magnified eutectic Sn-Bi solder bulk, (c) Sn element mapping and (d) Bi element mapping (Liu et al., 2016)

The microstructure phases analysis of Sn-58Bi solder alloy recorded that the solder consisted of alternate layer of Sn-rich phases and network Bi phases in the form of lamellar eutectic structure (Chen et al., 2016). Figure 2.12 (a) show that the Sn phases dissolve the Bi atom and forms nano-sized Bi particles precipitate in the Sn-rich matrix (Chen et al., 2016). The lamellar structure of the intermetallic compound of Sn-58Bi/Cu as shows in Figure 2.12 (b), results in stronger but higher brittle and poorer fatigue life compared with Sn-37Pb solder at room temperature (Ren, Wilding & Collins, 2016).

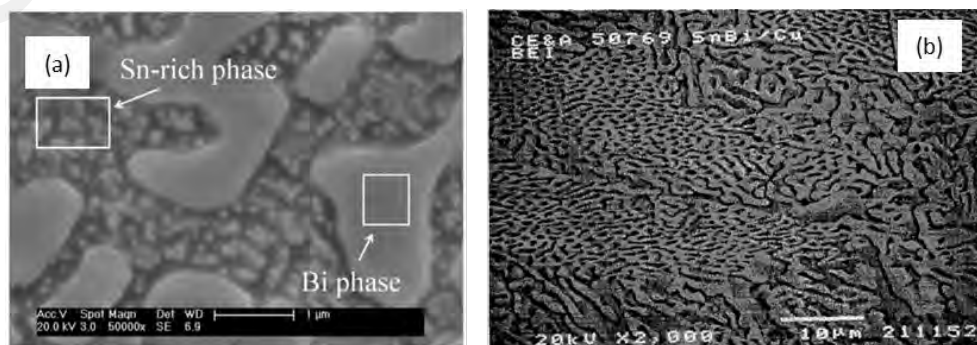


Figure 2.12: (a) Sn-58Bi solder alloy microstructure (Chen et al., 2016), (b) Eutectic Sn-58Bi/Cu solder lamellar structure (Ren, Wilding & Collins, 2016)

2.2.3 Mechanical Properties

Generally, the mechanical properties of the solder were discussed in term of its elongation, tensile strength, modulus of elasticity, shear strength and hardness. By understanding the mechanical properties of the solder, the serviceability of the solder under certain force, temperature and pressure could be determined. This section review some of the reported literature on the mechanical properties of Sn-Ag-Cu, Sn-Zn, Sn-In and Sn-Bi solders alloy.

In contrast with Sn-Cu, Sn-Ag and Sn-Pb solder composition, Sn-Ag-Cu have higher solder joint strength and better electrical conductivity (Tunthawiroon & Kanlayasiri, 2019). Two of the famous Sn-Ag-Cu compositions with different in wt. % of Ag content are Sn-1.0Ag-0.5Cu and Sn-3.0-0.5Cu solder. The solder mechanical properties of Sn-1.0Ag-0.5Cu and Sn-3.0Ag-0.5Cu are shown in Table 2.1. Sn-1.0Ag-0.5 have excellent performance in drop tests but not in thermal cycling tests (Leong & Haseeb, 2016).

Table 2.1: Sn-1.0Ag-0.5Cu and Sn-3.0Ag-0.5Cu solders properties (Cheng, Huang & Pecht, 2017)

| Properties | Solder | |
|-------------------|-----------------------|-----------------------|
| | Sn-1.0Ag-0.5Cu | Sn-3.0Ag-0.5Cu |
| Tensile strength | 5640 PSI | 7200 PSI |
| Young's modulus | 2150 KSI | 2410 KSI |
| Yield strength | 3359 PSI | 5289 PSI |
| Elongation | 13.4 % | 19.3 % |

Vickers Hardness test is performed to Sn-1.0Ag-0.5Cu solder alloy for the indentation testing and results in the hardness of 9.78 HV (Leong & Haseeb, 2016). Then, maximum load of 500 μ N is used on Sn and Cu₆Sn₅ to measure its indentation performance whereby the penetration of indenter is approximately 4.5 times for Cu₆Sn₅

(Leong & Haseeb, 2016). The solder matrix of Sn-1.0Ag-0.5Cu is soft with 0.23 – 0.30 GPa hardness while Cu₆Sn₅ intermetallic hardness is approximately 6.2 GPa (Leong & Haseeb, 2016). Upon unloading, Sn-1.0Ag-0.5Cu forms plasticity and recovered roughly 10 nm of 230 nm from that intermetallic penetration while Cu₆Sn₅ intermetallic recovered around 40 % of the maximum penetration (Leong & Haseeb, 2016). The solder deforms primarily plastic while the intermetallic phases of Cu₆Sn₅ deforms both plastic and elastic formation (Leong & Haseeb, 2016). The solder has much larger residual indents compared with the intermetallic layer which has not detected sink-in of material (Leong & Haseeb, 2016).

Besides, soluble properties of Zn in Sn led to the strengthening effect of Sn matrix (Ren, Wilding & Collins, 2016). Then, the absence of brittle intermetallic particles in the eutectic Sn-Zn alloy phase diagram results in an excellent plasticity where only α -Zn and β -Sn phases are formed during cooling process (Ramos et al., 2020). However, Sn-Zn have low joint reliability and poor wettability due to the oxidation of Zn-to-Zn oxide/hydroxide (Ren, Wilding & Collins, 2016). This Zn oxide/hydroxide required a highly active fluxes to removed it during processing (Ren, Wilding & Collins, 2016). Sn-9Zn also offers high-calibre mechanical properties at room temperature while still costing lower cost than Sn-Ag-Cu solder alloy (Ren, Wilding & Collins, 2016). Compared with Sn-40Pb solder alloy, Sn-9Zn alloy possess higher creep resistance with high fatigue life (Ren, Wilding & Collins, 2016). However, Sn-9Zn have poor wettability and corrosion resistance (Wang et al., 2019; Ren, Wilding & Collins, 2016).

Then, Sn-52In solder also have good mechanical properties, good creep resistance, low coefficient of thermal expansion and high tensile strength (Takao, Yamada & Hasegawa, 2004; Silva et al., 2017). Despite exhibiting a high tensile strength, Sn-52In solder has a lower elongation than Sn-Ag-Cu solder alloy (Wang et al., 2019). Besides, Sn-52In also have excellent ductility, wettability, and fatigue life (Wang et al.,

2019; Chan & Wu, 2016; Li et al., 2016a). These wonderful properties make the eutectic Sn-52In solder favourable for specialised and advanced electronic products such as laser die bonding, chip-on-glass bonding, optoelectronics modules and heat sensitive devices applications (Li et al., 2016a).

The creep analysis performance of Sn-Bi solder alloy had been done using Vickers indentation testing and nanoindentation method by some researchers. The long-time Vickers indentation testing at room temperature for solid solution of Sn-xBi solders where x is ranging from 1 to 5 wt. % shows that when Bi content increase, the creep resistance increase (Wang et al., 2019). This is due to the solid solution of Bi strengthening effect in the Sn matrix (Wang et al., 2019). While nanoindentation method on Sn-xBi solders of x ranging from 3 to 70 wt. % shows that when Bi content increase, creep resistance decreased which makes eutectic and hypoeutectic Sn-Bi solders have lower creep resistance than the solid solution of Sn-Bi solder (Wang et al., 2019).

Wang et al. also conducted nanoindentation tests on Sn-Bi with 3%, 10%, 50% and 57% of Bi wt. % which then shows that the transition stress of the solder creep performance decreased along with Bi content (Wang et al., 2017). These shows that the solder composition and applied stress affects the creep mechanism of the Sn-Bi solder alloy (Wang et al., 2019). Creep mechanism at high, intermediate, and low stress region are dominates by dislocation glide. Dislocation climbs and phase boundary sliding respectively (Wang et al., 2019). Then, in contrast with Sn-Pb solder alloy, the mechanical properties of Sn-Bi considered to be poor due to its high brittleness and lower elongation with present of Bi in the solder composition (Ribas et al., 2017).

Sn-Bi solder alloy elongation could be improved by reducing its Bi content, but the ultimate tensile strength of the alloy does not show many decreases (Ribas et al., 2017). The high content of Bi-rich phase in Sn-Bi solder alloy could affects the hardness and brittleness of the eutectic Sn-Bi solder alloy (Liu et al., 2016). Excessive hardness

and brittleness of solder alloy easily deteriorate the solder joint mechanical properties which then highly contained the solder joint long-term reliability and packaging components (Liu et al., 2016). This brittle behaviour of the Sn-Bi solder alloy is the same in both bulk and interface of the solder joint due to Bi true nature (Mokhtari & Nishikawa, 2013). While the ductility of Sn-Bi solder is also poor at low temperatures in high strain rates due to the present of hard Bi phase (Silva et al., 2017; Maruya et al., 2017). The less ductility makes it tough to ease the strain joint and thermal stress of the solder (Takao Yamada & Hasegawa, 2004). These characteristics would also increase the risk of drop failure of Sn-Bi solder (Cheng, Huang & Pecht, 2017).

Furthermore, Bi content reduction from 58 to 45 wt.% and 58 to 40 wt.% results in increase of drop shock characteristics life in 42 % and 77 % respectively but it still insufficient to cross over Sn-3Ag-0.5Cu drop shock characteristics life (Ribas et al., 2017). Sn-14.5Bi solder alloy recorded the highest bend fracture energy and hardness compared to the other Sn-Bi solder alloy with Bi wt.% of 3.6 %, 7.25 %, 29% and 58% (Wang et al., 2017). The Bi content in the Sn-Bi solder alloy composition should be in the adequate amount because addition of Bi could improve Sn-Bi solder alloy mechanical properties (Yang et al., 2019).

Sn-58Bi also have impressive solderability properties (Vianco, Rejent & Grant, 2004), good wettability and high mechanical properties (Yang et al., 2019). Compared with Sn-Pb solder, Sn-58Bi solder alloy exhibit higher shear strength and superior creep resistance (Mokhtari & Nishikawa, 2013). Wang et al. reported that Sn-58Bi solder creep test shows that the curve followed all the traditional stages of primary, steady, and tertiary (Wang et al., 2019). Wang et al. and Chen et al. observed that higher temperature lessens the tensile strength while improve Sn-58Bi solder alloy ductility (Chen et al., 2016; Wang et al., 2019). Decreased in tensile strength would increase the solder elongation whereas when the strain rate reduced, the tensile strength improved significantly but deteriorate

the solder ductility (Chen et al., 2016). Figure 2.13 shows that raise in temperature results in further finely-broken surface fracture while raise in strain rate flatten the surface dimples which decreased the solder toughness characteristics (Chen et al., 2016).

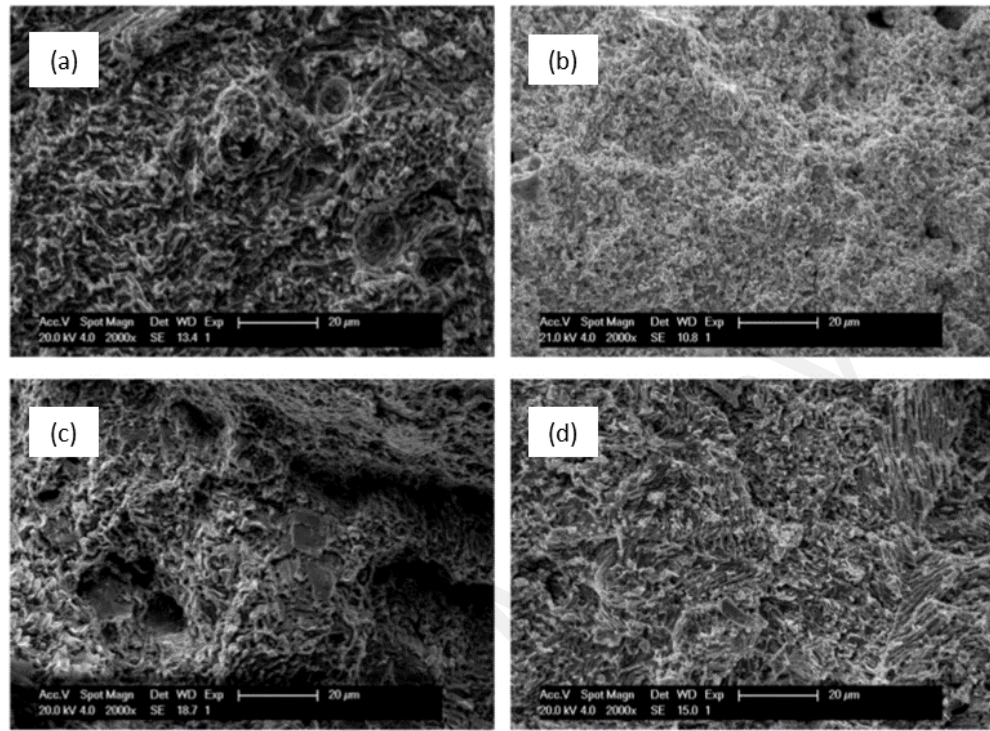


Figure 2.13: SEM image of Sn-58Bi solder alloy fracture surface at (a) 25°C, (b) 125°C, (c) 0.0004 s⁻¹ strain rate and (d) 0.05 s⁻¹ strain rate (Chen et al., 2016)

Then in-situ tensile test and nanoindentation test were carried out to investigate the Sn-58Bi eutectic solder creep deformation mechanism. Chen et al. stated that from in-situ test at low strain rate, Sn and Bi phases forms large deformation and sliding, while at high strain rate the formation was vice versa whereas there nearly no sliding and deformation between the phases (Chen et al., 2016). Under nanoindentation test of 25°C, the deformation mechanism behaviour at high strain rate, dislocation glide controlling dominants while at low strain rate dominant by grain and phase boundary (Chen et al., 2016). Both tensile test results show that Sn-Bi solder alloy highly affected by strain rate (Chen et al., 2016).

2.2.4 Interfacial and Aging Studies

Interfacial studies were very importance to observe the solder microstructure after reflow and the intermetallic compound layer (IMC) morphology between solder and substrate. This IMC morphology will influence the joint performance of the solder. Then, from aging studies, the serviceability and performance of the solder joint after prolongs usage cycle or thermal cycle could be analysed. However, the types of metallization used to pair with any solder alloy is crucial to ensure that the solder joint will have a great reliability, wettability, and strength in the assembly process of PCB (Cheng, Huang & Pecht, 2017). Solderability and reliability of a solder joint could also be evaluated by choosing the right metallization (Cheng, Huang & Pecht, 2017).

In 2012, IPC and National Physical Laboratory (NPL) had conducted a survey which recorded that the single most contributor to PCB defects is surface finish solderability where the surface finish is usually form between solder and PCB interface (Cheng, Huang & Pecht, 2017). The surface finish act as preservation of the solderability during substrate and PCB assembly process (Cheng, Huang & Pecht, 2017). The formation of intermetallic compound at the interface and growth rate will be highly affected by the different in substrate used (Wang et al., 2019). Intermetallic compound performance enhancement also is commonly done by either metallization or solders with minor alloying element (Wang, Li & Huang, 2017). Aside choosing the suitable alloying, metallization also plays the same important role in the overall performance of a solder alloy composition. Metallization was discussed further in terms of IMC properties and between Cu substrate and solder.

Intermetallic compound (IMC) layer forms metallic bonding between solder and substrate during soldering (Wang et al., 2019; Ren, Wilding, & Collins, 2016). Better understanding in IMC properties is necessary to study the solder joint strength during soldering and its metallurgical (Wang et al., 2017). The solder joint strength could be

enhanced when the interface of solder and substrate forms a thin layer of IMC during soldering (Wang et al., 2019). Thick IMC would tend to lessen the mechanical properties of the solder joint (Ren, Wilding & Collins, 2016) but it will not be the case for the joint strength of some solder joint (Wang, Li & Huang, 2017). The hard and brittle nature of IMC during solder and substrate soldering or aging will easily deteriorate the solder joint reliability and strength due to IMC layer growth (Wang et al., 2019; Wang, Li & Huang, 2017).

Most papers also reported that high temperature aging would cause growing of IMC thickness and eventually deteriorate the solder joint strength (Wang, Li & Huang, 2017). The solder joint reliability could also be enhanced by achieving more rounded or curved IMC surface morphology, more meagre coefficient of thermal expansion discrepancy between the component and board and lower Young's modulus (Ren, Wilding & Collins, 2016). Therefore, mechanical properties and reliability of the solder joint are highly influenced by the IMC formation and growth.

The electronic industry nowadays is juggling to enhance the solder joint reliability by controlling the growth mechanism of the IMC (Wang, Li & Huang, 2017). The development of reported IMCs between some solders and Cu substrate is discussed. Cu often used as a substrate with a lead-free solder as most of the electronic compound nowadays are from Cu based material. Cu also is easily available and environmentally friendly to be used as substrate (Skwarek et al., 2018). Sn-based lead-free solder when incorporate with Cu substrate, it will form an interfacial intermetallic compound of Cu_3Sn and Cu_6Sn_5 depending on the Bi-Cu-Sn ternary system (Wang et al., 2019). The ternary system of Bi-Cu-Sn was shown in Figure 2.14.

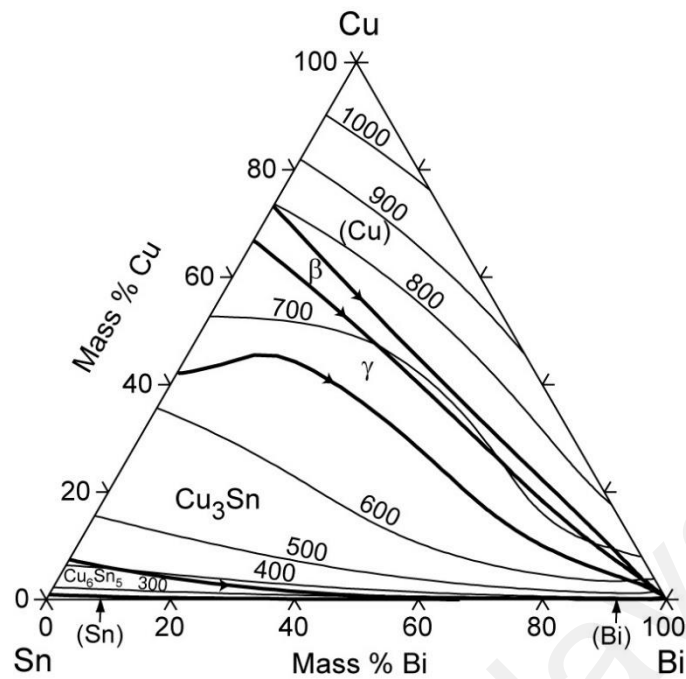


Figure 2.14: Bi-Cu-Sn ternary system (“Bi-Cu-Sn System”, n.d.)

When Sn-Ag soldered with Cu substrate, the brittle growth of Cu_6Sn_5 intermetallic layer is interfered due to the formation of fine intermetallic phase of Ag_3Sn (Tunthawiroon & Kanlayasiri, 2019). These fine Ag_3Sn is useful to improve the reliability of Sn-xAg solder and Sn-xAg/Cu joints (Tunthawiroon & Kanlayasiri, 2019). However, too much Ag content could form a large plate-like Ag_3Sn which would accelerates the Sn-xAg/Cu joints failure (Tunthawiroon & Kanlayasiri, 2019). The precipitation of fine Ag_3Sn particles on the solidified surface and Cu_6Sn_5 grain boundaries hindered the growth of Cu_6Sn_5 grains whereby it is also known as the shielding effect of Ag_3Sn on the growth formation of Cu_6Sn_5 which prevent the diffusion of Cu atoms from the Cu substrate (Tunthawiroon & Kanlayasiri, 2019). The brittleness of Ag_3Sn also decreased the shear and tensile strength of the solder joints which then would affects its reliability and durability (Tunthawiroon & Kanlayasiri, 2019). Sn-Ag also could easily coarsening during thermal cycling which caused fluctuation fatigue and creep resistance of the solder (Achari, Paruchuri & Shangguan, 1999).

Sn-3.0Ag solder composition contains 3.0 w.t % of Ag content have 94.6% of average spreading factor on Cu substrate (Tunthawiroon & Kanlayasiri, 2019). In Figure 2.15 (a), the intermetallic layer of Sn-3.0Ag/Cu showed that eutectic Ag_3Sn is observed in the joints with 1.14 μm intermetallic layer thickness (Tunthawiroon & Kanlayasiri, 2019). Then, Sn-3.5Ag/Cu have 1.58 μm intermetallic layer thickness and wettability of 93.8 % of average spreading factor where the finely distributed Ag_3Sn observed in the joints as in Figure 2.154 (b) (Tunthawiroon & Kanlayasiri, 2019).

EDX map analysis of Sn-3.5Ag solder cross-sectional also prove that only Ag_3Sn is finely distributed and more prevalent compared to Cu_6Sn_5 in the solder matrix (Tunthawiroon & Kanlayasiri, 2019). While its intermetallic layer morphologies with Cu substrate in Figure 2.15 (c) and (d) showed that both large plate like Ag_3Sn and eutectic Ag_3Sn are present in the joints with 1.78 μm and 1.86 μm intermetallic layer thickness respectively (Tunthawiroon & Kanlayasiri, 2019). The Sn-5.0Ag solder shows the similar cross-sectional of EDX map with Sn-3.5Ag solder (Tunthawiroon & Kanlayasiri, 2019). Sn-4.0Ag/Cu and Sn-5.0Ag/Cu both have the average spreading factor of 94.2 % and 95.06 % for its wettability respectively (Tunthawiroon & Kanlayasiri, 2019).

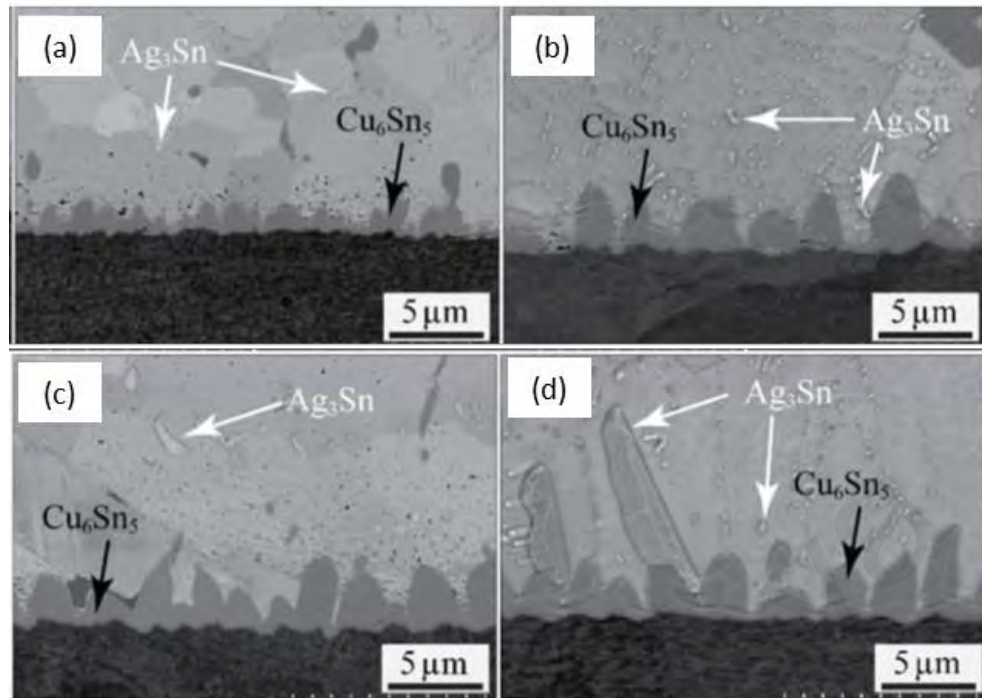


Figure 2.15: Intermetallic layer morphologies of (a) Sn-3.0Ag; (b) Sn-3.5Ag; (c) Sn-4.0Ag and Sn-5.0Ag solders with Cu substrate (Tunthawiroon & Kanlayasiri, 2019)

As for Sn-Ag-Cu/Cu solder joint, the present of Cu in the composition also shows some concerns in Cu dissolution, excessive voids, and IMC of Sn-Ag-Cu solder (Cheng, Huang & Pecht, 2017). The amount of undercooling of Sn-Ag-Cu is 10-30 °C and considerably high which could cause reliability and joint embrittlement problems due to the formation of large plate-like Ag_3Sn structure (Leong & Haseeb, 2016). FESEM micrograph of Sn-1.0Ag-0.5Cu on Cu substrate after 1 × reflowed in Figure 2.16 (a) shows scallop type Cu_6Sn_5 layer formed at the interface (Leong & Haseeb, 2016). Then another intermetallic layer formed in between both layers after isothermal aging at 150 °C for up to 720 h as shown in Figure 2.16 (b) (Leong & Haseeb, 2016).

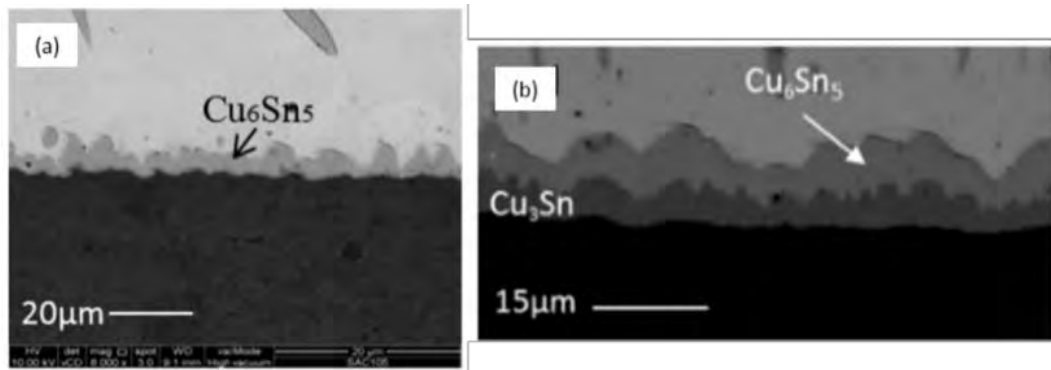


Figure 2.16: SAC (a) cross sectional micrograph after 1 x reflow and (b) cross sectional image after aging at 150 °C for 720 h (Leong & Haseeb, 2016)

Then, Sn-Zn/Cu solder joint also had some concerns where the formation of Zn-rich precipitates needs to be suppressed by forming Zn-containing intermetallic with the joint (Liu et al., 2016). Previous studies of the Sn-Zn/Cu intermetallic shows that after soldering, Cu-Sn and Cu-Zn systems are created at the interface (Gancarz, 2016). The diffusion of Cu with the solder creates Cu_5Zn_8 layer and forms the precipitates of Cu-Sn system (Gancarz, 2016). This Cu_5Zn_8 layer would grow due to its lowest activation energy among the other phases while the system tends towards equilibrium (Gancarz, 2016). Fractures and continuity of the Cu_5Zn_8 layer during annealing process are very also important to determine the layer formation from either Cu-Zn system at the interface or precipitates emergence of Cu-Sn system (Gancarz, 2016).

The present of Zn in the composition also results in poor processing and solder paste shelf life of the solder alloy (Vianco, Rejent & Grant, 2004). There is also a postulate which state that the wetting kinetics degradation could be achieved by reduction of Zn interfacial concentration (Ren, Wilding & Collins, 2016). Analysed of Sn-9Zn solder joints under cyclic stimuli of Garafalo-Arrhenius creep model and finite element analysis in chip scale package for different lead-free solder alloy, results in an equivalent creep strain and lower von Mises stress (Ren, Wilding & Collins, 2016). Sn-9Zn shows the highest fatigue life compared with Sn-37Pb, Sn-3.5Ag and Sn-5Sb solder alloys (Ren, Wilding & Collins, 2016).

Accelerated temperature cycling test conducted by leadfree European project showed that after 400 cycles, large fraction of Sn-9Zn solder joints had failed whereas under the same condition, Sn-36Pb-2Ag solder recorded a first failure at 1000 cycles (Ren, Wilding & Collins, 2016). There is an assumption where both narrower solder joint fillet formation and fast crack growth attribute to an early fatigue failure of Sn-9Zn solder aside with the different printing properties and rheology of the solder (Ren, Wilding & Collins, 2016).

The Cu substrate dissolved into the alloy and formed a Cu_5Zn_8 IMC layer for Sn-Zn/Cu solder joint (Ramos et al., 2020). After 100 h aging at 150 °C, the IMC layer of Cu_5Zn_8 interface fractured and caused it to act as Sn diffusion channel where Cu_6Sn_5 and Cu_3Sn IMCs formed underneath the Cu_5Zn_8 layer (Ren, Wilding, & Collins, 2016). Besides, when Sn-9Zn solder alloy solidified in the Cu substrate, the small amount of hard CuZn intermetallic particles could improvised the tensile strength of the solder alloy (Ramos et al., 2020). However, the interface microstructural evolution of joint strength could degrade significantly with the solder fast interfacial reaction where Zn phase distributed as fibrous or platelet precipitates in the eutectic phase (Liu et al., 2016).

The present of In in the Sn-52In solder alloy composition also influence its interfacial reaction, IMC phase's structure and morphologies of the solder joint which could influence the solder interconnect reliability and mechanical properties (Tian et al., 2018). Then, Sn-52In/Cu solder joints forms a few types of interfacial IMC when both Sn and In react with Cu substrate which results in complicated microstructure (Li et al., 2016a). Chan & Wu reported that there were $\text{Cu}_2(\text{In},\text{Sn})$ and $\text{Cu}(\text{In},\text{Sn})_2$ phase at Sn-48In/Cu solder alloy interface (Chan & Wu, 2016). Both layers are the Sn-52In solder and single-crystalline Cu substrate interfacial IMC growth where the transformation phase between $\text{Cu}_2(\text{In},\text{Sn})$ and $\text{Cu}(\text{In},\text{Sn})_2$ is notable (Li et al., 2016a).

While Figure 2.17 (a) show Sn-52In/Cu as-soldered interface phases where a bright layer of $\text{Cu}(\text{In},\text{Sn})_2$ forms next to the solder matrix and a dark layer of $\text{Cu}_6(\text{Sn},\text{In})_5$ forms next to the Cu substrate (Li et al., 2016a). After undergoing 480 h isothermal aging at 55 °C, both interfacial layers grew thicker and could be seen clearer, but the thickness of $\text{Cu}(\text{In},\text{Sn})_2$ layer grew more rapidly than $\text{Cu}_6(\text{Sn},\text{In})_5$ layer as shown in Figure 2.17 (b) (Li et al., 2016a).

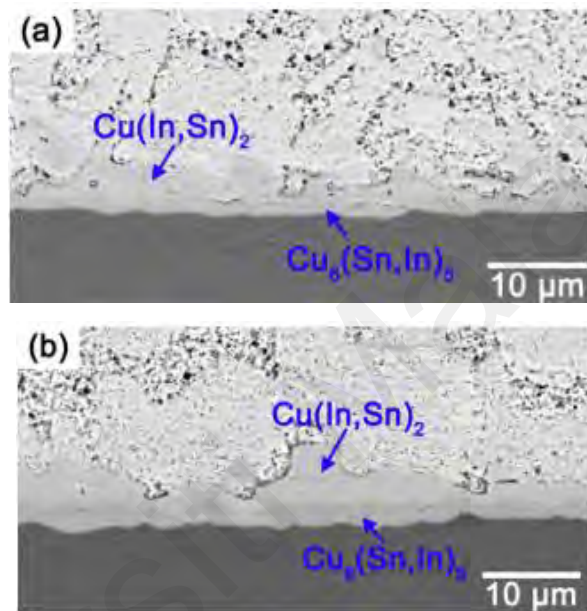


Figure 2.17: Microstructure of Sn-52In/Cu (a) as-soldered interface and (b) after aging at 55 °C for 480 hours interface (Li et al., 2016a).

The same interface layers also presented during 70-100 °C isothermal aging but only an interface layer of $\text{Cu}_2(\text{In},\text{Sn})$ was presented during 100 °C solid-state aging (Li et al., 2016a). During reflow of 150-400 °C temperature ranging, the eutectic Sn-52In/Cu interface form a scalloped layer of $\text{Cu}_6(\text{Sn},\text{In})_5$ near to the solder and a planar layer of $\text{Cu}_3(\text{Sn},\text{In})$ near to the Cu substrate (Li et al., 2016a). Further observation of the Sn-52In/Cu IMC composition is conducted by EDX analysis where the dark layer of $\text{Cu}_6(\text{Sn},\text{In})_5$ is classified as 56.1 at. % Cu, 18.2 at. % In and 25.7 at. % Sn while the bright layer of $\text{Cu}(\text{In},\text{Sn})_2$ is classified as 15.3 at.% Sn, 34.4 at % Cu and 50.3 at. % In (Li et al., 2016a).

Studies show that, the Bi content in the composition could be reduced, but it is still not enough to improve Sn-Bi solder joint reliability (Ribas et al., 2017). The interface of the solder with substrate used also important in soldering. Soldering Sn-Bi solder alloy with Cu substrate shows some decline in the solder joints mechanical properties due to the Bi segregation at the Cu/Cu₃Sn interface (Ren, Wilding & Collins, 2016). While soldering temperature of more than 280 °C also lead to Bi segregation at the Cu/Cu₃Sn interface due to Bi accumulated diffusion at interface and forms isolated Bi particles when cooling (Ren, Wilding & Collins, 2016).

The intermetallic compound studies for Sn-58Bi solder alloy also have been done. Ren, Wilding & Collins, reported that Sn-58Bi solder alloy forms good metallurgical bond with organic coated copper substrates and new non-cleaned low temperature activated fluxes (Ren, Wilding & Collins, 2016). At 200 °C - 240 °C, Sn-58Bi solder and Cu substrates shows η -Cu₆Sn₅ growth followed by ϵ -Cu₃Sn and η -Cu₆Sn₅ growth at the interface (Ren, Wilding, & Collins, 2016). As shown in Figure 2.18 (a) and (b), Sn-58Bi/Cu solder reflow at 160 °C for 10 s, the intermetallic compound (IMC) interface is thin but after aged for 30 days, the IMC thicken (Wang, Li, & Huang, 2017). The IMC layer forms are known as Cu₆Sn₅ and Cu₃Sn layer where the Bi-rich phase coarsen after aging (Wang, Li & Huang, 2017). Interfacial reaction of Sn-58Bi/Cu solder thermally activate the diffusion process and changed the Cu₆Sn₅ scallop structure to plate-like structure (Wang, Li & Huang, 2017).

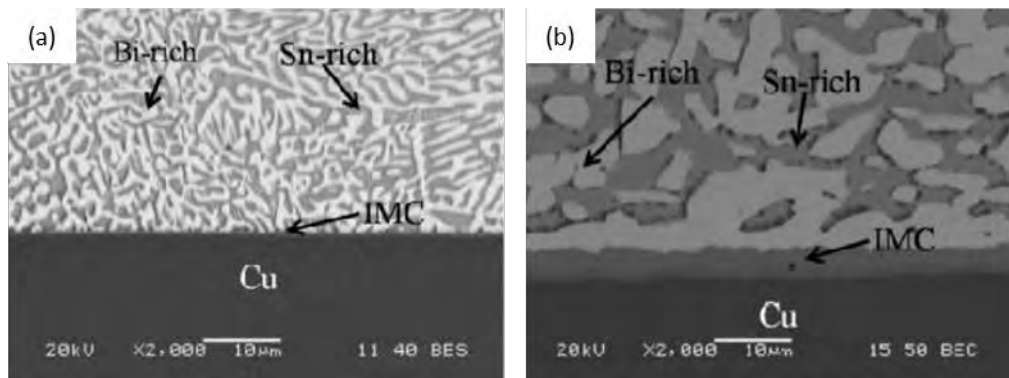


Figure 2.18: SEM images of reflowed Sn-58Bi/Cu solder joint at 160 °C for 10 s (a) before and (b) after aged at 30 days (Wang, Li & Huang, 2017).

The interfacial reaction of Sn-Cu during the intermetallic compound formation of Sn-Cu did not affect by the Bi addition into the Sn-based solder composition, but it enhanced the Sn and Cu interfacial behaviour occurrence (Wang et al., 2019; Wang et al., 2017). There will be an obvious increase in the interfacial of intermetallic compound growth rate when the amount of Bi added in the Sn-Bi solder increased (Wang et al., 2019). The increment of the intermetallic compound growth rate at interface will also be accelerated (Wang et al., 2019).

In terms of melting temperature, Bi addition effectively decrease the solder melting point and eventually accelerate the atomic diffusion of the solder with the substrate because of its higher homologous temperature over the melting point (Wang et al., 2019). The diffusion of Cu atoms from the substrate into the solder matrix will be inhibited by the presence of Bi in the solder and produce the intermetallic compound by accumulated at the interface (Wang et al., 2019). As for non-eutectic Bi-based solder joint, Wang et al. had studied about the Sn-5Bi and Sn-10Bi with Cu substrate, respectively where both solder and substrate forms Cu_3Sn and Cu_6Sn_5 intermetallic compound at the interface (Wang et al., 2017). When compare with pure Sn/Cu joint, Sn-10Bi/Cu joint intermetallic compound develop quicker (Wang et al., 2019).

There are also several reports about the eutectic Sn-58Bi/Cu solder joint. Incorporated of Sn-58Bi solder alloy and Cu substrate form interfacial reaction of Cu_6Sn_5

(Wang et al., 2017). The solder joint strength deteriorated due to Bi-rich layer formation and easily developed Bi atoms segregation at the joint layer (Wang et al., 2017). During isothermal aging, Bi segregation between Cu_3Sn is present in Sn-58Bi/Cu solder joint because of the diffusion of Bi through the intermetallic compound layers of Cu-Sn (Wang et al., 2019). The Bi segregation caused voids formation at the interface and create a barrier of Cu diffusion where Cu atoms had to disseminated around the Bi particles (Wang et al., 2019).

As the results, Cu developed voids and vacancies in between the Cu and Bi particles where the voids deteriorated the tensile strength and fatigue resistance of the Sn-Bi solder joint (Wang et al., 2019). However, compared with Sn-45Bi solder, Sn-58Bi solder had lesser growth rate due to continuous Bi-rich layer formation between the solder and Sn-58Bi solder atomic diffusion inhibited in the intermetallic compound (Wang et al., 2019). The Cu substrate successfully enhanced the Sn-58Bi solder joint tensile properties (Wang et al., 2019). The Sn-58Bi/Cu solder joint shear behaviour also shows good ductility under shear stress (Wang et al., 2019).

The research about Sn-57Bi-Co/Cu solder joint is still scarce. Recently, Wang et al. reported that Co successfully depressed the formation of Cu_3Sn intermetallic compound, however, continue increase in the Co content led to increase in Cu substrate dissolution rate and Cu_6Sn_5 intermetallic compound growth rate (Wang et al., 2019). Therefore, further research on this solder composition is needed to fully understand its properties and suitability to be used for low temperature soldering and heat sensitive electronic devices application.

2.2.5 Summary

Sn-based lead-free solder alloy had been actively studied until today to overcome the drawbacks of lead-free solder and gained the best lead-free solder alternative which had similar performance as Sn-Pb solder alloy. Sn-Ag is one of the famous solder

compositions studied by past researchers. Sn-Ag have impressive properties of high joint reliability, good resistance, and good conductivity to thermal and creep fatigue (Tunthawiroon & Kanlayasiri, 2019; Takao, Yamada & Hasegawa, 2004). However, Sn-Ag have some drawback where Ag element is quite costly and possess high melting temperature (Tunthawiroon & Kanlayasiri, 2019). Ag content in a solder composition also affect the microstructure and intermetallic layer of the solder but insignificantly affecting its wettability.

In general, Sn-Ag-Cu have many beneficial properties such as high-calibre wettability, solderability, reliability and mechanical properties (Wang et al., 2017). Sn-3.0Ag-0.5Cu is still the most reliable solder alloy composition for hand and wave soldering applications, favoured choice for solder pastes and widely used for solder balls on device substrates (Cheng, Huang & Pecht, 2017). In contrast, Sn-37Pb ductility will increase with increasing temperature or strain rate, while Sn-3.0Ag-0.5Cu ductility is independent of the temperature and strain rate (Chen et al., 2016). However, carbon emission could be reduced while saving the energy cost by replace the Sn-3.0Ag-0.5Cu solder alloy with other solder composition (Ribas et al., 2017). Furthermore, upon having moderate wetting characteristics, Sn-3.0Ag-0.5Cu has enormous Cu dissolution with relative rate of 2.1 (Cheng, Huang & Pecht, 2017). This Cu dissolution problem could cause high processing and bulk purchase cost (Cheng, Huang & Pecht, 2017).

Sn-Ag and Sn-Ag-Cu solder alloys considered to have high melting temperature which are more than 200 °C. However, Sn-Zn, Sn-In and Sn-Bi solder alloys have low melting temperature which was suitable for low temperature soldering application. Sn-Zn have some advantages such as possessed similar fatigue performance and creep resistance as Sn-Pb solder, low melting temperature, low cost and lower toxicity (Hou et al., 2019; Liu et al., 2016). Nevertheless, Sn-9Zn solder had poor corrosion resistance and poor interfacial bonding (Jiang et al., 2020; Liu et al., 2016). Sn and Zn elements also could

form some brittle phase in the composite solder which cause deterioration of its mechanical properties (Ding et al., 2018). These drawbacks caused limitation for Sn-Zn solder application especially under corrosive media and moisture exposure (Liu et al., 2015).

Additionally, Sn-In is one of the low temperature solder alloys which widely used in many low temperature fields and for surface mount technologies due to its lower melting temperature property (Ribas et al., 2017). However, the major drawback for Sn-In solder alloy is the high cost of Indium material which makes it a costly solder (Wang et al., 2019). Another low temperature solder alloy which is considered as favourable solder alloy among researchers is Sn-Bi solder alloy. Sn-Bi solder alloy have huge advantages among the other solders alloy in replacing Sn-Pb solder due to its good wettability, low melting point, inexpensive solder material and impressive thermal properties (Yang et al., 2016). Besides, Sn-Bi solder alloy is technically advantageous than the standard Sn-Ag-Cu based lead free solder in electric application (Ren, Wilding & Collins, 2016).

Sn-Bi also have good joint strength, impressive creep resistance and high tensile strength (Silva et al., 2017; Ren, Wilding & Collins, 2016). However, despite of the impressive characteristics, Sn-58Bi solder also have some drawbacks which need to be studied further for improvement. Sn-Bi solder greatly dependent on strain rate where under high strain rates, the solder shows poor ductility (Maruya et al., 2017; Chen et al., 2016). The brittle nature of Bi also caused coarsening and embrittlement to the solder. These disadvantages result in segregation during service and drop the solder mechanical properties (Yang et al., 2019; Liu et al., 2022). Thus, further studies is needed to improve the solder mechanical properties to make the solder more compatible for low temperature soldering application to replace lead solder alloy.

2.3 Method of Improving Solder Performances

There are several alloying addition methods had been introduced to improve the solder performances. Flux doping technique, directional solidified method and powder metallurgy method are some of the method that had been implemented by the researchers. The details on the methods are discussed in the next sub-section.

2.3.1 Flux Doping Technique

Flux doping technique is the technique used by mechanically mix the selected addition alloying element powder with flux for 30 min (Bashir et al., 2016). To ensure that the powder would mix well together with the flux, the powder should be in micro or nano particles sizes while the type of flux used should be water soluble. The doping process onto the solder could be conducted under solid state reaction or liquid state reaction. For solid state reaction, the mixture was doped onto solid solder and undergoes certain heat treatment below the solder melting temperature at certain duration for the additional alloying element to diffused into the solder. While for liquid state reaction the mixture was doped during the reflow process of the solder joint.

2.3.2 Directional Solidified Method

Directional solidified method is conducted by directly melt all the high purity element with respect to the elements selected quantities in induction furnace to form a molten alloy (Paixão et al., 2020). The molten alloy was constantly heated at certain time for melt homogenisation. Then, the homogenised molten solder would be casted into several mold which is suitable for the testing.

2.3.3 Powder Metallurgy Method

Powder metallurgy method is employed by mechanically blend the weighed and selected solder and additional alloying element powder with 20 agate balls in agate jar for 10 hours (Zhu et al., 2019). Then, the blended mixture was compressed by bead

machine and sintered for solder ingots. Lastly, the solder ingots were cut into several slab for further tests.

2.4 Effect of Alloying Element on Lead-Free solder

The most suggested way to improve the Sn-Bi solder alloy microstructure and mechanical performances is by alloying additional element into the solder composition. By added alloying element into Sn-Bi solder alloy, segregation of Bi could be reduced (Mokhtari & Nishikawa, 2013) and the solder elongation could be improved (Yang et al., 2019). However, the amount of added alloying element needs to be controlled to avoid over segregation, formation, and overgrowth at the intermetallic compound (Yang et al., 2019). Alloying element could also enhance Sn-Bi solder alloy thermal cycling and drop shock (Ribas et al., 2017) while would affect the solder melting temperature positively or negatively depending on the added element properties (Yang et al., 2019).

Solidification of higher liquidus temperature phases could also be induced and effectively prevent grain growth of solder phases of binary composition while providing additional heterogeneous nucleation sites (Yang et al., 2019). Lower melting temperature element could help to soften the Sn phase while lowering melting point of the solder (Yang et al., 2019). Then, mechanical properties of the solder could also be enhanced by controlling the solder matrix major phases grain size and minor phases amount and distribution when alloying additional elements in the solder composition (Yang et al., 2019).

2.4.1 Properties and Criteria of Alloying Selection

There are several alloying elements which had catch much attention to researchers recently such as Co, Bi, Mn, Ge, and Ni (Cheng, Huang & Pecht, 2017). Properties such as melting temperature, microstructure, ductility, shear strength and wetting performance of a solder composition are some of the key points to determine the most suitable alloying element to be added in any solder composition to improve its performance and

properties. The bulk and interfacial intermetallic compound of a solder could easily affect by these properties (Cheng, Huang & Pecht, 2017). Usually, Differential Scanning Calorimeter (DSC) is used to measure the thermal properties and melting point of a solder composition. Suitable alloying element addition could help to achieve the desired melting temperature for the targeted usage.

Then, microstructure of the solder would be easily disturbed by any addition alloying addition where it will also influence the mechanical properties of the solder and solder joint (Wang et al., 2019). Refinement of the solder microstructure by alloying additional element onto the solder composition will positively enhanced the mechanical properties of the solder (Wang et al., 2019).

The mechanical properties that should be looking at when added any additional element are tensile properties, shear strength, creep, and hardness. The tensile properties will indicate the solder alloy solder joint performance (Wang et al., 2019). For Sn-Bi solder, the strain rate and temperature applied during the tensile test, highly influence the overall performance of the solder joint (Wang et al., 2019). The tensile properties of Sn-Bi also will be affected by additional alloying element into Sn-Bi solder. Then, the shear strength of the solder joint is tested by conducting shear test.

The solder joint will shear when the force applied exceed a certain level where the harder the solder, the greater the shear force required to shear the solder joint (Cheng, Huang & Pecht, 2017). Temperature, aging time and interfacial intermetallic compound layers thickness and transition formed are the properties which influence the sheer force of a solder joint (Wang et al., 2019). The increased in the solder resistivity to plastic deformation will caused higher shear and shear rate (Wang et al., 2019). The failing of brittle elements in load chain can also be preserve if the solder joint could absorb the strain caused by shock and cycling loading (Cheng, Huang & Pecht, 2017).

The shear strength of a solder also will affect differently based on the alloying element (Wang et al., 2019). Besides, creep resistance and creep rate of Sn-Bi solder highly influence by the Bi content in the solder alloy (Wang et al., 2019). The creep properties of a solder could be enhanced by different alloying elements (Wang et al., 2019). The structure of Sn-Bi solder joint interfacial growth also can be lowered by added small amount of alloying element in the solder (Wang et al., 2019).

In addition, wettability of the solder joint is also important to measure the molten solder ability to maintain contact with the metal surfaces/substrate (Cheng, Huang & Pecht, 2017) and the molten solder alloy composition spreading ratio (Takeda, Habu & Yamauchi, 2002). Spreading ability of the solder is influenced by the surface tensions and interfacial intermetallic compound formation between liquid-flux, solid-flux, and solid-liquid (Wang et al., 2019). Wettability of the solder can be used to measure the solder's solderability where it can be evaluated by conducting spreading test to gain the contact angle of the molten solder (Wang et al., 2019). Young's equation will be utilised to calculate the contact angle of the molten solders where the smaller the contact angle result in better the solder alloy wettability (Wang et al., 2019).

In the record, the contact angle of Sn-37Pb solder is 25° , thus contact angle with less or nearly to 25° need to be achieved to get a solder alloy with a better wettability than Sn-37Pb (Wang et al., 2019). As additional alloying element in Sn-Bi affect the solder wettability, the wetting temperature and amount of Bi in the solder composition also play similar role in affecting the solder wettability (Wang et al., 2019). Usually, high wetting temperature will increase the molten solder and substrate interaction which then will positively affect the wettability of the solder (Wang et al., 2019). However, in this case, the best addition of alloying element in Sn-Bi solder composition needs to be determined to reach the objective of low temperature solder with good wettability.

Besides, reliability, cost, intermetallic compound layer thickness and ductility of the solder also the criteria that need to be consider upon choosing the right additional alloying element. A solder alloy reliability is usually evaluated drop shock of solder joint reliability (Cheng, Huang & Pecht, 2017) or in electronic products (Wang et al., 2019). The intermetallic compound layer with brittle origin will eventually cause failure to the solder joint (Cheng, Huang & Pecht, 2017). Aside from the solder packaging process, the solder joint reliability is highly influence by the solder voiding (Cheng, Huang & Pecht, 2017). The voids in a solder alloy composition can be reduce by selecting the most suitable alloying addition which could fill in the voids (Cheng, Huang & Pecht, 2017).

Next, costing is also needed to be consider in the process of selecting additional alloying element where the material/element itself will affect the total solder composition cost (Cheng, Huang & Pecht, 2017) and royalty patent cost. Then, the selected addition alloying element should be able to slow the growth, modify the morphology and control the thickness of the solder intermetallic compound while increasing its toughness, ductility and strength and preventing phase changes disruptive (Cheng, Huang & Pecht, 2017). Thus, to be conclude there are several criteria to be considered before selecting any addition alloying element because these elements could affect the microstructure and mechanical properties of the solder alloy differently. The further literature review details on Bi and Co alloying which will be considered in this research of Sn-based low temperature solder alloy will be discussed.

2.4.2 Bismuth, Bi

Bismuth (Bi) has plenty of advantages as an alloying element in a solder composition and one of the most popular alloying elements in the lead-free solder alloy composition. Bi has properties such as low melting temperature (Cheng, Huang & Pecht, 2017), high tensile strength and easily expands on solidification (Cheng, Huang & Pecht, 2017). Low melting temperature is useful in assuring better soldering result. Low wt. %

of Bi combine with lead-free solder alloy composition will positively reduce the solder melting temperature while enhanced solder wettability and spread (Cheng, Huang & Pecht, 2017). Wettability of the solder alloy could be improved with the present of Bi where when compare with Sn, Bi has lower surface tension (Cheng, Huang & Pecht, 2017). However, Bi is a bit costly then zinc, Zn (Cheng, Huang & Pecht, 2017). Then, Bi itself will cause the solder alloy to be high in brittleness and prone to thermal fatigue (Cheng, Huang & Pecht, 2017). The solder brittleness will eventually increase when it in contact with lead (Cheng, Huang & Pecht, 2017). Thus, alloying Bi element into a Sn-based solder could create low temperature solder but excessive amount of Bi would cause brittleness to the solder composition.

2.4.3 Cobalt, Co

Cobalt (Co) also have some advantages that is useful to enhance lead-frees solder alloy mechanical and microstructure performance. Co is known as brittle, hard and lustrous metal with bluish-white appearance (Cheng, Huang & Pecht, 2017). Co element is ferromagnetic element which active chemically and could forms many compound (Cheng, Huang & Pecht, 2017). Co has the properties to hinder Cu_3Sn growth while develop nucleation and decrease Cu_3Sn layer after annealing due to the high affinity of Co with Sn compared to Cu (Cheng, Huang & Pecht, 2017). Co also could react with Sn and Cu to be dissolved in the solder and forms intermetallic compound layer during reflow (Yakymovych et al., 2016). The combination of Co into Sn-58Bi solder alloy also will not highly influence the composition melting temperature (Cheng, Huang & Pecht, 2017). Thus, these will be beneficial as Co can be useful to lessen the growth of Cu_3Sn and Bi brittle nature in Sn-Bi solder alloy while still could construct a reliable solder joint with low melting temperature.

CHAPTER 3: METHODOLOGY

3.1 Introduction

The overall process of sample preparations and characterisation was discussed illustrated in the Figure 3.1. Flux doping technique was used to customise the pure Sn-58Bi solder into Sn-58Bi-xCo solder where $x = 1.0, 1.5$ and 2.0 wt.%. Samples preparation includes in cutting the solder into different pieces which suits for sample characterisation. Several tests were conducted to observe the thermal, microstructure, composition, crystalline structure and mechanical properties of the solders.

Universiti Malaysia

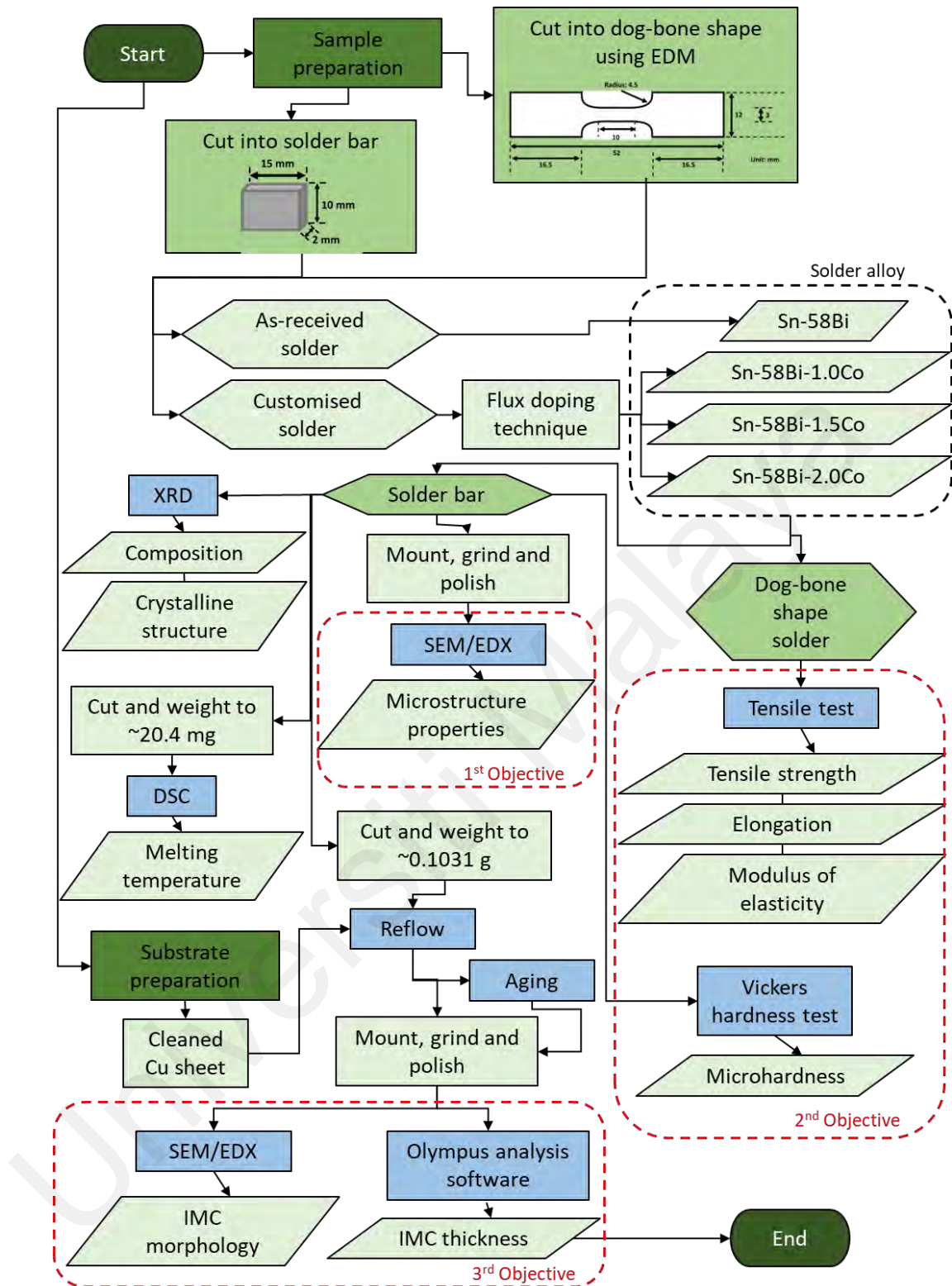


Figure 3.1: Methodology flow chart

3.2 Sample Preparation

The as-received pure Sn-58Bi solder was customised into Sn-58Bi-xCo solder where $x = 1.0, 1.5$ and 2.0 wt.% using flux doping technique. The as-received pure Sn-58Bi solder was in bar shaped where the width, length and thickness of the bar were 15

mm, 200 mm, and 2 mm, respectively. To customise the as-received solder, the as-received solder was cut and pre-cast into several different dimension depending on the characterisation and studies that was conducted. The cutting dimension was explained in detail in the sub-section.

The flux doping technique was conducted by preparing the doped mixture by manually stir Co powder ($\sim 2 \mu\text{m}$ particles size) with TF2000 Water Soluble Tacky Flux (SRA Soldering Products) for 30 minutes and equally spread the prepared mixture onto the pre-cast Sn-58Bi solder. The amount of Co powder added in the doped mixture was varied by the weight percentage of Co powder and Sn-58Bi solder. Figure 3.2 (a) show the weighing process of the solder on the weighing balance. Then, the pre-cast solder was heated using a horizontal tube furnace at 100°C for 10 hours. Figure 3.2 (b) and (c) show the cleaned solder and the customised solder after heated in the horizontal furnace, respectively. Deionised water was used to clean the residues of the doped mixture on the pre-cast solder. Figure 3.3 illustrate the overall process of alloying Co into the pure Sn-58Bi solder using flux doping technique.



Figure 3.2: Pictures of flux doping technique sample preparation process

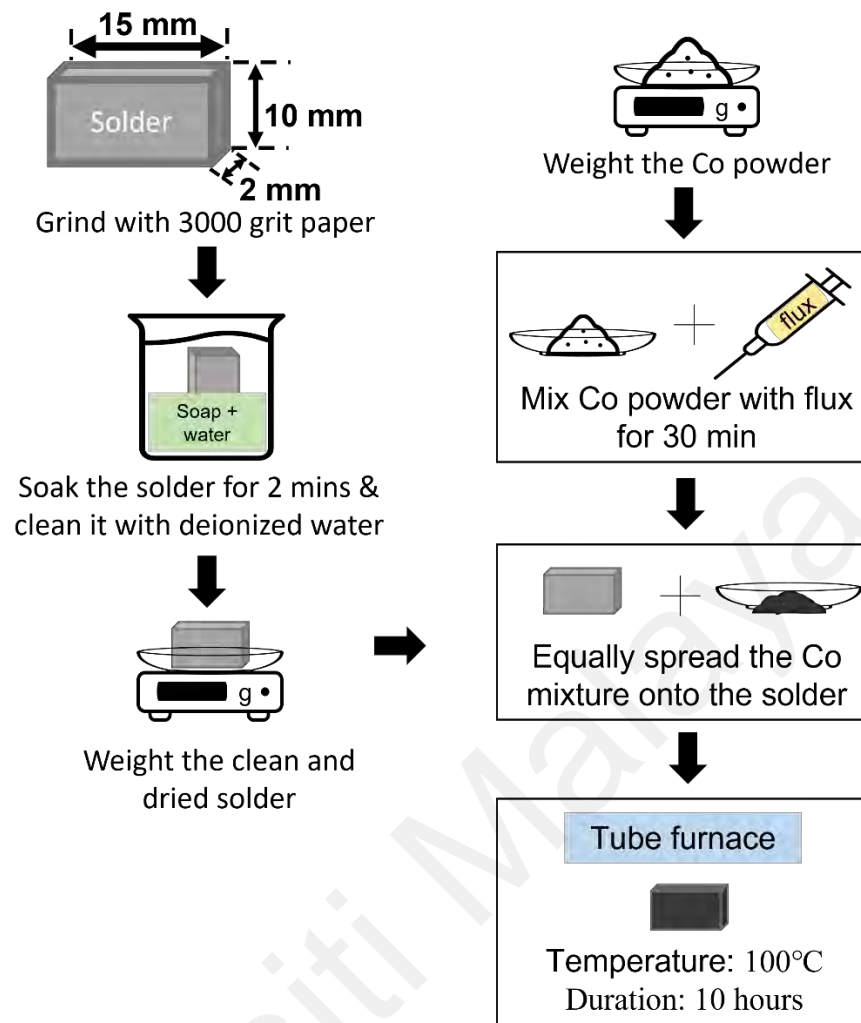


Figure 3.3: Flux doping technique schematic diagram

3.2.1 Thermal Characterisation, Microstructure Characterisation, Composition and Crystalline Structure Studies, Interfacial Studies, and Vickers Hardness Test

The prepared customised Sn-Bi-xCo solders for thermal characterisation, composition and crystalline structure studies, interfacial studies and Vickers hardness test were cut into small bar shaped using CNC wire electric discharge machining (EDM) where the width, length and thickness of the bar were 2 mm, 10 mm, and 2 mm, respectively. These small bar shaped solders then were manually cut into approximately 20.4 mg and 0.1031 g for thermal characterisation and interfacial studies, respectively.

3.2.2 Tensile Test

CNC wire electric discharge machining (EDM) was used to cut the as-received solder alloy for tensile test. The solder was machined into dog-bone shaped as illustrated in Figure 3.4 by following standard ASTM E8-04 dimension ratio. Then, the dog-bone shaped solder also was customised into Sn-58Bi-xCo solder where $x = 1.0, 1.5$ and 2.0 wt.% using flux doping technique.

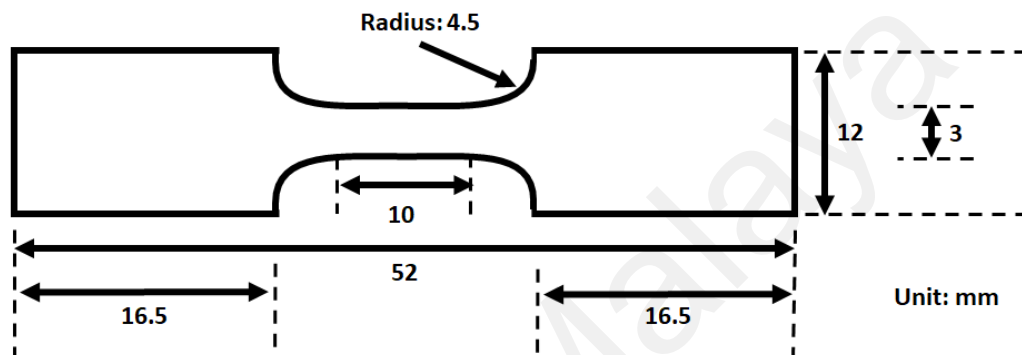


Figure 3.4: Schematic diagram of tensile test specimens

3.3 Sample Characterisation

The prepared customised solders were characterised its thermal, microstructure and mechanical properties for low temperature soldering application. The characterisation was analysed based on its melting temperature, structural, morphology, aging studies, tensile properties, and hardness studies.

3.3.1 Thermal Properties

The thermal behaviour of as-received and customised solders which focusing on the melting temperature of the solder were evaluated using differential scanning calorimeter (DSC). Approximately ~20.4 mg of the samples was weight to be used for thermal studies. The studies were repeated 3 times for each sample where every sample went through thermal treatment of 25 °C to 250 °C and chilled at room temperature with 10 °C/min rate.

3.3.2 Microstructure Properties

As-received pure Sn-Bi solder alloy and all customised Sn-Bi-xCo solders alloys was prepared for micro-examination. The standard metallographic was used in the process of cutting, mounting, grinding, and polishing the solder. The 240, 600, 800, 1200, 1500, 2000 and 3000 grit papers were used during the grinding process while the polishing process was done using diamond paste and colloidal silica with micron sizes of 9 μm , 3 μm , 1 μm and 0.02 μm . Scanning electron microscope (SEM) was used to characterized the microstructure of both as-received and prepared solders while the energy dispersive X-ray spectroscopy (EDX) was used to analysed elemental composition and the intermetallic compound (IMC) of the solder alloys. Figure 3.5 show the solder sample in mold of resin and hardener mixture for microstructure observation under SEM/EDX.

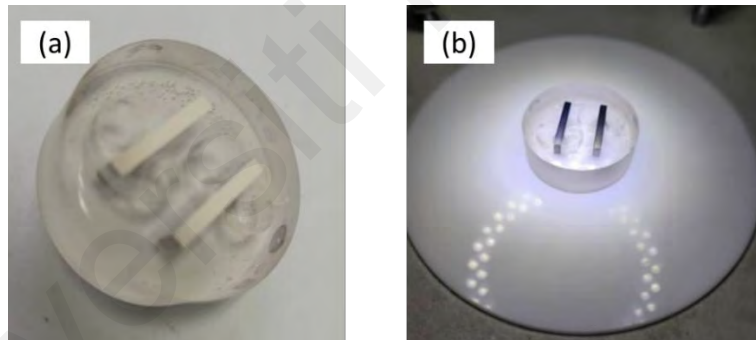


Figure 3.5: Samples for microstructure observation

3.3.3 Composition and Crystalline Structure Studies

The solders composition and crystalline structure were observed by conducting x-ray diffraction (XRD) using Malvern PANalytical (X'Pert³) with Cu K α radiation ($\lambda = 1.5418 \text{ \AA}$) in the range of $2\theta = 10^\circ - 90^\circ$. The scan step time and step size were 10s/step and 0.03° , respectively. The voltage and electron current of the generator were set to 40 kV and 40 mA, respectively.

3.3.4 Mechanical Properties

The mechanical properties of the solder were characterised by studying the tensile properties and microhardness and microstructure relationship of the solders.

Tensile test of the dog-bone shape samples was conducted at room temperature using the Instron 3369 Universal Testing Machine with static rating of ± 50 kN. The pure Sn-Bi solder samples was loaded to failure using crosshead speeds of 0.3, 0.6 and 1.5 mm/min. Before conducting the tensile test, the dog-bone shape tensile sample was marked as shown in Figure 3.6 (a) to make sure the necking happened at the gauge area. The sample was repetitively conducted with the same crosshead speed for 5 times and take the average. Figure 3.6 (b) show the position of the sample before starting the tensile test while Figure 3.6 (c) show the necking of the samples during the tensile test. The elongation, ultimate tensile strength, and modulus of elasticity of the pure Sn-Bi was evaluated. Then, 0.3 mm/min crosshead speed was chosen for further conduct tensile test for Sn-Bi-xCo (1.0, 1.5 and 2.0 wt.%) solders samples. The samples also were repetitively conducted with the same crosshead speed for 5 times and take the average. The gained tensile properties of the Sn-Bi-xCo solders samples were evaluated. After conducted tensile test, one of the post-tensile test fractured surface of each solder composition specimen was conserve and mold into a resin and hardener mixture as shown in Figure 3.6 (d) to observed the fractured surface. Similarly, the standard metallographic method was used to examine the fractured and deformation of the solders using SEM. The remaining post-tensile test samples stored in a container with with some silica gel as shown in Figure 3.6 (e).

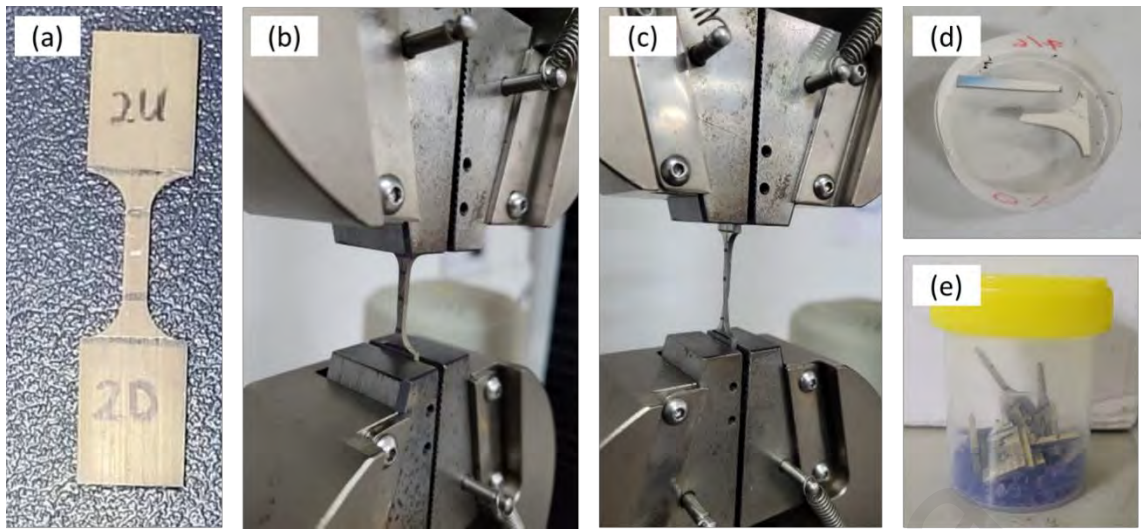


Figure 3.6: Samples of before and after tensile test.

Measurement of the Vickers hardness was conducted to examine the microhardness and microstructure relationship. The values of Vickers hardness were calculated using Equation 1:

$$HV = \frac{2P \sin \phi}{2d} \quad (\text{Equation 1})$$

where P is the applied load, ϕ is the apex angle of the indenter and d is the diagonals average length. The loading period and applied load were 5 s and 1 kgf, respectively. The microhardness test was conducted using Shimadzu HMV-G Micro Vickers Hardness tester. Five points were tested for each specimen and the mean values were gained.

3.3.5 Interfacial and Aging Studies

For interfacial studies, the commercial grade polycrystalline 0.3 mm thick copper (Cu) sheets were used as substrate. Before soldering, any oxide film present on the Cu sheets was removed by grinding, degreasing, and soaking the substrate in sulphuric acid (H_2SO_4) solution. The 3000 grit silica carbide paper was used for grinding then degreased with detergent for 2 minutes. The substrate then soaked into 10 vol.% H_2SO_4 solution for 1 minute. Then the film oxide-free substrate was rinsed with running distilled water

before acetone-drying the samples. The Cu substrate was equally spread with TF2000 Water Soluble Tacky Flux (SRA Soldering Products) and followed by the solder thin bar.

Figure 3.7 (a) show the solder which had been cut into smaller pieces before reflowing onto the Cu substrate. The average solder thin bar weight was approximately 0.1031 g. Figure 3.7 (b) show the position of solder and substrate before equally spread with TF2000 Water Soluble Tacky Flux and reflowed. Reflowed was conducted in horizontal tube furnace at 190 °C for 5 minutes. The reflowed sample was left in the horizontal tube furnace for 1 hour for cooling before letting it cool at room temperature outside of the furnace. The reflow process of the sample was illustrated in Figure 3.8. After the sample cooled at room temperature, the residual flux was cleaned by flushing the sample under running deionised water. The reflowed samples before and after cleaned with deionized water were shown in Figure 3.7 (c) and (d), respectively.

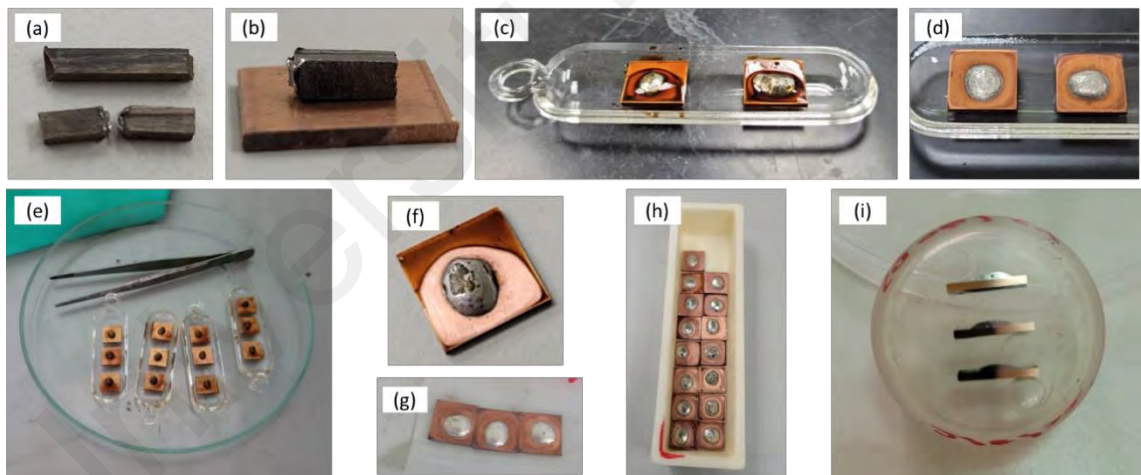


Figure 3.7: Samples for pure Sn-58Bi/Cu and Sn-58Bi-Co/Cu solder joint intermetallic studies and thermal aging studies

Figure 3.7 (e-g) show some Sn-Bi-Co/Cu solder joint samples for interfacial studies. The reflowed samples were prepared by standard metallographic specimen preparation for microstructural investigation. The microstructure of the bulk solder and the morphology of the IMCs formed at the solder/substrate interface was investigated by SEM and the composition of the IMCs was investigated by EDX. The Sn-Bi-Co/Cu solder

joint mold in the resin and hardener mixture for observation under SEM/EDX was shown in Figure 3.7 (i). IMC thickness was determined by dividing the IMC area by the length of the IMC using a built-in image analyser software in an Olympus SZX10 (Olympus, Tokyo, Japan) stereoscope.

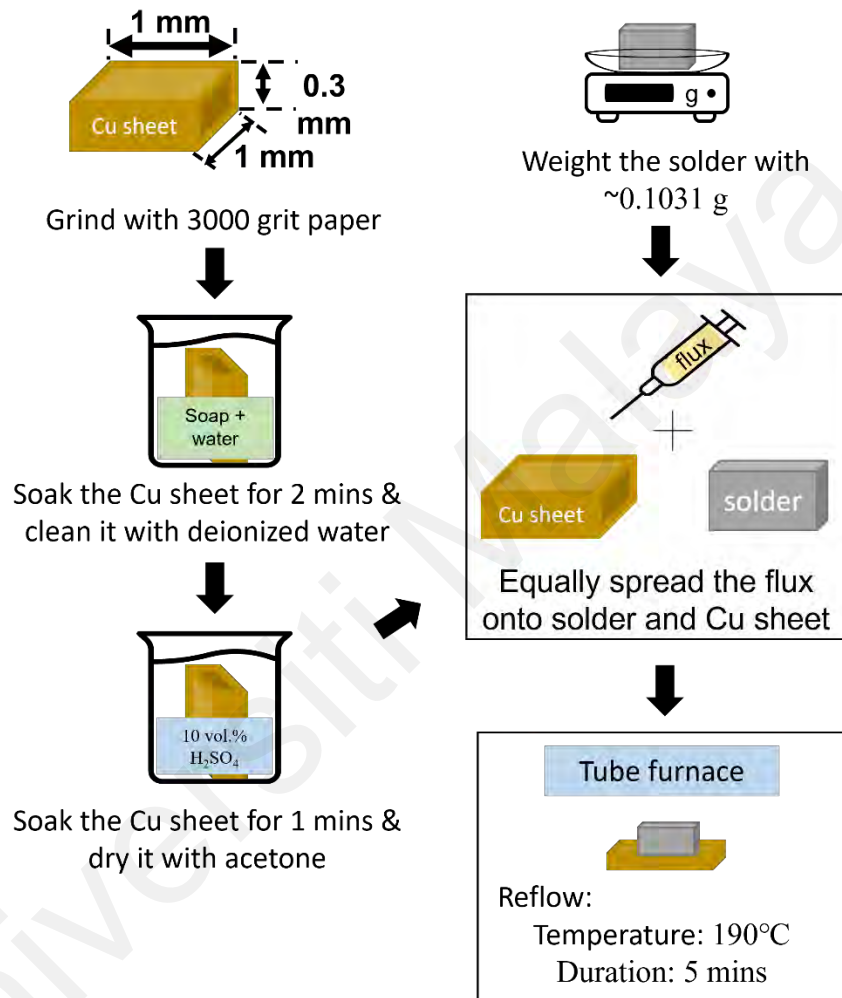


Figure 3.8: Schematic diagram of reflow process

For aging studies, Figure 3.7 (h) show some samples arranged in a crucible for thermal aging. The reflowed samples were set to thermal aging at $80^\circ C$ in an oven for 14, 28, 42, 56 and 72 days, respectively. Figure 3.9 illustrate the aging process of the reflowed samples. Sn-58Bi-1.5Co solder alloy with the optimum mechanical properties was thermally aged for 14, 28, 42, 56 and 72 days while all the other solders was only thermally aged at 28 and 56 days. Every thermal aging, 3 similar solder composition was aged. Then similarly, the microstructure of bulk solder, interface and IMC thickness were

examined using SEM, EDX and Olympus SZX10 stereoscope built-in image analyser software.

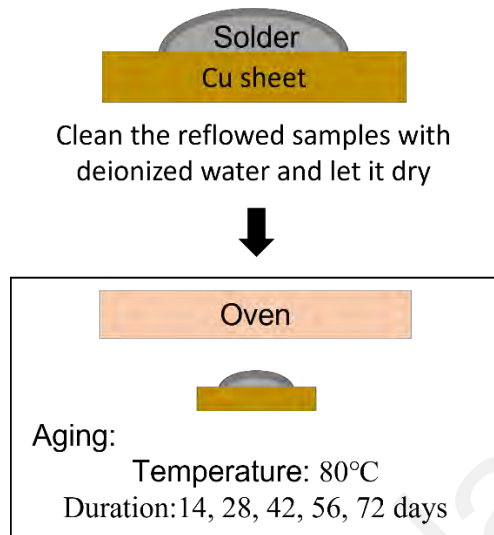


Figure 3.9: Schematic diagram of aging process

CHAPTER 4: RESULTS AND DISCUSSION

4.1 Introduction

This chapter will present and discuss the comprehensive results that was collected from thermal properties, microstructure properties, composition and crystalline structure studies, mechanical properties, interfacial and aging studies analysis of the samples. These properties will be compared among all 4 different prepared solder alloys composition and available reported literature.

4.2 Thermal Characterisation

The melting temperature of pure Sn-58Bi solder and Sn-58Bi-xCo ($x = 1.0, 1.5$ and 2.0 wt. %) solder were evaluated by taking the average melting temperature of 3 samples for each solder composition. Figures 4.1 and 4.2 shown the resulted average melting temperature of each solder composition. The melting temperature of the pure Sn-58Bi ($140.12\text{ }^{\circ}\text{C} \pm 3.55$) recorded a bit higher than the melting temperature reported by Li et al. ($139\text{ }^{\circ}\text{C}$), Lee et al. ($138\text{ }^{\circ}\text{C}$) and Wei et al. ($138\text{ }^{\circ}\text{C}$) (Li et al., 2020; Wei et al., 2021). However, the melting temperature of Sn-58Bi should be in the range of $\sim 139\text{-}140\text{ }^{\circ}\text{C}$. Amares et al. also reported in his literature that the melting temperature of Sn-Bi was $141.08\text{ }^{\circ}\text{C}$ which was $0.96\text{ }^{\circ}\text{C}$ more than the eutectic temperature of Sn-58Bi solder recorded in the Figure 4.1 (Amares et al., 2014). Thus, the recorded average melting temperature of Sn-58Bi solder was still in the range of reported values and could be acceptable.

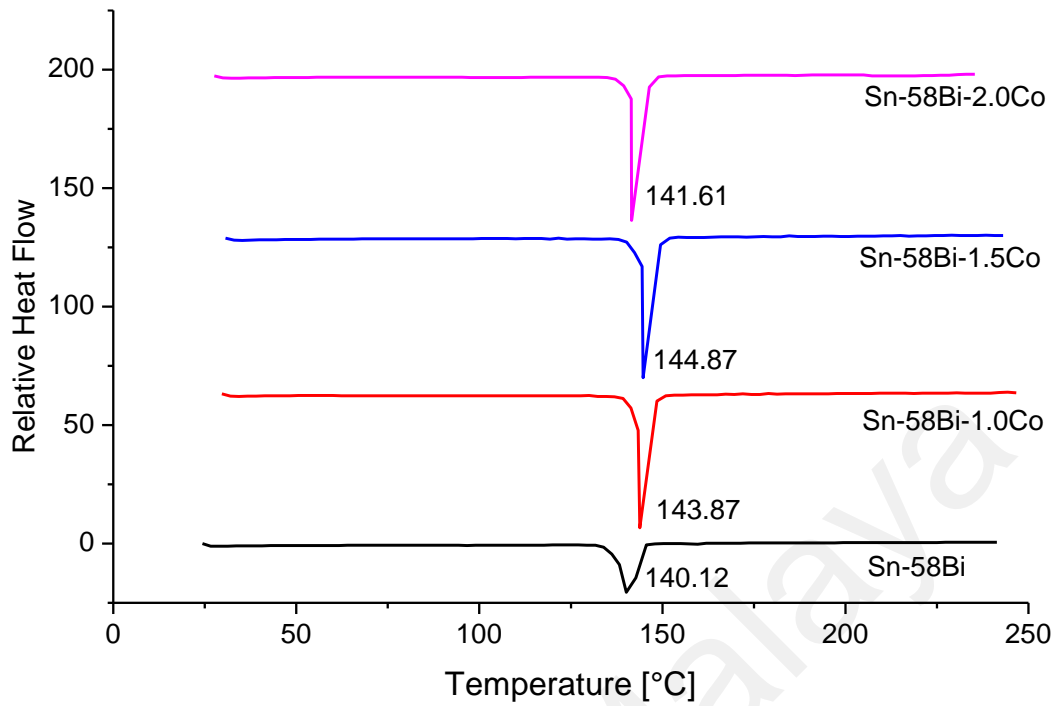


Figure 4.1: DSC curve with average melting temperature of Sn-58Bi-xCo solder alloy

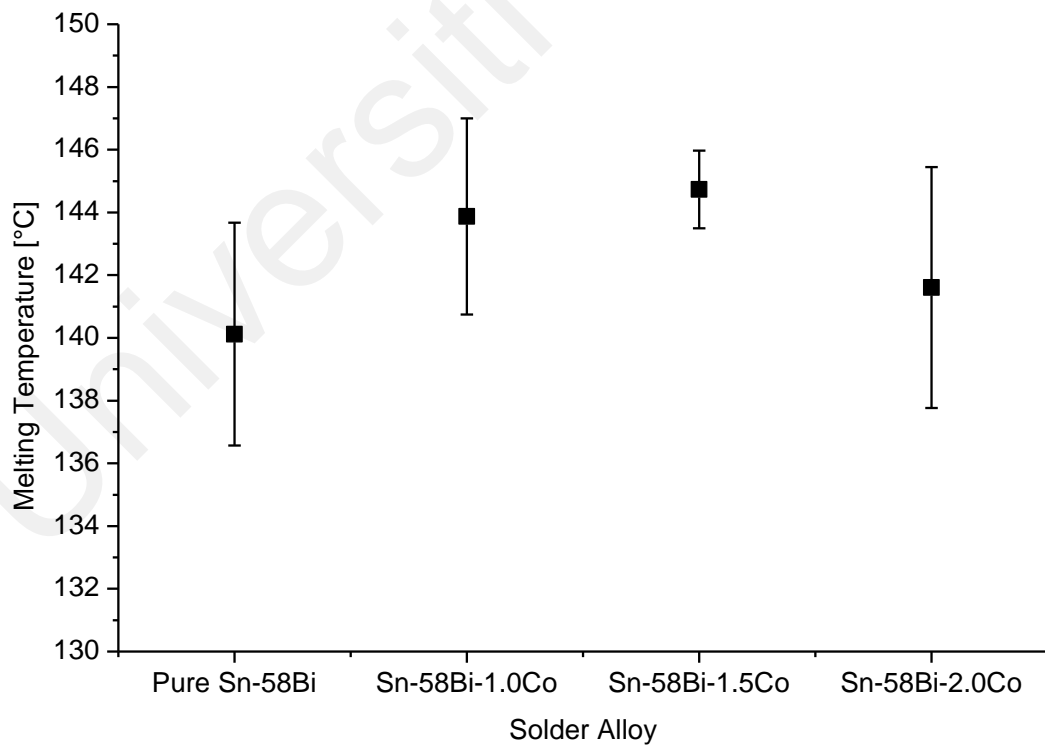


Figure 4.2: Average melting temperature of Sn-58Bi-xCo solder alloy

Besides, the alloying addition of Co into the Sn-58Bi solder show raise of average melting temperature in between 1.49-4.61 °C or 0.01-0.03 %. The present of Co was

proven to not change the Sn-58Bi solder melting temperature significantly. Moreover, a solder composition was considered low melting temperature solder type when the melting temperature was below 200°C. Thus, even though the melting temperature of Sn-58Bi-xCo ($x = 1.0, 1.5$ and 2.0) solder were a bit higher than pure Sn-58Bi solder, but it still not exceeding the melting temperature of Sn-Pb solder. The resulted melting temperature of Sn-58Bi-xCo solder were also lesser than Sn-3Ag-0.5Cu solder (217 °C) (Cheng et al., 2017). These shows that minor alloying of Co element into Sn-Bi solder could be considered to reinforce the drawbacks of pure Sn-Bi solder without altering the melting temperature much.

4.3 Microstructure Properties

The microstructure properties of the solders alloy were studied in terms of the structural and morphology of the solders. The studies focussing on the microstructure of the bulk solder before and after alloying with of Co. The microstructure of as-received and prepared Sn-Bi-xCo ($x = 1.0, 1.5$ and 2.0 w.t %) solders was analysed by conducting scanning electron microscope (SEM). Figure 4.3 shows the microstructure of the pure Sn-58Bi solder and Sn-58Bi-xCo solder alloy ($x = 1.0, 1.5$ and 2.0 wt. %). The microstructure of the pure Sn-58Bi solder and Sn-58Bi with Co alloying addition solders shows normal lamellar eutectic SnBi microstructure. The alloying addition of Co into the Sn-58Bi solder does not impose changes to the Sn-58Bi solder microstructure. The results were expected due to Co could stabilised the Sn-58Bi solder microstructure (Fan et al., 2020). Thus, the microstructure of the Sn-58Bi solder remain unchanged with the present of Co as the minor alloying element.

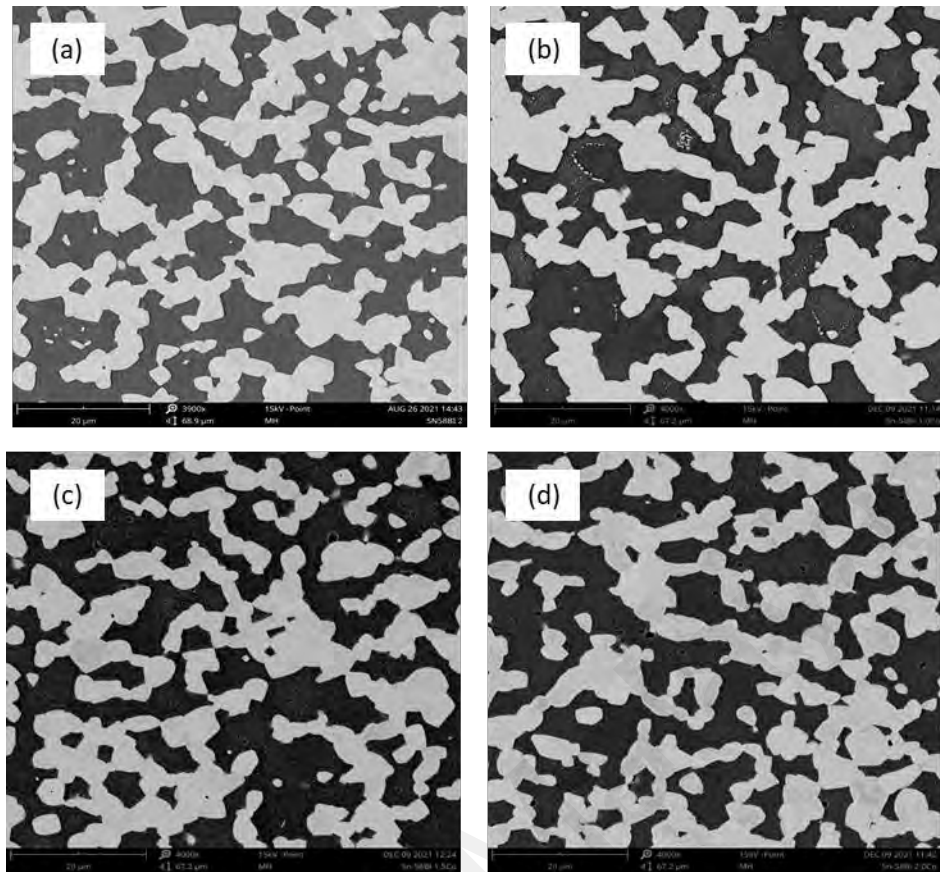


Figure 4.3: SEM images of (a) Sn-58Bi, (b) Sn-58Bi-1.0Co, (c) Sn-58Bi-1.5Co and (d) Sn-58Bi-2.0Co solder alloy.

To further prove the doping of Co into Sn-Bi solder was successfully done, element mapping and element mapping analysis were conducted. The Co distribution throughout the Sn-58Bi solder was observed by element mapping using EDX. Figures 4.4, 4.5 and 4.6 show the elemental mapping of Sn-58Bi-xCo ($x= 1.0, 1.5$ and 2.0 wt. %) solders. Based on the Figures, the dark and white region were Sn-rich and Bi-rich phase region, respectively. The phase region microstructure of the pure Sn-58Bi agreeable with research (Chen et al., 2016; Liu et al., 2016). All solder composition shows that Co was presented in a form of very small particles where it was spread all over the area in both regions.

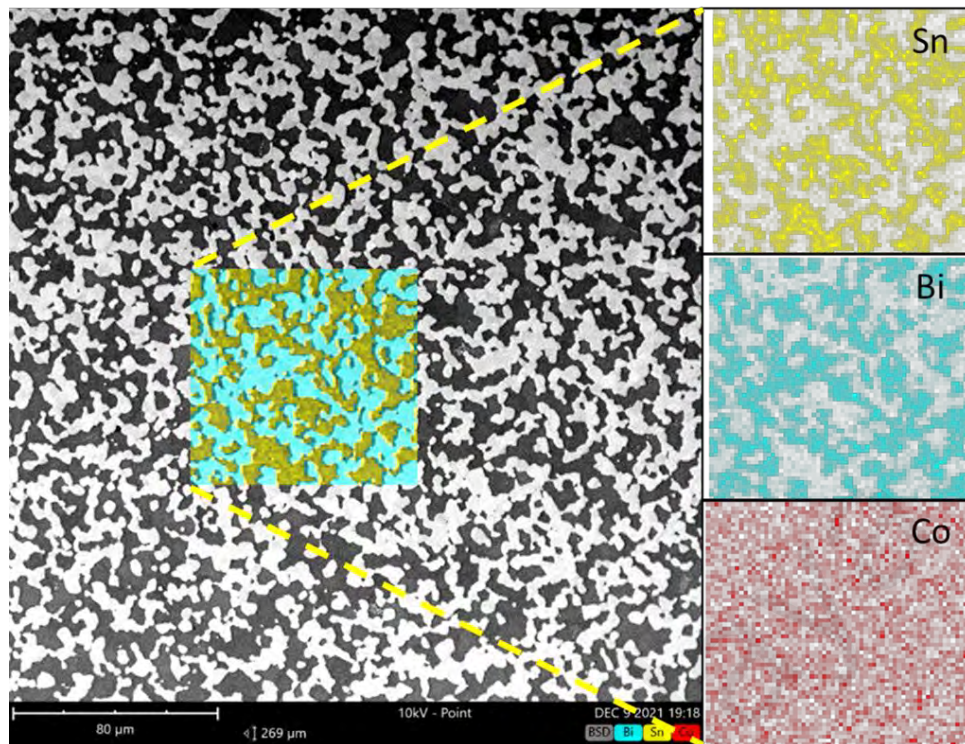


Figure 4.4: Element mapping of Sn-58Bi-1.0Co solder alloy.

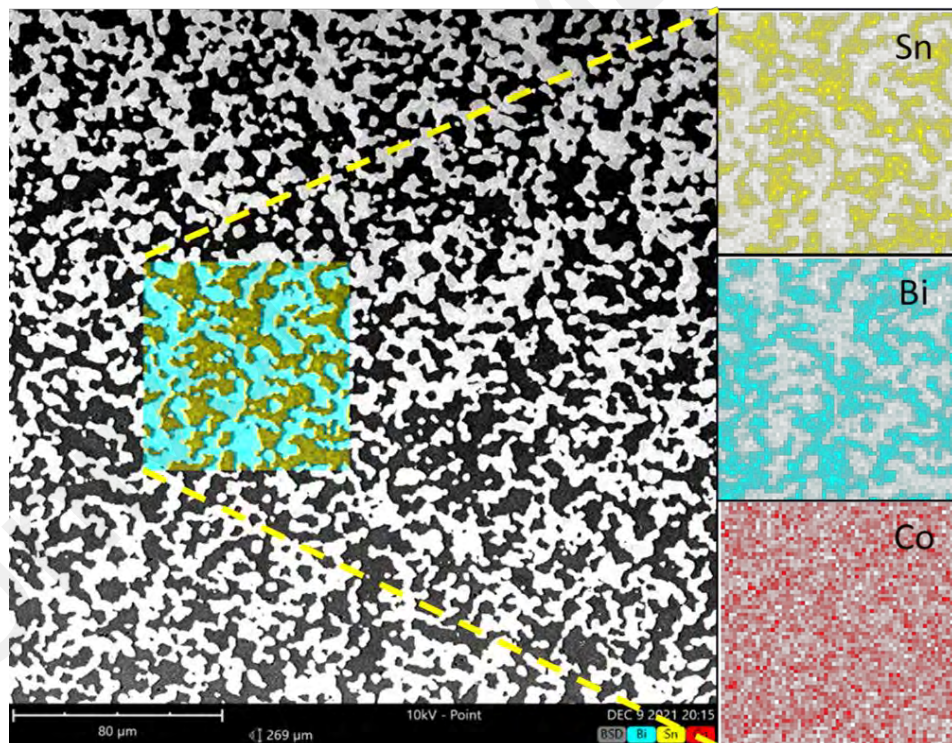


Figure 4.5: Element mapping of Sn-58Bi-1.5Co solder alloy

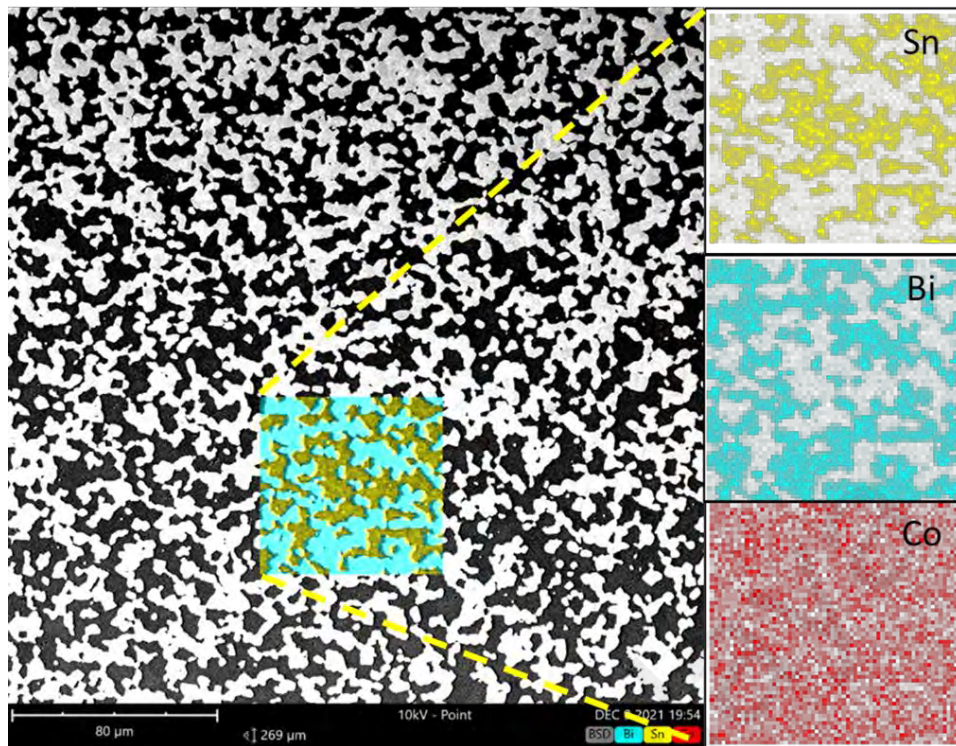


Figure 4.6: Element mapping of Sn-58Bi-2.0Co solder alloy

Figures 4.7, 4.8 and 4.9 show the line scanning of Sn-Bi-xCo ($x= 1.0, 1.5$ and 2.0) solders. Based on the resulted line scanning, the Co was presented in the Sn-Bi solder. Small amount of Co was successfully doped in the Sn-58Bi solder, and the Co element was distributed thoroughly in between both Sn-rich and Bi-rich phases.

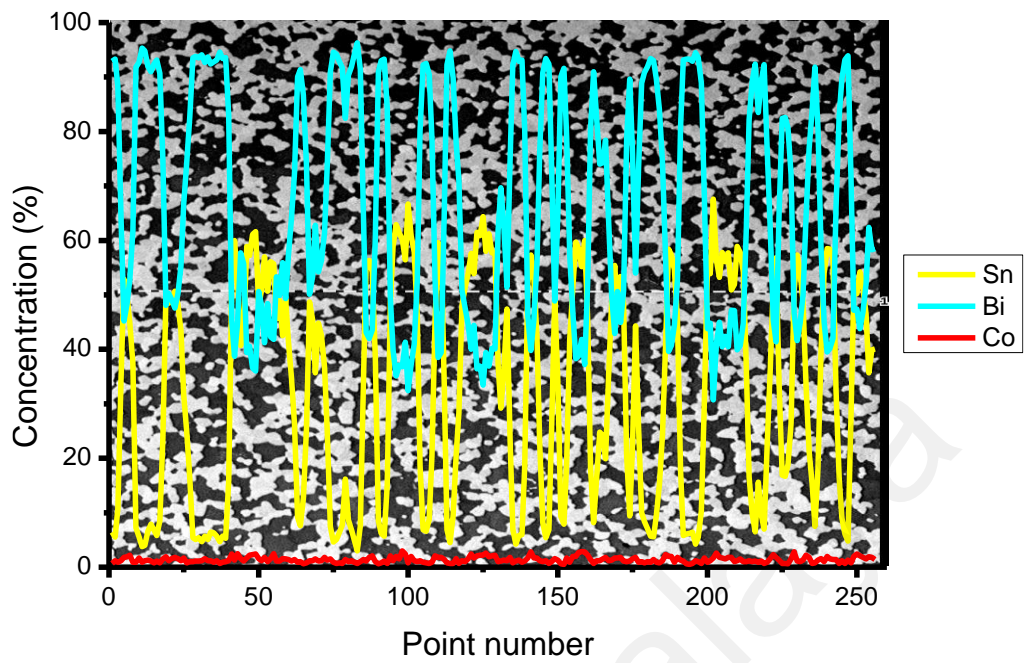


Figure 4.7: Line scanning of Sn-58Bi-1.0Co solder alloy

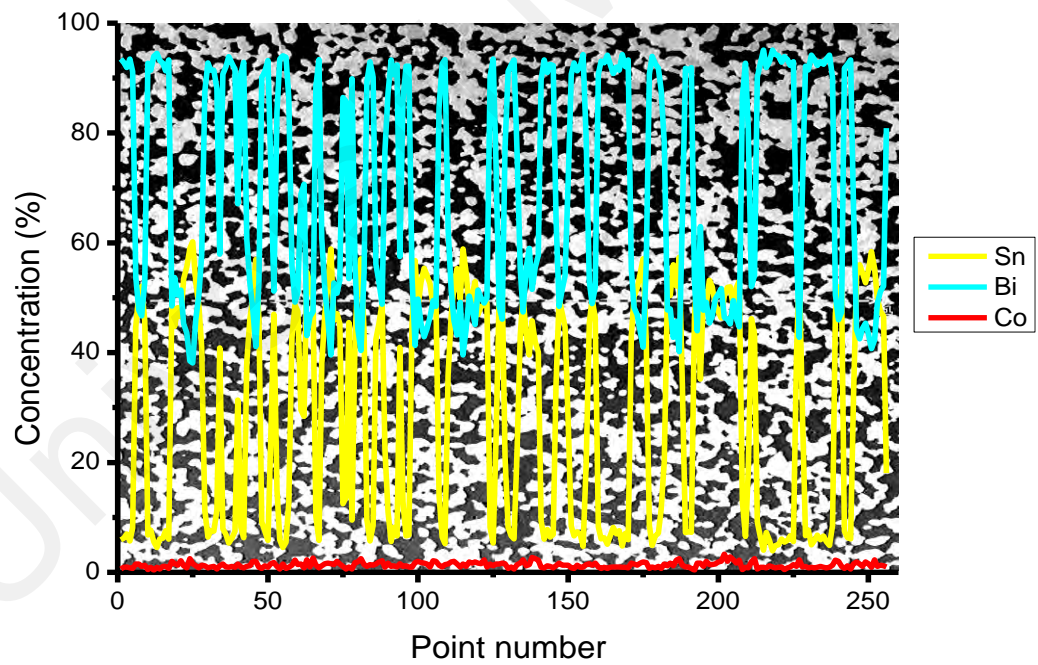


Figure 4.8: Line scanning of Sn-58Bi-1.5Co solder alloy

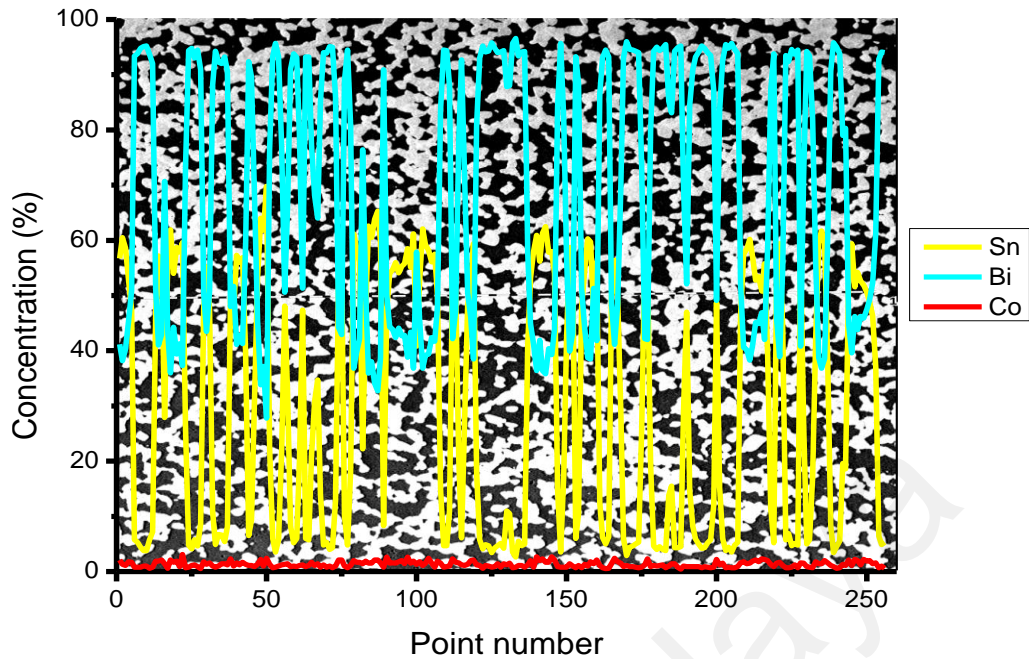


Figure 4.9: Line scanning of Sn-58Bi-2.0Co solder alloy

Table 4.1 shows the solder composition of Co added solders compared to the average amount of Co detected by line scanning. Regardless of the amount of Co added into the Sn-58Bi solder, the detected Co was ranges between 0.52-0.59%. To emphasize, the doped method was carried out by mixing flux with Co powder and doped it to Sn-58Bi solder by solid state doping. Firstly, different amount of Co was observed compared to the detected Co amount was possibly due to the Co particle was engulfed or rejected during doping diffusion Sn-58Bi solder (Haseeb & Leng, 2011). The atomic distribution or interatomic bonding between Sn-58Bi and Co possibly change due to substitution or penetration of Co atoms into Sn region (Yakymovych et al., 2016). Limit amount that can be detected would be below 0.60% regardless of how much Co is added.

Secondly, it is possible that Co particle will be oxidised when being exposed to the atmosphere during preparation and doping processes (Haseeb & Leng, 2011). Then, the Co could also be concentrated in the area where the line scan was not conducted which caused the detected amount of Co presented become lesser than the amount of Co added. However, through these line scanning results, it was evidence than the Co was successfully doped into the Sn-58Bi solder by using flux doping technique.

Table 4.1: Average amount of Co detected from the line scanning

| Solder alloy | Amount of Co added (wt.%) | Average amount of Co detected (wt.%) |
|---------------------|----------------------------------|---|
| Sn-58Bi-1.0Co | 1.0 | 0.52 |
| Sn-58Bi-1.5Co | 1.5 | 0.59 |
| Sn-58Bi-2.0Co | 2.0 | 0.53 |

4.4 Composition and crystalline structure studies

The composition of the solder was further studied by conducting XRD. The XRD plot of each solder composition was presented in Figure 4.10. The XRD plot was analysed using HighScore Plus software. Referred from Joint Committee on Powder Diffraction Standards (JCPDS) data card number 98-006-4703, there were obvious peak seen in Figure 4.10 which matched the Bi 2 θ at 27.17 °, 37.96 °, 39.62 °, 46.02 °, 48.70 °, 56.03 °, 64.51 ° and 70.79 °. The peak which matched JCPDS data card number 98-004-3613 for Sn 2 θ were 30.63 °, 32.01 °, 43.87 °, 44.87 °, 55.32 °, 62.50 °, 72.40 ° and 79.47 °. The resulted crystallographic of the Bi and Sn were hexagonal and tetragonal crystal systems, respectively.

The Sn-58Bi solder with Co alloying element resulted some peak of Co₃Sn₂. The Co₃Sn₂ 2 θ matched JCPDS data card number 98-062-5259 were 21.73 °, 41.66 °, 67.37 ° and 88.46 ° while JCPDS data card number 98-010-2675 was 59.39 °. The crystallographic of Co₃Sn₂ of JCPDS data card number 98-062-5259 and 98-010-2675 were orthorhombic and hexagonal crystal systems, respectively. Thus, through this XRD analysis, it was proven that the cobalt was successfully alloyed into Sn-58Bi solder and form Co₃Sn₂. It also agreeable with Figure 2.6 where at eutectic composition, Co₃Sn₂ was expected form.

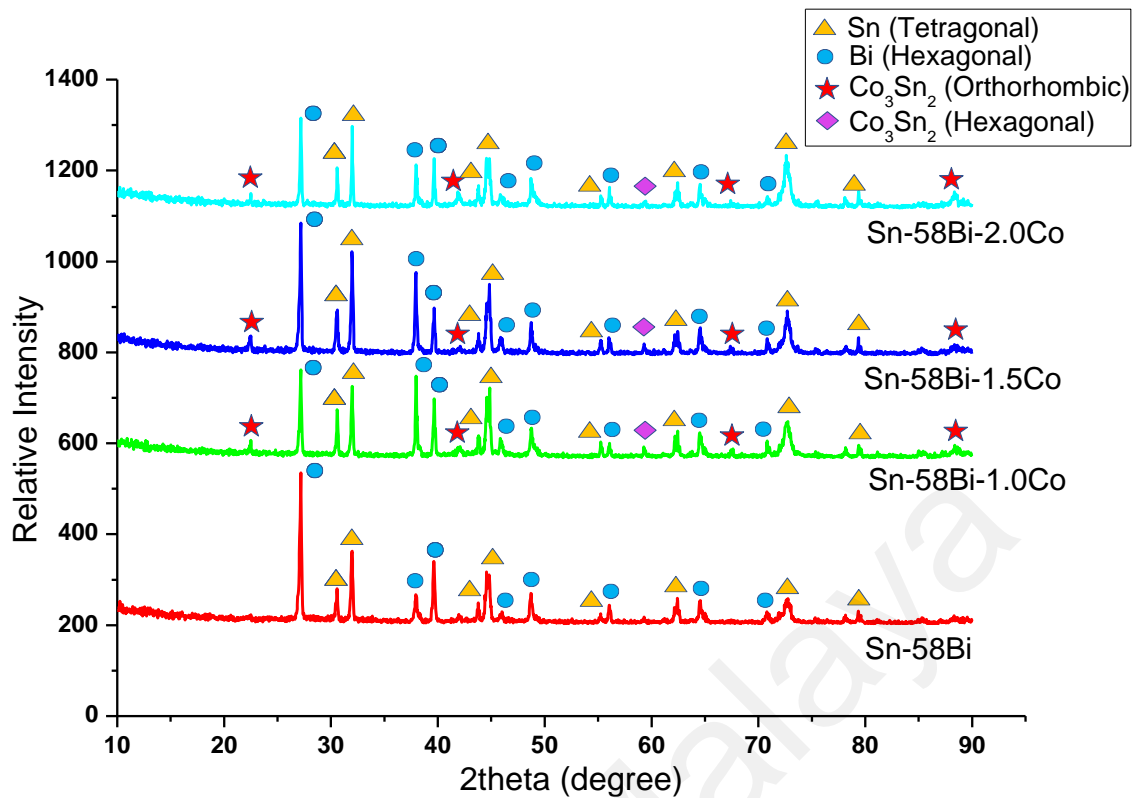


Figure 4.10: XRD plot of pure Sn-58Bi solder and Sn-58Bi-xCo solder

4.5 Mechanical Properties

The mechanical properties of the pure Sn-58Bi solder and Sn-58Bi-xCo ($x = 1.0$, 1.5 and 2.0 wt. %) solder were evaluated by conducting 2 different tests which is tensile test and Vickers hardness test. The fractography of the post-tensile also was also evaluated.

4.5.1 Tensile Properties

The tensile properties of pure Sn-58Bi solder and Sn-58Bi-xCo ($x = 1.0$, 1.5 and 2.0 wt. %) solders were observed in 2 different perspectives. Firstly, the pure Sn-58Bi solder tensile test was conducted by varying the strain rates to observe the effect of strain rates on the solder. Secondly, 0.0005 s^{-1} strain rate was chosen to further study the tensile properties differences between pure Sn-58Bi solder and Sn-58Bi-xCo ($x = 1.0$, 1.5 and 2.0 wt. %) solders.

The elongation, modulus of elasticity and tensile strength of pure Sn-58Bi solder at 0.0005, 0.001 and 0.0025 s⁻¹ strain rates at room temperature was tabulated in Table 4.2. The elongation decreased while the modulus of elasticity increased with the increasing of strain rates. These results were expected because Sn-58Bi solder alloy was reported to have poor ductility at high strain rate and low temperature (Maruya et al., 2017; Silva et al, 2017). Table 4.2 indicates that Sn-58Bi solder had highest tensile strength at 0.0025 s⁻¹ strain rate. Higher strain rates resulted a higher tensile strength where 0.0025 s⁻¹ strain rate result in 16.4% and 9.9% higher tensile strength than 0.001 s⁻¹ and 0.0005 s⁻¹ strain rates, respectively.

These also agreeable with Chen et al. where he states that Sn-Bi solder tensile properties was highly affected by strain rate (Chen et al., 2016). The gained tensile strength of Sn-58Bi solder at 0.0005 and 0.001 s⁻¹ strain rates does not differ much from the reported tensile strength values. However, at 0.0005 s⁻¹ strain rate, the gained elongation and modulus of elasticity values recorded 70.5% and 99.0% higher compared to Mokhtari & Nishikawa reported values, respectively. Thus, difference in the elongation and modulus of elasticity results could be due to different solder alloy production manufacturing, tensile test static rating or tensile sample dimension.

Table 4.2: Tensile properties of Sn-58Bi solder alloy at different strain rates

| Gauge length × thickness (mm) | Strain rate (s⁻¹) | Elongation (%) | Modulus of elasticity (GPa) | Tensile strength (MPa) | References |
|--|---|---------------------------|--|---------------------------------------|-------------------|
| 10 × 2 | 0.0005 | 75.90 ± 23.20 | 4.17 ± 0.76 | 57.02 ± 0.39 | This work |
| | 0.001 | 66.86 ± 19.34 | 4.72 ± 0.39 | 53.43 ± 2.30 | |
| | 0.0025 | 55.05 ± 30.02 | 11.12 ± 7.02 | 62.96 ± 4.03 | |

| | | | | | |
|--------|--------|--------------|------------|--------------|----------------------------|
| 10 × 1 | 0.0005 | 36.30 ± 2.50 | 12.5 ± 1.0 | 52.00 ± 1.00 | Mokhtari & Nishikawa, 2016 |
| 10 × 2 | 0.0005 | 37.50 | - | 49.00 ± 1.00 | Zhou et al., 2018 |
| 10 × 1 | 0.001 | 34.00 ± 4.50 | - | 52.00 ± 1.50 | Zhou et al., 2019 |

Figures 4.11 and 4.12 shown the modulus of elasticity and tensile strength of pure Sn-58Bi solder and Sn-58Bi-xCo (x= 1.0, 1.5 and 2.0 wt. %) solders at 0.0005 s⁻¹ strain rate at room temperature. Based on Figure 4.11, Sn-58Bi-1.0Co solder had the highest modulus of elasticity compared to pure Sn-Bi solder and other Sn-58Bi-Co solder. The alloying addition of 1.5 and 2.0 wt.% of Co into Sn-58Bi solder slightly decrease the solder modulus of elasticity by 0.72 % and 3.84 % compared to the pure Sn-58Bi solder alloy, respectively. Figure 4.12 shown that all three Sn-58Bi-Co solder composition results in higher tensile strength than pure Sn-58Bi solder. The alloying addition of Co into Sn-58Bi solder successfully increase the tensile strength of the solder. The increasing trend of the solder tensile strength were inconsistent where the solder tensile strength started to decrease for Sn-58Bi-2.0Co solder. However, the tensile strength of Sn-58Bi-2.0Co solder was 2.95 % higher than the pure Sn-58Bi solder.

As for the solder composition with most optimum tensile properties, Sn-58Bi-1.5Co solder shown the best combination. The modulus of elasticity and tensile strength of Sn-58Bi-1.5Co solder recorded stable properties. Compared to Sn-58Bi solder, the modulus of elasticity Sn-58Bi-1.5Co solder only drop slightly by 0.7%, but the tensile strength increased by 5.6%, and Sn-58Bi-1.5Co solder recorded the highest tensile strength. This high tensile strength could be an added advantage of the solder where the solder could withstand much more tension while in service and strengthen the solder and substrate joint. Thus, the amount of Co added into the Sn-58Bi solder highly affected the modulus of elasticity and tensile strength of the solders afterwards. The increase in Co

wt.% alloying addition into Sn-58Bi solder did not proportionally increase the modulus of elasticity and tensile strength of the solders.

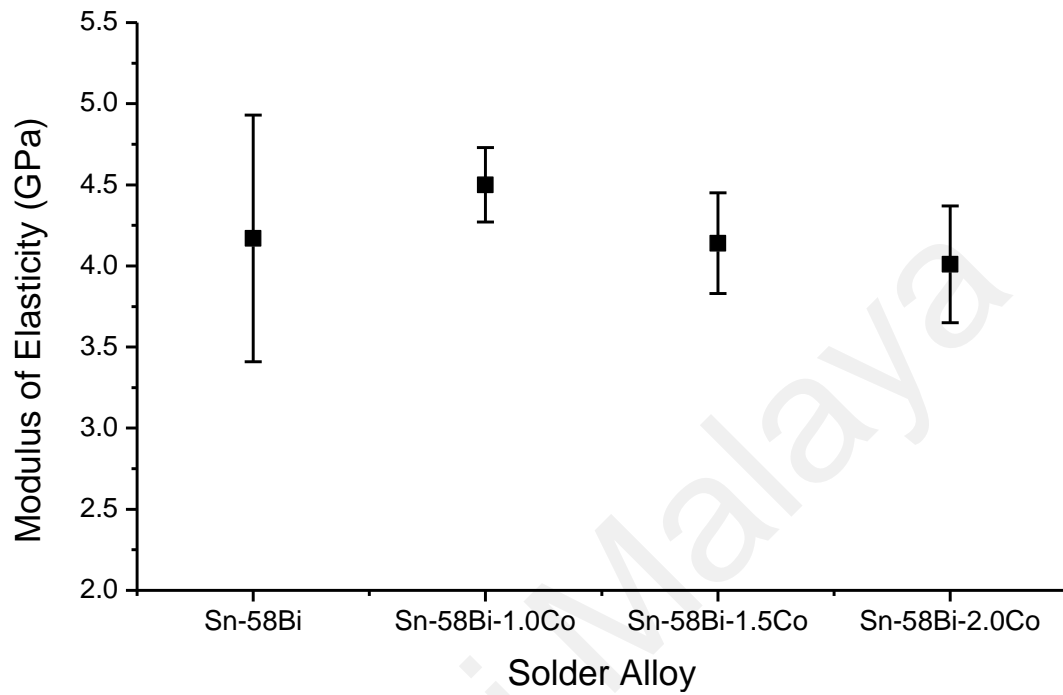


Figure 4.11: Modulus of elasticity of pure Sn-58Bi solder and Sn-58Bi-xCo (x = 1.0, 1.5 and 2.0) solder

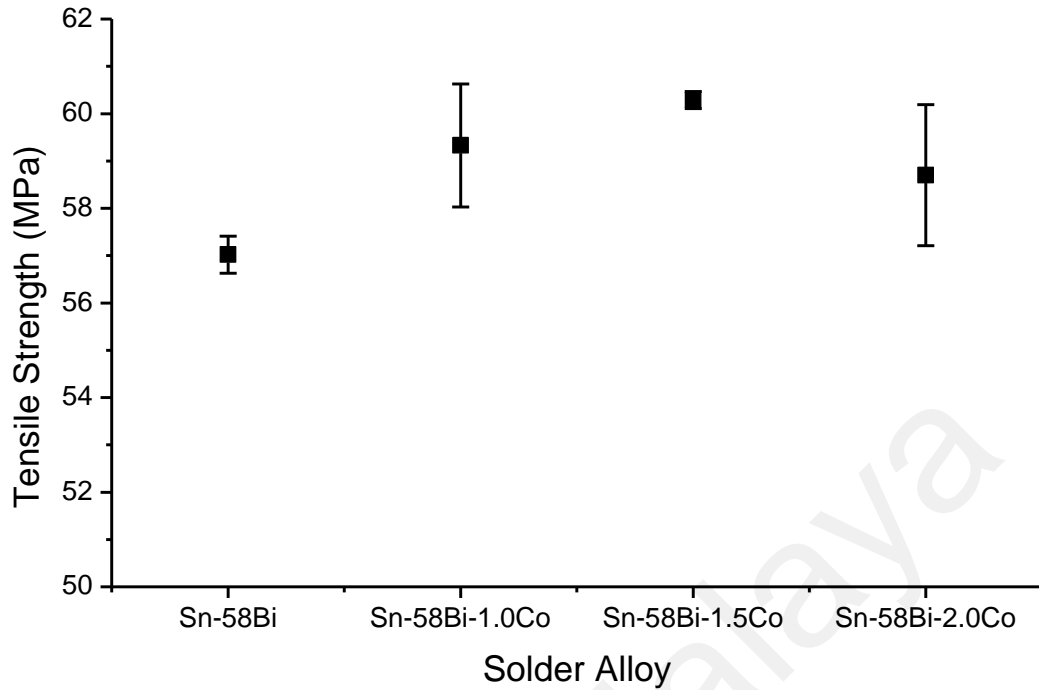


Figure 4.12: Tensile strength of pure Sn-58Bi solder and Sn-58Bi-xCo (x = 1.0, 1.5 and 2.0) solder

4.5.2 Fractography Studies

The fractography of the tensile test specimen was examined by selecting 1 out of 5 post-tensile test fractured tensile specimens. The fractured surface of the pure Sn-58Bi solder and Sn-Bi-Co solder post-tensile test specimens was observed using SEM at 2 different views. The red box outline in Figure 4.13 (a) show the surface area of the side view while Figure 4.13 (b) show the surface area of cross-section view of the post-tensile test specimen.

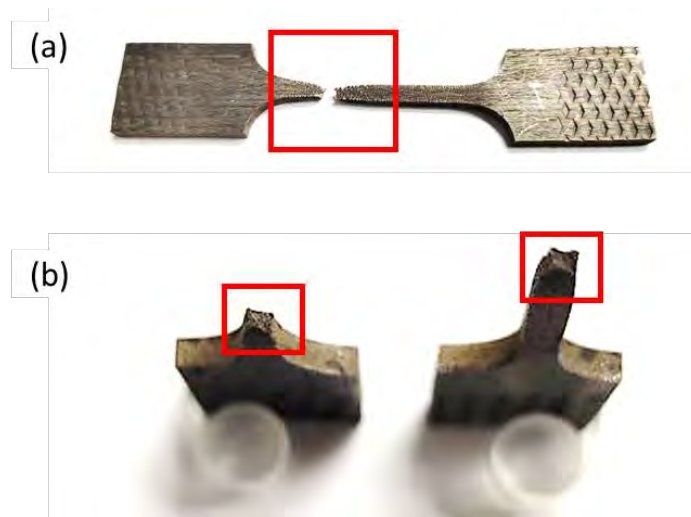


Figure 4.13: (a) Side view and (b) cross-section view of fractured surface observations position

Figure 4.14 shown the side view of post-tensile fractured surface of Sn-58Bi solder at different strain rates. Based on Figure 4.14 (a) and (b), the cracking near the breaking area becomes bigger and towards tearing with increasing strain rates. This caused the modulus of elasticity to decrease at increasing strain rates. Figure 4.14 (a) and (b) also show that necking phenomenon happen at the before breaking while Figure 4.14 (c) show that there was nearly no necking. At 0.0025 s^{-1} strain rate, the nearly no necking phenomenon results in the lowest elongation.

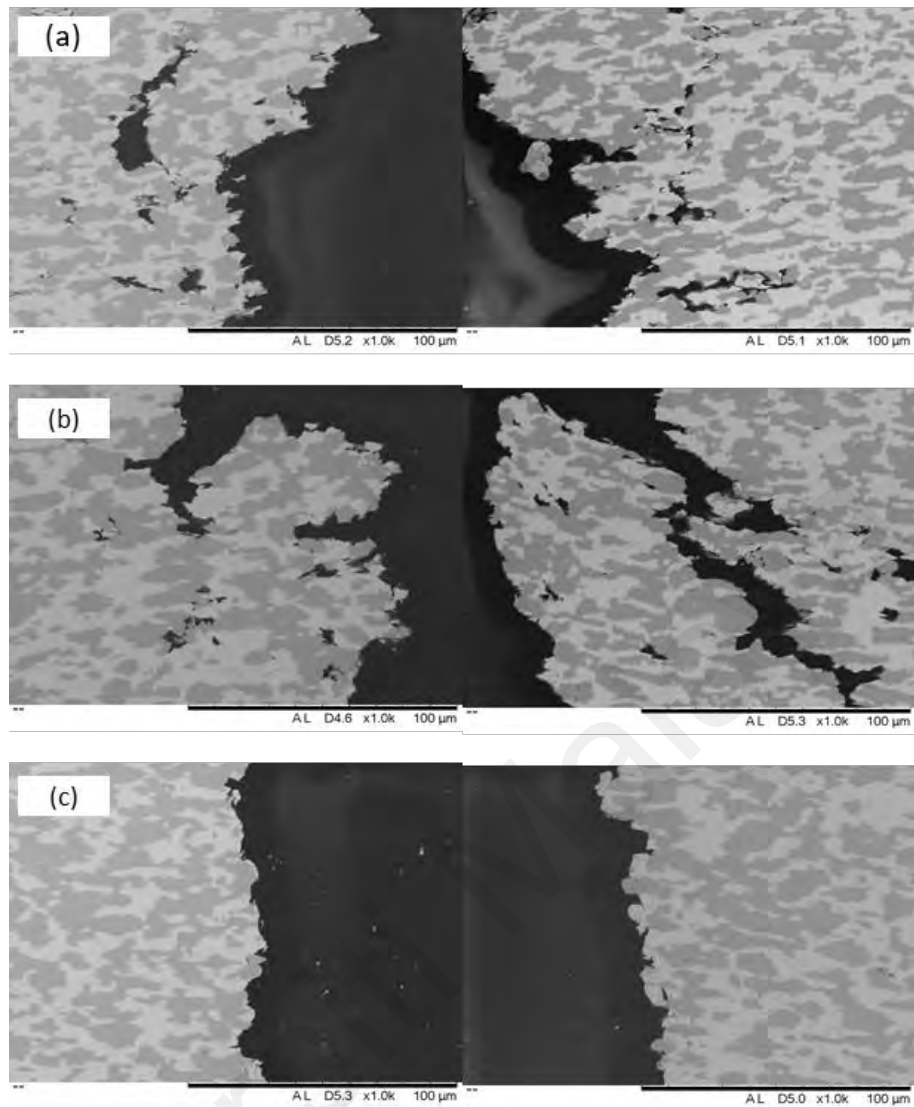


Figure 4.14: SEM images of pure Sn-58Bi solder tensile fractured surface side view at (a) 0.0005 s^{-1} , (b) 0.001 s^{-1} and 0.0025 s^{-1} strain rates

The fractured surface of pure Sn-58Bi solder at different strain rates from the cross-section view was shown in Figure 4.15. Based on Figure 4.15, the fractured surface become flatter and lesser dimples were observed as the strain rates increase. The decrease in the presence of dimples indicates that toughness and ductility of the solder fluctuated (Chen et al., 2016). At 0.0025 s^{-1} strain rates, there was nearly no presence of bulge fracture surface as the surface become flatter. It agreeable with Table 4.2 where the elongation decreases when the strain rates increase.

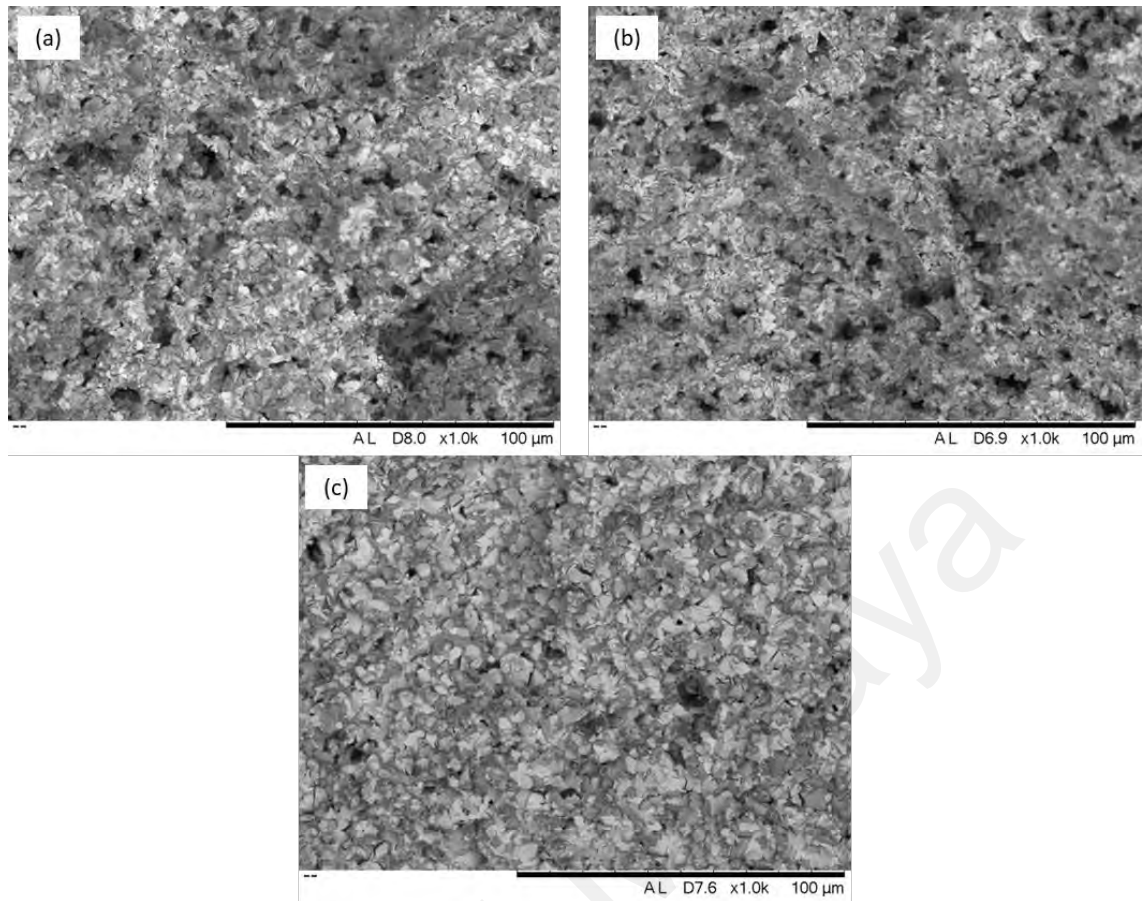


Figure 4.15: SEM images of pure Sn-58Bi solder tensile fractured surface cross-section view at (a) 0.0005 s^{-1} , (b) 0.001 s^{-1} and 0.0025 s^{-1} strain rates

The tensile fractured surface side view of pure Sn-58Bi solder and Sn-58Bi-Co solders were shown in Figure 4.16. Figure 4.16 show that necking phenomenon happen at all solder composition samples. Figure 4.16 (a) shown that there was a big crack near the tensile breaking region which may cause the pure Sn-58Bi solder recorded the lowest tensile strength. From Figure 4.16 (c), lesser cracks forms near the tensile breaking region of Sn-58Bi-1.5Co solder compared to other solders which than result in the highest tensile strength. Figure 4.16 (c) and (d) also show that the breaking area of Sn-58Bi-1.5Co solder and Sn-58Bi-2.0Co solder were mostly composed of Bi-rich phase. While the breaking area of the pure Sn-58Bi solder was mostly at Sn-rich phase. Thus, the cracking and breaking area of the fractured surface also influenced the tensile strength of the solders.

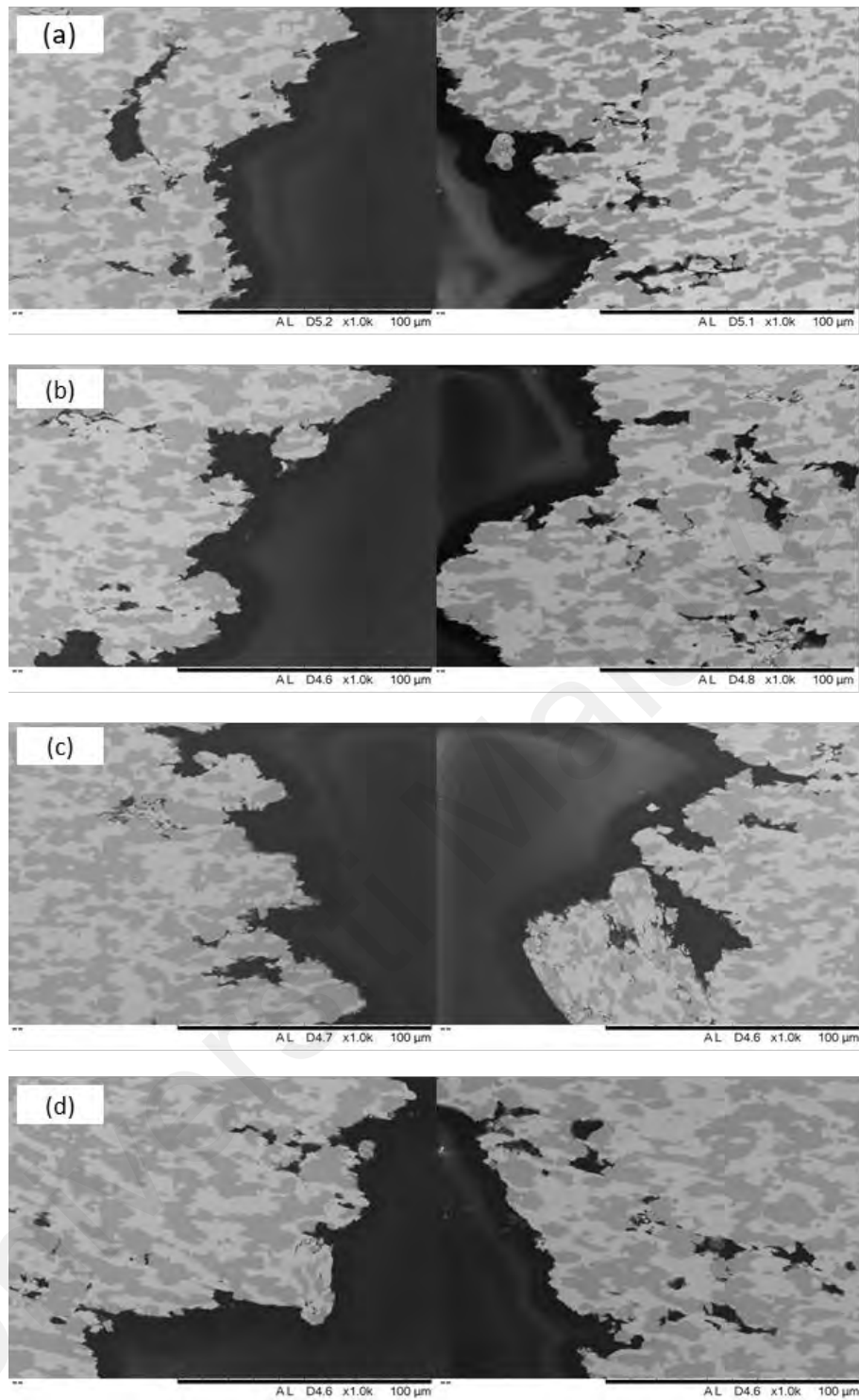


Figure 4.16: SEM images of tensile fractured surface side view of (a) pure Sn-58Bi, (b) Sn-58Bi-1.0Co, (c) Sn-58Bi-1.5Co and (d) Sn-58Bi-2.0Co solders at 0.0005 s^{-1} strain rate.

The cross-section view of pure Sn-58Bi solder and Sn-58Bi-Co solders fractured surface were shown in Figure 4.17. All solders show ductile fracture mode where bulge fracture was observed. The presence of dimples increases with increasing Co amount. These indicated that the ductility and toughness of solder improve with the alloying

addition of Co. It also agreeable with Figure 4.12 where the tensile strength increases with the alloying addition of Co.

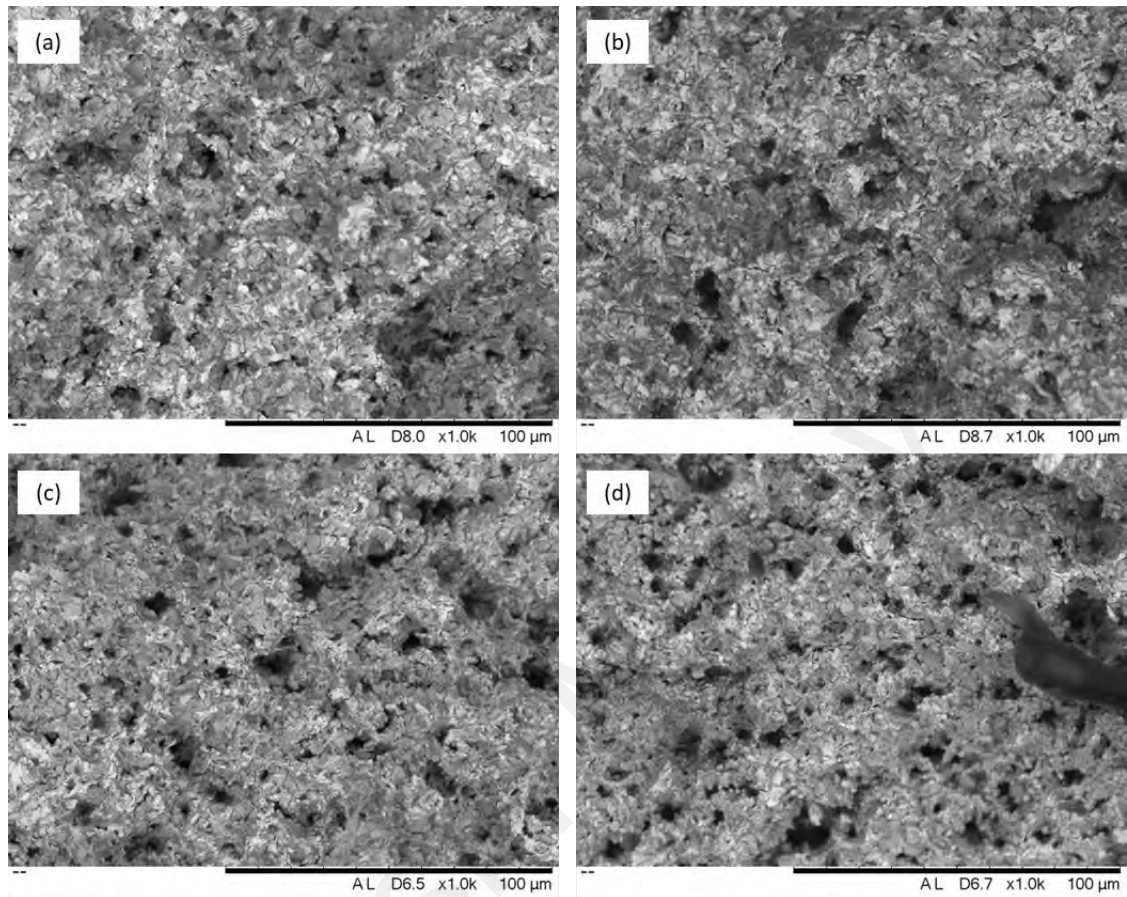


Figure 4.17: SEM images of tensile fractured surface cross-section view of (a) pure Sn-58Bi, (b) Sn-58Bi-1.0Co, (c) Sn-58Bi-1.5Co and (d) Sn-58Bi-2.0Co solders at 0.0005 s^{-1} strain rate.

4.5.3 Microhardness

The microhardness of the solders was tested by conducting Vickers hardness test. Microhardness test was important to evaluate the durability and strength of the solder upon services. Table 4.3 summarised the average microhardness values recorded. Based on Table 4.3, the other reported literatures recorded the average microhardness of Sn-58Bi solder was 19.70 HV to 24.38 HV while this work of the pure Sn-58Bi solder recorded 19.18 HV average microhardness. The microhardness of the pure Sn-58Bi solder was lesser than the other reported literatures. However, the applied load and holding time of the microhardness test conducted by the other reported literatures were lesser and longer than this work applied load and holding time, respectively. Li & Chan

conducted the microhardness test at 2.942 N applied load had lower microhardness value than Wei et al. and Hu et al. whose conducted microhardness test at 0.981 N applied load. These indicates that higher applied load, decreased the microhardness value. Thus, in this work, the recorded average microhardness value of pure Sn-58Bi solder was acceptable.

Then, 1.0 and 2.0 wt. % alloying addition of Co into Sn-58Bi solder decrease the average microhardness compared to pure Sn-58Bi solder. The average microhardness of Sn-58Bi-1.0Co solder and Sn-58Bi-2.0Co solder decrease by 3.50 % and 0.31 %, respectively. However, Sn-58Bi-1.5Co solder successfully increase the average microhardness by 1.76 % compared to pure Sn-58Bi solder. The increase of the microhardness value indicates that addition of 1.5 wt. % of Co could enhanced the strength of pure Sn-58Bi solder. These may be due to the dispersion of Co particle in the Sn-58Bi-1.5Co solder capable to act as grain refinement strengthening in the Sn-Bi solder matrix (Wei et al. 2021; Li & Chan, 2015). While, increasing the amount of added wt. % of Co to 2.0 only decrease the average microhardness slightly compared to pure Sn-58Bi solder. Thus, Co minor alloying addition still could enhance the durability and strength of the solder but at some certain addition amount only.

Table 4.3: Average microhardness values

| Solder | Applied load (N) | Holding time (s) | Average microhardness (HV) | References |
|---------------|------------------|------------------|----------------------------|-----------------|
| Pure Sn-58Bi | 9.807 | 5 | 19.18 ± 0.52 | This work |
| Sn-58Bi-1.0Co | | | 18.52 ± 0.36 | |
| Sn-58Bi-1.5Co | | | 19.52 ± 0.47 | |
| Sn-58Bi-2.0Co | | | 19.12 ± 0.56 | |
| Sn-58Bi | 0.981 | 10 | 24.38 | Hu et al., 2015 |
| Sn-58Bi | 0.981 | 10 | 20.60 | Wei et al. 2021 |
| Sn-58Bi | 2.942 | 12 | 19.70 | Li & Chan, 2015 |

4.6 Interfacial and Aging Studies

The intermetallic compound morphology and thickness developed at the solder/substrate interface before and after thermal aging was studied. The interfacial and aging studies between the solder and Cu substrate were observed by SEM, EDX and calculating the intermetallic compound (IMC) layer thickness. The aging studies was evaluated up to 70 days.

4.6.1 Interfacial Studies

Figure 4.18 shows that the IMC layer form at pure Sn-58Bi/Cu solder and Sn-58Bi-xCo/Cu ($x=1.0, 1.5$ and 2.0 wt. %) solders after reflowed. There were 2 IMC layers observed at the interface which were Cu_3Sn and Cu_6Sn_5 . At $\times 6000$ magnification, the IMC layer of Cu_3Sn was not clearly seen compared to Cu_6Sn_5 due to very thin layer. Figure 4.18 (a) show that the IMC layer form were a typical scallop type IMC layer. 1.0, 1.5 and 2.0 wt. % of Co addition changes the IMC layer morphology from scallop to planar to needle-like type of IMC layer. Figure 4.18 (a) also shows that there were several voids at IMC layer. The alloying addition of Co into the pure Sn-58Bi solder successfully lessen the voids presented at the IMC layer. Some flattening of IMC layer also could be observed at Sn-58Bi-1.0Co/Cu, Sn-58Bi-1.5Co/Cu and Sn-58Bi-2.0Co/Cu interface.

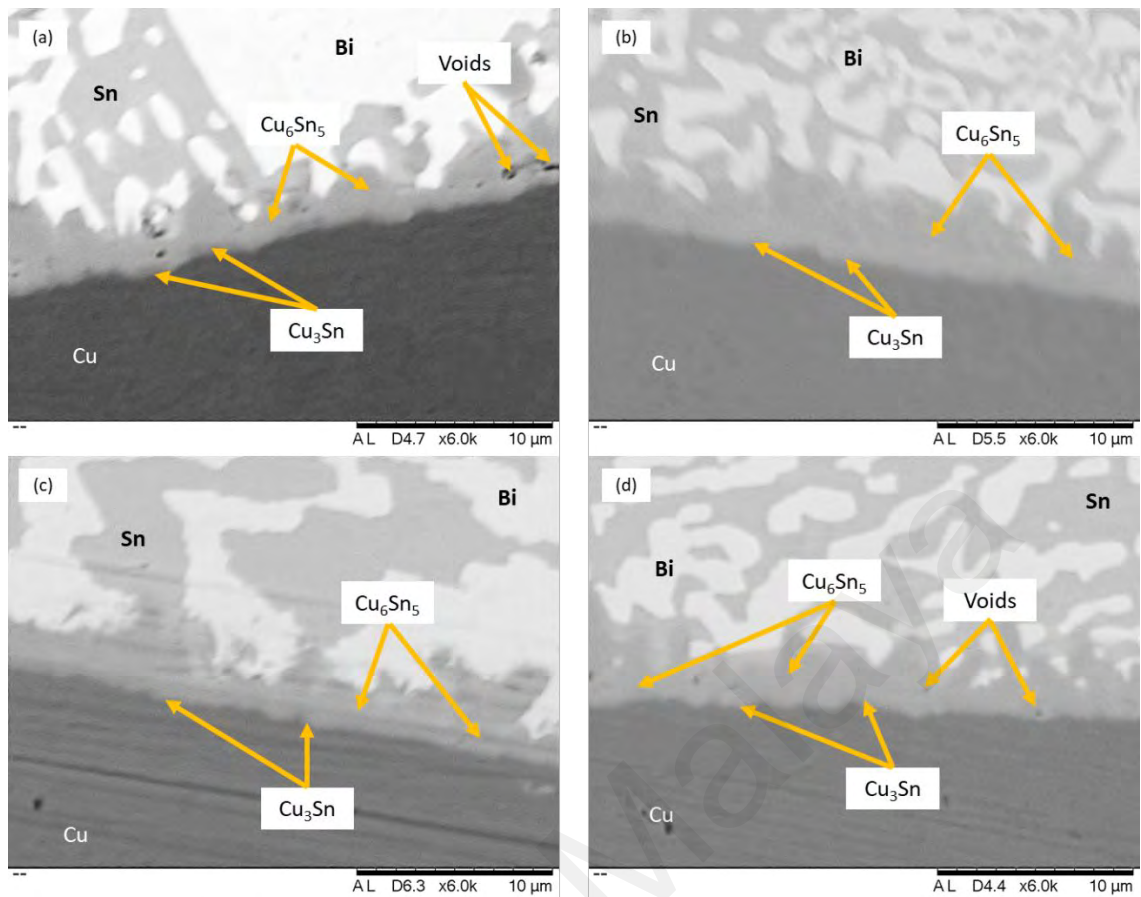


Figure 4.18: SEM images of (a) pure Sn-58Bi/Cu solder, (b) Sn-58Bi-1.0Co/Cu solder, (c) Sn-58Bi-1.5Co/Cu solder and (d) Sn-58Bi-2.0Co/Cu solder at 6000× magnification

To analyse the distribution of Co between the solders and Cu substrate, element mapping was conducted at the IMC layer area. Figure 4.19 shown the element mapping of Sn-58Bi-Co/Cu. Figure 4.19 shows that the IMC layer form was consist of Cu_3Sn and Cu_6Sn_5 where there were plenty of Cu and Sn element observed at the IMC layer. Figure 4.19 (b-d) show that Co particle was observed to be distributed all over the solder and Cu substrate. Cu particle also was observed to be presented at the solder but more concentrated at the IMC layer and Cu substrate. Figure 4.19 also confirm that the dark and white region of the solder were Sn-rich and Bi-rich phase region, respectively. Figure 4.19 (b) show an obvious needle-like type IMC layer while Figure 4.19 (c) and (d) shows nearly scallop to planar type IMC layer.

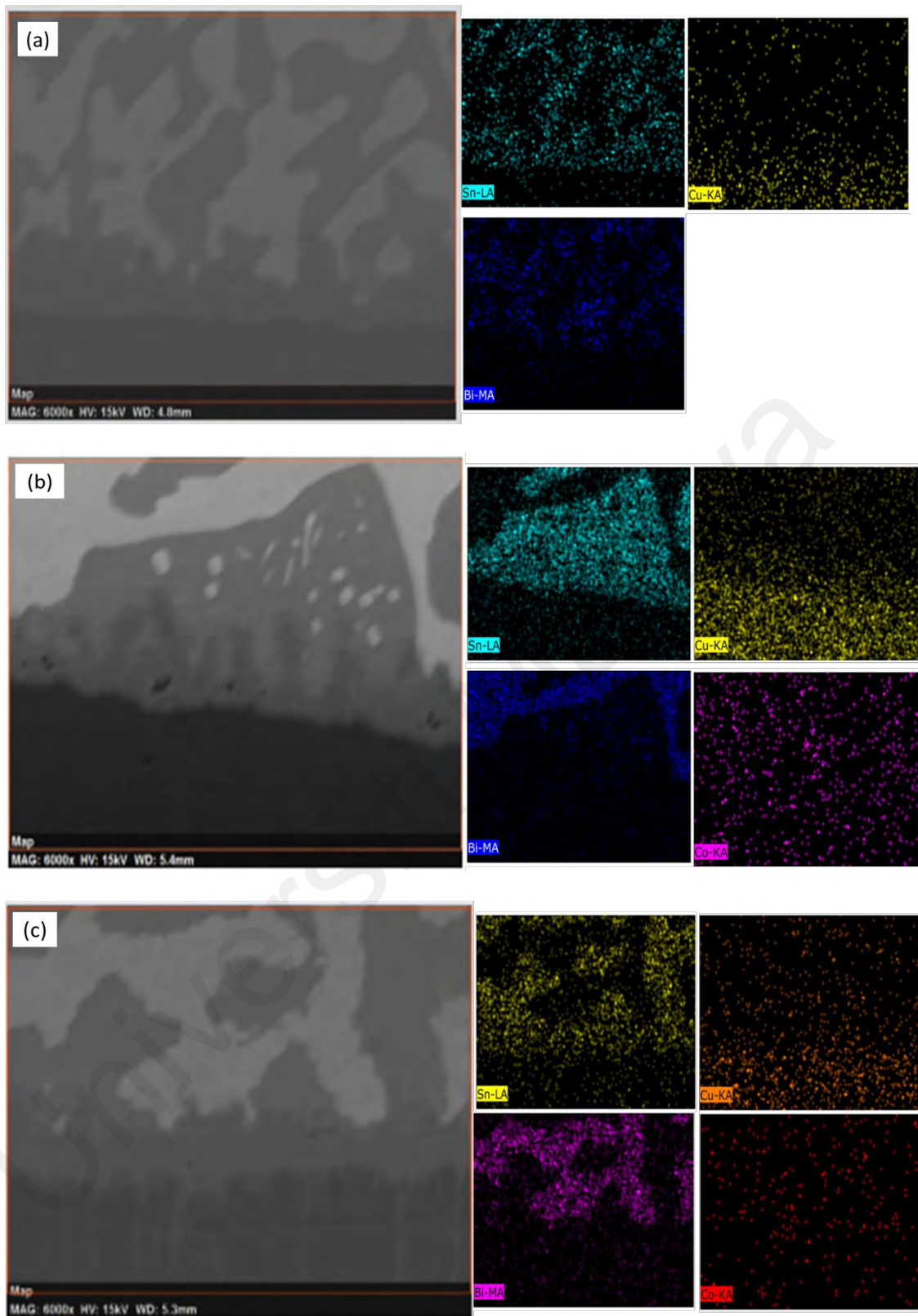


Figure 4.19: Element mapping of (a) pure Sn-58Bi/Cu, (b) Sn-58Bi-1.0Co/Cu, (c) Sn-58Bi-1.5Co/Cu and (d) Sn-58Bi-2.0Co/Cu solder joint

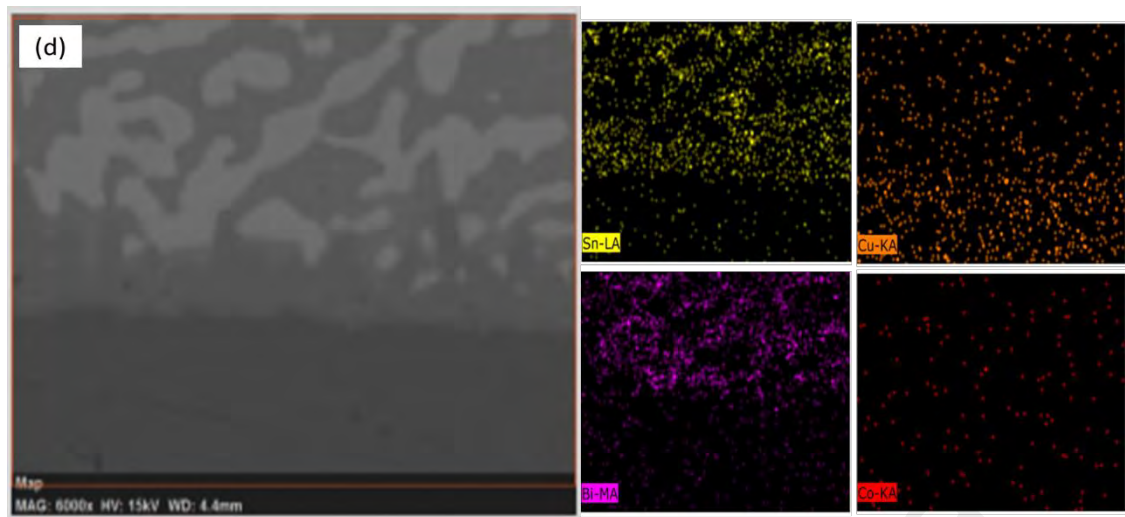


Figure 4.19, continued: Element mapping of (a) pure Sn-58Bi/Cu, (b) Sn-58Bi-1.0Co/Cu, (c) Sn-58Bi-1.5Co/Cu and (d) Sn-58Bi-2.0Co/Cu solder joint

Several SEM images of the intermetallic compound (IMC) layer forms at pure Sn-58Bi/Cu and Sn-58Bi-xCo/Cu ($x= 1.0, 1.5$ and 2.0 wt.%) solders were taken from 3 similar samples to calculate the IMC thickness layer of the solder and Cu substrate. Table 4.4 show the average IMC thickness of Sn-58Bi-Co with Cu substrate calculated from 12 SEM images. From Table 4.4, the alloying addition of 1.0, 1.5 and 2.0 wt. % of Co into Sn-58Bi solder caused the IMC layer thickness increase by $0.26 \mu\text{m}$, $0.21 \mu\text{m}$ and $0.23 \mu\text{m}$ compared to pure Sn-58Bi solder, respectively. The IMC layer increased due to flattening of the IMC layer.

Table 4.4: Average IMC thickness of Sn-58Bi-Co with Cu substrates

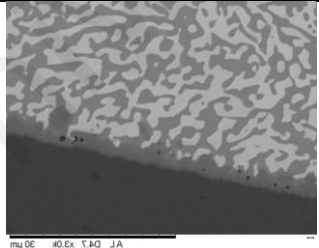
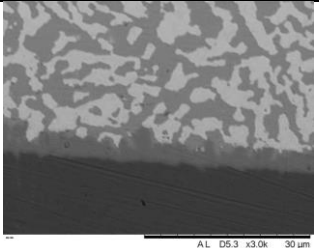
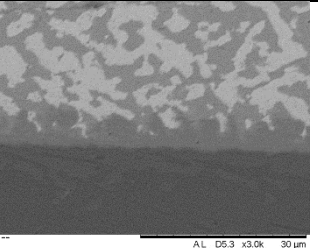
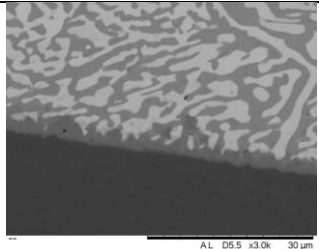
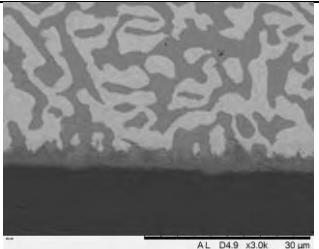
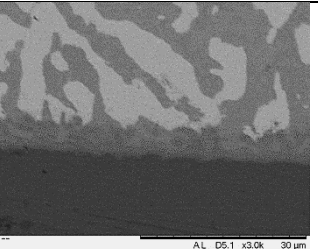
| Solder | Average IMC thickness (μm) |
|---------------|---|
| Pure Sn-58Bi | 3.37 ± 0.40 |
| Sn-58Bi-1.0Co | 3.63 ± 0.23 |
| Sn-58Bi-1.5Co | 3.58 ± 0.33 |
| Sn-58Bi-2.0Co | 3.60 ± 0.51 |

4.6.2 Thermal Aging Studies

The pure Sn-58Bi/Cu solder joint and Sn-58Bi-xCo/Cu ($x = 1.0, 1.5$ and 2.0 wt. %) solder joint were thermally aged at $80\text{ }^{\circ}\text{C}$. Sn-58Bi/Cu, Sn-58Bi-1.0Co/Cu and Sn-58Bi-2.0Co/Cu solder joints were thermally aged for 28 and 56 days while Sn-58Bi-1.5Co/Cu solder joint was thermally aged for 14, 28, 42, 56 and 70 days. Table 4.5 show the comparison of SEM images of pure Sn-58Bi/Cu and Sn-58Bi-xCo/Cu ($x = 1.0, 1.5$ and 2.0 wt. %) solder joint after thermal aging for 0, 28 and 56 day(s).

Based on Table 4.5, the increase in thermal aging duration shows IMC layer of Sn-58Bi-xCo/Cu ($x = 1.0, 1.5$ and 2.0 wt. %) solder joint of scallop-like type became flattening while the pure Sn-58Bi/Cu solder joint still show scallop-like type of IMC layer. All of solders Sn-rich and Bi-rich phase structures also become enlarged with the increase in aging duration except Sn-58Bi-1.5Co/Cu solder. However, the enlargement of Sn-58Bi-1.0Co/Cu and Sn-58Bi-2.0Co/Cu solders phases structures were higher compared to the pure Sn-58Bi solder joint.

Table 4.5: SEM images of pure Sn-58Bi/Cu and Sn-58Bi-Co/Cu solder joint after thermal aging for 0, 28 and 56 day(s).

| Solder | 0 day | 28 days | 56 days |
|---------------|---|--|---|
| Pure Sn-58Bi |  |  |  |
| Sn-58Bi-1.0Co |  |  |  |

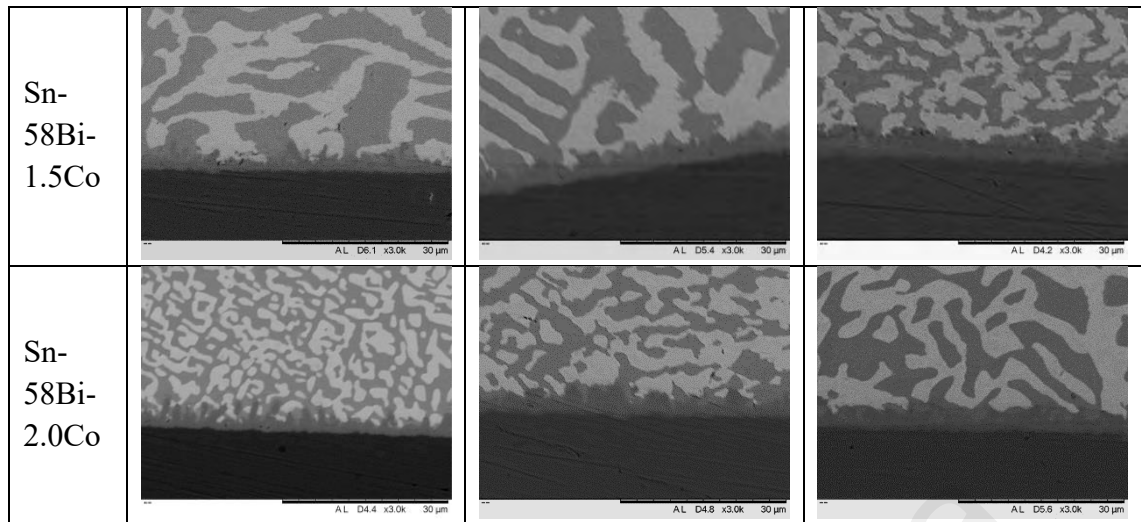


Figure 4.20 shown the average IMC layer thickness form at pure Sn-58Bi/Cu and Sn-58Bi-xCo/Cu ($x = 1.0, 1.5$ and 2.0 wt. %) solder joints thermally aged for 0, 28 and 56 day(s). After thermally aged for 28 days, all the average IMC thickness of the solder joints increased except for Sn-58Bi-1.0Co/Cu solder joint. However, after thermally aged for 56 days, the Sn-58Bi-1.0Co/Cu solder joint had the highest average IMC thickness solder joint. Sn-58Bi-1.0Co/Cu solder joint had the highest average IMC thickness at 0 day and 56 days of thermally aged. Both pure Sn-58Bi/Cu and Sn-58Bi-1.5Co/Cu solder joints show similar trend which show that when aging duration increased, the average IMC thickness increased. The average IMC thickness Sn-58Bi-2.0Co/Cu solder joint was the only IMC layer which show decreased in IMC thickness after thermally aged for 56 days. Thus, the amount of Co addition in the Sn-58Bi affect the IMC thickness before and after aged differently.

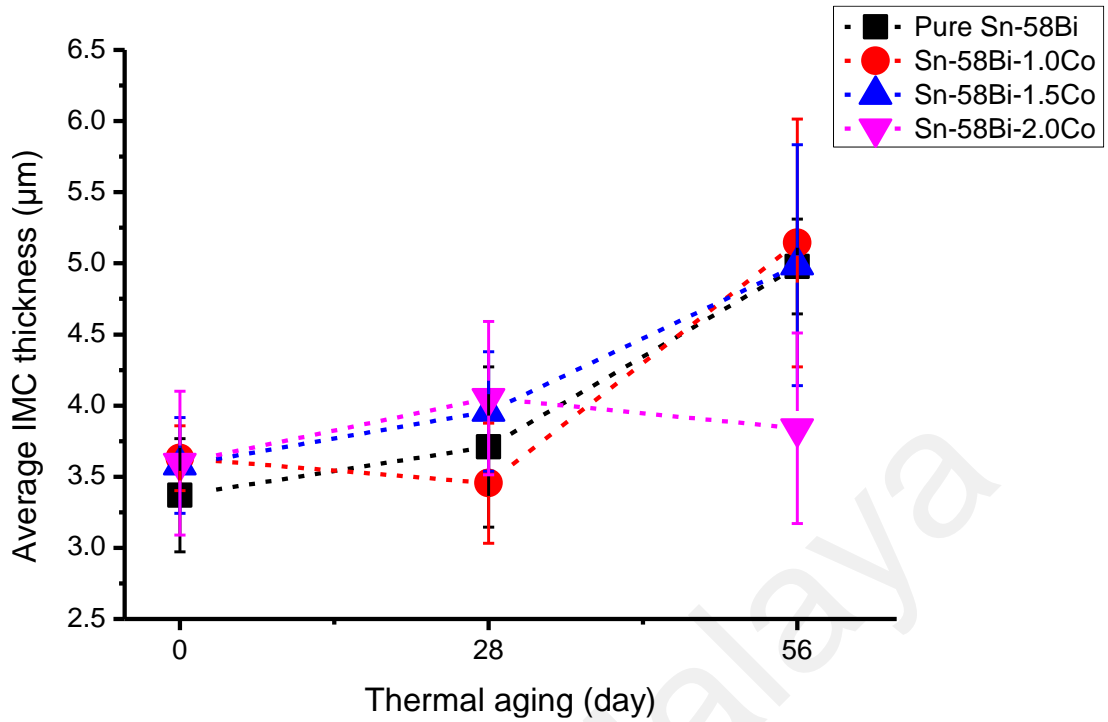


Figure 4.20: IMC thickness of pure Sn-58Bi/Cu and Sn-58Bi-Co/Cu solder joint after thermal aging for 0, 28, and 56 day(s)

The IMC thickness of Sn-58Bi-1.5Co/Cu solder joint was further observed in detailed by thermally aged at 80 °C. The aging duration was varied by 14 days until reach 70 days. Figure 4.21 show the IMC layer thickness form after thermally aged for 0, 14, 28, 42, 56 and 70 day(s). The IMC layer of Sn-58Bi-1.5Co/Cu solder joint before aged show that the IMC layer form was scallop-to-needle like type of IMC. However, after aging, the IMC layer form changes to be more scallop-like type and become flattening. Figure 4.21 (b), (d) and (e) observed obvious flattening of the IMC layers. After thermally aged for 70 days, the IMC layer become a little scallop-like type IMC again. Based on Figure 4.21, the Sn-rich and Bi-rich phases structure also started to shrink in size after 42 days of aging.

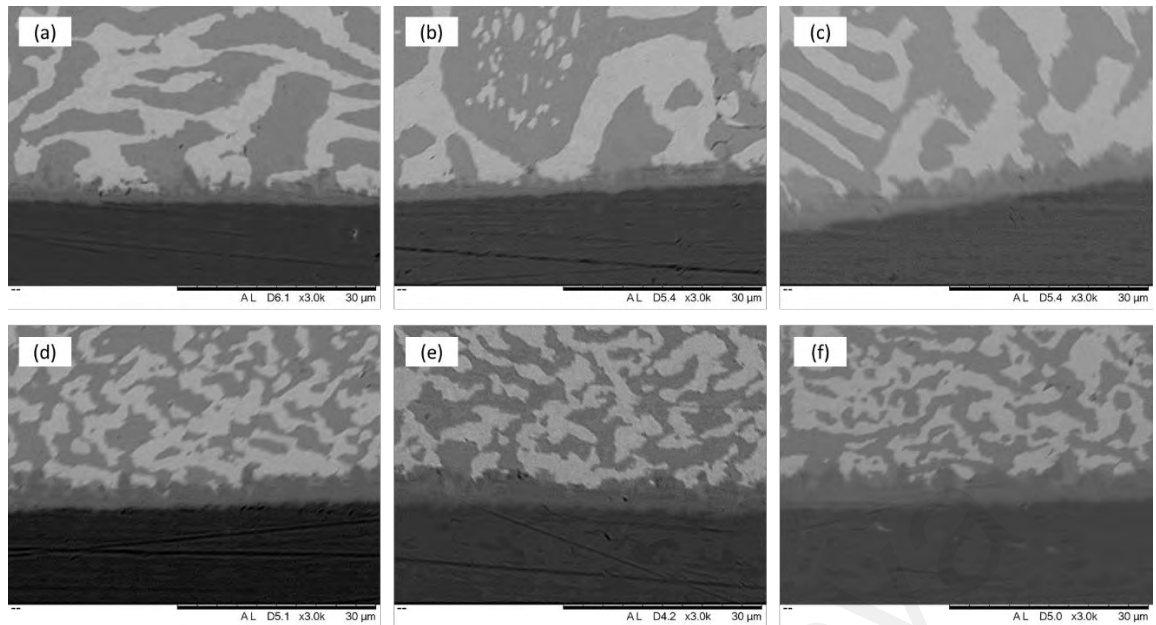


Figure 4.21: SEM images of Sn-58Bi-1.5Co/Cu solder joint after thermal aging for (a) 0, (b) 14, (c) 28, (d) 42, (e) 56 and (f) 70 day(s).

Figure 4.22 show the average IMC thickness of Sn-58Bi-1.5Co/Cu solder joint thermally aged for 0, 14, 28, 42, 56 and 70 day(s). After thermally aged for 14 days, the average IMC thickness of Sn-58Bi-1.5Co/Cu solder joint decrease by $0.32 \mu\text{m}$ compared to 0 day of thermal aging. Then, the average IMC thickness increased gradually from 14 until 56 days of thermal aging but started to decrease at 70 days of thermal aging. The average IMC thickness at 70 days of thermal aging decrease by $0.37 \mu\text{m}$ compared to 56 days of thermal aging. The decrease in the average IMC thickness may be related to the changes of the IMC layer form shown in Figure 4.21 (e) and (f). Thus, starting from 70 days of thermal aging, the IMC thickness started to stabilise.

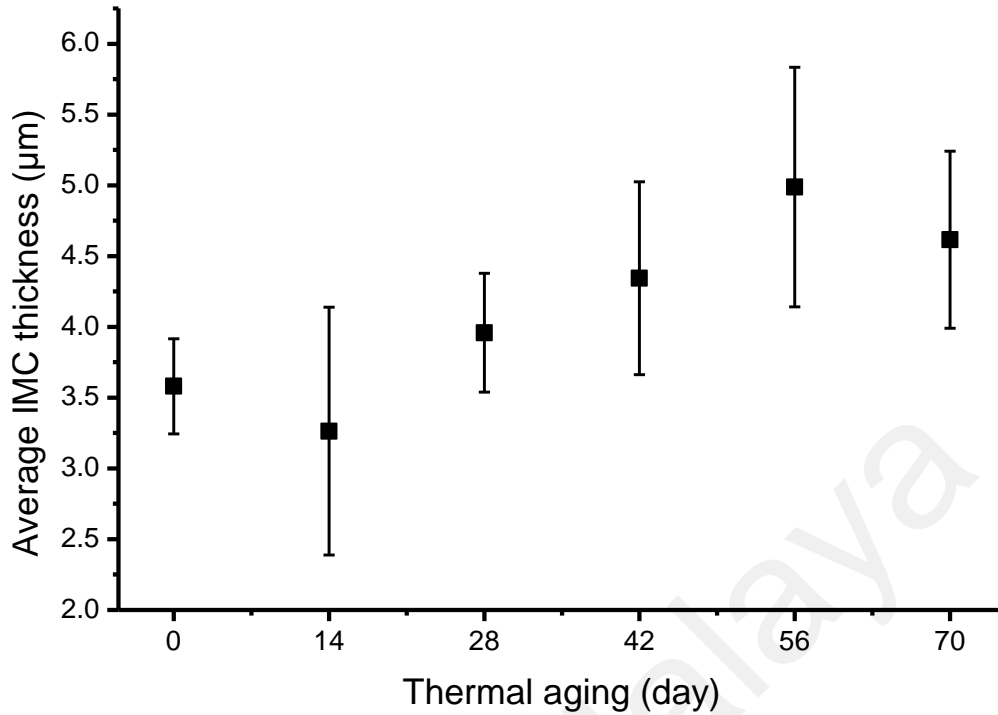


Figure 4.22: IMC thickness of Sn-58Bi-1.5Co after thermal aging for 0, 14, 28, 42, 56 and 70 day(s).

Then, to observe the distributions of Co particle in the Sn-58Bi-1.5Co/Cu solder joints during thermal aging, element mapping was conducted for 0, 28, 56 and 70 day(s) of thermal aging. Figure 4.23 show the element mapping of Sn-58Bi-1.5Co/Cu solder joint thermally aged for 0, 28, 56 and 70 day(s). The IMC layer was observed to be consist of Cu_3Sn and Cu_6Sn_5 where there were plenty of Cu and Sn element observed at the IMC layer. The dark and white region of the solder were also proven to be Sn-rich phase and Bi-rich phase, respectively. The Co particles was observed to be distributed all over the solder and substrate including at the solder joint. The present of Co observed to be decrease with increasing thermal aging duration until 56 days but started to increase a little at 70 days of thermal aging. These observations could be related to the average IMC thickness recorded in Figure 4.22.

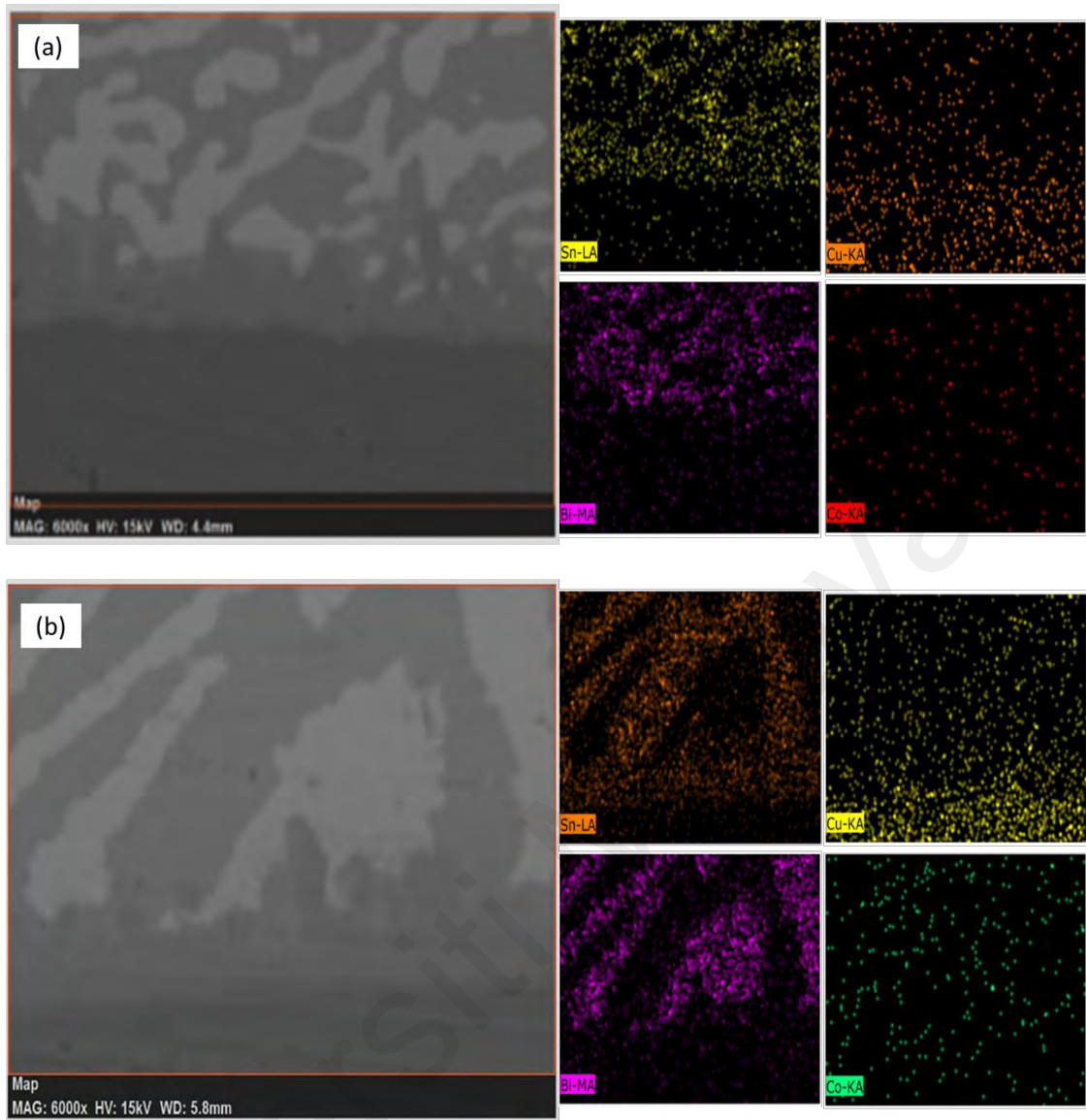


Figure 4.23: Element mapping of Sn-58Bi-1.5Co/Cu solder joint after thermal aging for (a) 0, (b) 28, (c) 56 and (d) 70 day(s).

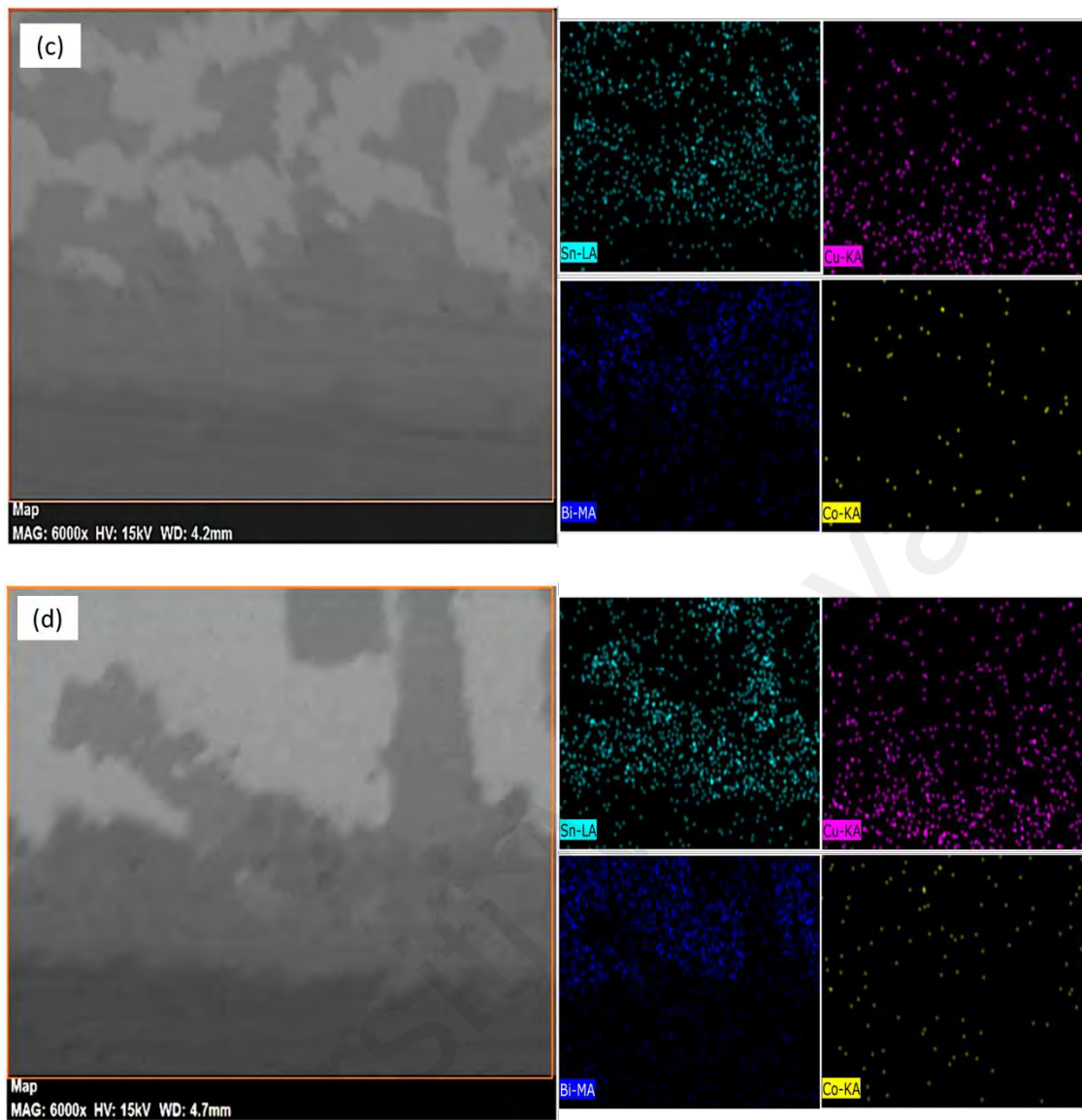


Figure 4.23, continued: Element mapping of Sn-58Bi-1.5Co/Cu solder joint after thermal aging for (a) 0, (b) 28, (c) 56 and (d) 70 day(s).

CHAPTER 5: CONCLUSION AND RECOMMENDATIONS

5.1 Conclusion

Co minor alloying addition into Sn-Bi solder using flux doping technique was successful. Co could be detected in all customised Sn-58Bi-xCo ($x = 1.0, 1.5$ and 2.0 wt. %) solders. $1.0, 1.5$ and 2.0 wt. % of alloying element of Co into Sn-58Bi solder does not changes the eutectic microstructure of SnBi solder. It was observed that Co particles distributed through the solder at both Sn-rich and Bi-rich phase. Sn-58Bi-1.5Co solder recorded the highest melting temperature which was 144.73 ± 1.24 °C. However, the melting temperature of Sn-58Bi-1.5Co solder only increased by 4.61 °C compared to pure Sn-58Bi solder melting temperature. The XRD plot of Sn-58Bi solder with alloying addition of Co show the matched with Co_3Sn_2 peak with orthorhombic and hexagonal crystal systems.

As for the tensile properties of Sn-58Bi solder, low strain rates result shows better tensile properties of pure Sn-58Bi solder. The elongation of Sn-58Bi solder decreased as strain rates and modulus of elasticity increased. Under the highest strain rate of 0.0025s^{-1} , very less necking could be observed at the pure Sn-58Bi solder tensile fractured surface. Then, the tensile properties of Sn-58Bi-xCo solders recorded that under 0.0005s^{-1} strain rate at room temperature, 1.5 wt. % of Co alloying addition into Sn-58Bi solder had the most optimum tensile properties and had the highest tensile strength. The tensile strength of Sn-58Bi-1.5Co solder was 60.29 ± 0.18 MPa. The fractography of all solder composition observed a necking phenomenon while Sn-58Bi-1.5Co solder show the lowest amount of crack near the tensile breaking region. 1.5 wt. % alloying addition of Co into Sn-58Bi solder improve the microhardness of the solder from 19.18 ± 0.52 HV to 19.52 ± 0.47 HV. These results in agreement with the resulted tensile strength of Sn-58Bi-1.5Co solder where in both mechanical test, Sn-58Bi-1.5Co recorded the highest values.

By alloying Co into Sn-58Bi/Cu solder joint, the appearance of voids at the intermetallic compound layer of pure Sn-58Bi/Cu solder joint decreased. 1.0, 1.5 and 2.0 wt. % of Co alloying addition changes the pure Sn-58Bi/Cu solder joint intermetallic compound layer from scallop type to needle-like to planar type of intermetallic compound layer. After thermally aged up to 56 days, the intermetallic compound layer of Sn-58Bi/Cu solder joint with the alloying addition of Co become flattening compared to the pure Sn-58Bi/Cu solder joint. Sn-58Bi-1.0Co/Cu solder joint and Sn-58Bi-2.0Co/Cu solder joint had the highest and lowest average intermetallic compound thickness after thermally aged for 56 days, respectively. Observation of intermetallic compound layer of Sn-58Bi-1.5Co/Cu solder joint growth after thermally aged up to 70 days show that the average intermetallic compound thickness continues to increase up to 56 days of aged and started to decrease after 70 days of aging. The intermetallic compound layer also become flattening with increasing thermal aging duration. The element mapping of the Sn-58Bi-xCo/Cu ($x = 1.0, 1.5$ and 2.0 wt. %) solder joints show that the Co particle was not only concentrated at the intermetallic compound layer but distributed thoroughly at the solder and substrate.

Therefore, the best composition which had the most optimised mechanical properties was Sn-58Bi-1.5Co solder alloy. The growth of intermetallic compound layer of Sn-58Bi-1.5Co/Cu solder joint also show a good performance.

5.2 Recommendations

Some recommendations for further studies of the research on microstructure and mechanical properties of Sn-Bi-Co low temperature solder alloy are as listed below:

1. Addition of the fourth minor alloying element could be considered. The fourth minor alloying element could enhance the modulus of elasticity and stabilised the growth of intermetallic compound layer of the solder joint.
2. New research on the flux used in the flux-doped technique could be developed to

match solder and improve the diffusion of Co particle into the solder. The flux also could be used during reflowing process of the solder joint.

3. Other technique used to dope Co into Sn-58Bi solder alloy could be considered.

The other available techniques are powder metallurgy method, metal casting routes and electrodeposition.

Universiti Malaya

REFERENCES

- Achari, A., Paruchuri, M. R., & Shanguan, D. (1999). Lead-free solder compositions. In: Google Patents.
- Alam, S. N., Jindal, N., & Naithani, N. (2019). Effect of addition of Cu on the properties of eutectic Sn-Bi solder alloy. *Materials Science-Poland*, 37(2), 212-224.
- Amares, S., Ervina Efzan, M. N., & Yap, T. C. (2014). Characterizations of physical properties of Sn-Bi solder alloy. In *Advanced Materials Research* (Vol. 845, pp. 261-265). Trans Tech Publications Ltd.
- Bashir, M. N., Haseeb, A., Rahman, A. Z. M. S., & Fazal, M. (2016). Effect of cobalt doping on the microstructure and tensile properties of lead free solder joint subjected to electromigration. *Journal of Materials Science & Technology*, 32(11), 1129-1136.
- Bi-Cu-Sn System (n.d.). Retrieved 3rd March 2023, from <https://www.metallurgy.nist.gov/phase/solder/bicusn.html>
- Bieler, T. R., & Lee, T. K. (2017). Lead-Free Solder. In *Reference Module in Materials Science and Materials Engineering*: Elsevier.
- Brittles, G., Mousavi, T., Grovenor, C. R. M., Aksoy, C., & Speller, S. C. (2015). Persistent current joints between technological superconductors. *Superconductor Science and Technology*, 28.
- Chen, X., Zhou, J., Xue, F., & Yao, Y. (2016). Mechanical deformation behavior and mechanism of Sn-58Bi solder alloys under different temperatures and strain rates. *Materials Science and Engineering: A*, 662, 251-257.
- Cheng, S., Huang, C.-M., & Pecht, M. (2017). A review of lead-free solders for electronics applications. *Microelectronics Reliability*, 75, 77-95.
- da Silva, V. C. E., de Gouveia, G. L., Reyes, R. A. V., Garcia, A., & Spinelli, J. E. (2019). Sn-Bi(-Ga) TIM Alloys: Microstructure, Tensile Properties, Wettability and Interfacial Reactions. *Journal of Electronic Materials*, 48(8), 4773-4788.
- Ding, M., Xing, W., Yu, X., Ma, L., Zuo, W., & Ji, Z. (2018). Effect of micro alumina particles additions on the interfacial behavior and mechanical properties of Sn-9Zn-1Al₂O₃ nanoparticles on low temperature wetting and soldering of 6061 aluminum alloys. *Journal of Alloys and Compounds*, 739, 481-488.
- Fan, J., Liu, Z., Zhai, H., Wang, X., Wang, Y., Li, Y., . . . Liu, J. (2020). Effect of Co content on the microstructure, spreadability, conductivity and corrosion resistance of Sn-0.7Cu alloy. *Microelectronics Reliability*, 107, 113615.
- Gancarz, T. (2016). The effect of aging temperature on the phenomena occurring at the interface of solder SnZn with Na on Cu substrate. *Materials Letters*, 171, 187-190.
- Gornakova, A., Straumal, B., Tsurekawa, S., Chang, L. S., & Nekrasov, A. (2009). Grain boundary wetting phase transformations in the Zn-Sn and Zn-In systems. *Reviews on Advanced Materials Science*, v.21, 18-26 (2009), 21.

- Haseeb, A. S. M. A., & Leng, T. S. (2011). Effects of Co nanoparticle addition to Sn–3.8Ag–0.7Cu solder on interfacial structure after reflow and ageing. *Intermetallics*, *19*(5), 707-712.
- Haseeb, A. S. M. A., & Leng, T. S. (2011). Effects of Co nanoparticle addition to Sn–3.8Ag–0.7Cu solder on interfacial structure after reflow and ageing. *Intermetallics*, *19*(5), 707-712.
- Hou, Z., Niu, T., Zhao, X., Liu, Y., & Yang, T. (2019). Intermetallic compounds formation and joints properties of electroplated Sn–Zn solder bumps with Cu substrates. *Journal of Materials Science: Materials in Electronics*, *30*(22), 20276-20284.
- Hu, J., Su, N., Wang, X., Yin, F., & Ouyang, X. (2022). Experimental investigation and thermodynamic calculation of the Co–Sn–Bi ternary system. *Calphad*, *77*, 102404.
- Hu, T., Li, Y., Chan, Y.-C., & Wu, F. (2015). Effect of nano Al₂O₃ particles doping on electromigration and mechanical properties of Sn–58Bi solder joints. *Microelectronics Reliability*, *55*(8), 1226-1233.
- Jiang, S.-l., Zhong, J.-f., Li, J.-y., Wang, R.-c., Peng, C.-q., & Cai, Z.-y. (2020). Influence of cobalt content on microstructure and corrosion performance of extruded Sn-9Zn solder alloys. *Journal of Central South University*, *27*(3), 711-720.
- Kang, H., Rajendran, S. H., & Jung, J. P. (2021). Low melting temperature Sn-Bi solder: Effect of alloying and nanoparticle addition on the microstructural, thermal, interfacial bonding, and mechanical characteristics. *Metals*, *11*(2), 364.
- Lee, H., Choi, K. S., Eom, Y. S., Bae, H. C., & Lee, J. H. (2016). Sn58Bi Solder Interconnection for Low-Temperature Flex-on-Flex Bonding. *Etri Journal*, *38*(6), 1163-1171.
- Leong, Y., & Haseeb, A. (2016). Soldering characteristics and mechanical properties of Sn-1.0 Ag-0.5 Cu solder with minor aluminum addition. *Materials*, *9*(7), 522.
- Li, Q., Wu, H., Xiong, M., Liu, F., Yue, X., & Yi, Y. (2020). *Effect of Er on microstructure and mechanical properties of Sn58bi based lead-free solder.*
- Li, Y., & Chan, Y. C. (2015). Effect of silver (Ag) nanoparticle size on the microstructure and mechanical properties of Sn58Bi–Ag composite solders. *Journal of Alloys and Compounds*, *645*, 566-576.
- Li, Y., Chan, Y., & Wu, F. (2016). *A comparison study of electromigration in In-48Sn solder interconnects with Cu and Au/Ni/Cu pads.* In 2016 International Conference on Electronics Packaging (ICEP). 689-692, doi: 10.1109/ICEP.2016.7486920.
- Li, Y., Lim, A. B., Luo, K., Chen, Z., Wu, F., & Chan, Y. (2016a). Phase segregation, interfacial intermetallic growth and electromigration-induced failure in Cu/In–48Sn/Cu solder interconnects under current stressing. *Journal of Alloys and Compounds*, *673*, 372-382.
- Liang, J., Dariavach, N., & Shanguan, D. (2007). Solidification Condition Effects on Microstructures and Creep Resistance of Sn3.8Ag0.7Cu Lead-Free Solder. *Metallurgical and Materials Transactions A-physical Metallurgy and Materials Science - METALL MATER TRANS A*, *38*, 1530-1538.

- Liu, J.-C., Wang, Z.-H., Xie, J.-Y., Ma, J.-S., Shi, Q.-Y., Zhang, G., & Sukanuma, K. (2016). Effects of intermetallic-forming element additions on microstructure and corrosion behavior of Sn–Zn solder alloys. *Corrosion Science*, *112*, 150-159.
- Liu, J.-C., Zhang, G., Wang, Z.-H., Ma, J.-S., & Sukanuma, K. (2015). Thermal property, wettability and interfacial characterization of novel Sn–Zn–Bi–In alloys as low-temperature lead-free solders. *Materials & Design*, *84*, 331-339.
- Liu, Y., & Tu, K. N. (2020). Low melting point solders based on Sn, Bi, and In elements. *Materials Today Advances*, *8*, 100115.
- Liu, Y., Fu, H., Sun, F., Zhang, H., Kong, X., & Xin, T. (2016). Microstructure and mechanical properties of as-reflowed Sn58Bi composite solder pastes. *Journal of Materials Processing Technology*, *238*, 290-296.
- Liu, Y., Xue, Y., Zhou, M., Cao, R., Zeng, X., Li, H., . . . Zhang, S. (2022). Effects of Sn–Ag–x leveling layers on the microstructure and mechanical properties of SnBi low-temperature solder joints. *Soldering & Surface Mount Technology*, *34*(3), 153-161.
- Maruya, Y., Hata, H., Shohji, I., & Koyama, S. (2017). *Fabrication of high melting point joint using Sn-57Bi-1Ag low temperature lead-free solder and gold-plated electrode*. In 2017 International Conference on Electronics Packaging (ICEP). 551-554, doi: 10.23919/ICEP.2017.7939445.
- Maruya, Y., Hata, H., Shohji, I., & Koyama, S. (2017). *Fabrication of high melting point joint using Sn-57Bi-1Ag low temperature lead-free solder and gold-plated electrode*. In 2017 International Conference on Electronics Packaging (ICEP).
- Mhd Noor, E. E., R, B., & J, E. (2018). A study on the effect of electromigration on solder alloy joint on copper with nickel surface finish. *Soldering & Surface Mount Technology*, *30*(1), 26-34.
- Mokhtari, O., & Nishikawa, H. (2013). *Coarsening of Bi phase and intermetallic layer thickness in Sn-58Bi-X (X= In and Ni) solder joint*. In 2013 14th International Conference on Electronic Packaging Technology. 250-253, doi: 10.1109/ICEPT.2013.6756465.
- Mokhtari, O., & Nishikawa, H. (2016). Correlation between microstructure and mechanical properties of Sn–Bi–X solders. *Materials Science and Engineering: A*, *651*, 831-839.
- Paixão, J. L., Gomes, L. F., Reyes, R. V., Garcia, A., Spinelli, J. E., & Silva, B. L. (2020). Microstructure characterization and tensile properties of directionally solidified Sn-52 wt% Bi-1wt% Sb and Sn-52wt% Bi-2wt% Sb alloys. *Materials Characterization*, *110*445.
- Qu, L., Ma, H., Zhao, H., Zhao, N., Kunwar, A., & Huang, M. (2013, 11-14 Aug. 2013). *The nucleation of Ag₃Sn and the growth orientation relationships with Cu₆Sn₅*. In 2013 14th International Conference on Electronic Packaging Technology, doi: 10.1109/ICEPT.2013.6756493.
- Ramos, L. S., Reyes, R. V., Gomes, L. F., Garcia, A., Spinelli, J. E., & Silva, B. L. (2020). The role of eutectic colonies in the tensile properties of a Sn–Zn eutectic solder alloy. *Materials Science and Engineering: A*, *776*, 138959.

- Ren, G., Wilding, I. J., & Collins, M. N. (2016). Alloying influences on low melt temperature SnZn and SnBi solder alloys for electronic interconnections. *Journal of Alloys and Compounds*, 665, 251-260.
- Ribas, M., Kumar, A., Kosuri, D., Rangaraju, R. R., Choudhury, P., Telu, S., & Sarkar, S. (2017). *Low temperature soldering using Sn-Bi alloys*. In Proceedings of the SMTA International Conference and Exhibition. Rosemont, Illinois. 201-206.
- Sakuyama, S., Akamatsu, T., Uenishi, K., & Sato, T. (2009). Effects of a Third Element on Microstructure and Mechanical Properties of Eutectic Sn–Bi Solder. *Transactions of The Japan Institute of Electronics Packaging*, 2(1), 98-103.
- Shrestha, T., Gollapudi, S., Charit, I., & Murty, K. L. (2014). Creep deformation behavior of Sn–Zn solder alloys. *Journal of materials science*, 49(5), 2127-2135.
- Silva, B. L., Garcia, A., & Spinelli, J. E. (2017). Complex eutectic growth and Bi precipitation in ternary Sn-Bi-Cu and Sn-Bi-Ag alloys. *Journal of Alloys and Compounds*, 691, 600-605.
- Silva, B. L., Xavier, M. G., Garcia, A., & Spinelli, J. E. (2017). Cu and Ag additions affecting the solidification microstructure and tensile properties of Sn-Bi lead-free solder alloys. *Materials Science and Engineering: A*, 705, 325-334.
- Skwarek, A., Illés, B., Witek, K., Hurtony, T., Tarasiuk, J., Wronski, S., & Synkiewicz, B. K. (2018). Reliability studies of InnoLot and SnBi joints soldered on DBC substrate. *Soldering & Surface Mount Technology*, 30(4), 205-212. doi:10.1108/SSMT-10-2017-0029
- Sujan, G. K., Haseeb, A. S. M. A., & Afifi, A. B. M. (2014). Effects of metallic nanoparticle doped flux on the interfacial intermetallic compounds between lead-free solder ball and copper substrate. *Materials Characterization*, 97, 199-209.
- Takao, H., Yamada, A., & Hasegawa, H. (2004). Mechanical properties and solder joint reliability of low-melting Sn-Bi-Cu lead free solder alloy. *R&D Review of Toyota CRDL*, 39(2), 457-462.
- Takeda, N., Habu, K., & Yamauchi, K. (2002). Solder alloy composition. In: Google Patents.
- Tay, S. L., Haseeb, A. S. M. A., & Rafie Johan, M. (2011). Addition of cobalt nanoparticles into Sn-3.8Ag-0.7Cu lead-free solder by paste mixing. *Soldering & Surface Mount Technology*, 23(1), 10-14.
- Tian, F., Li, C.-F., Zhou, M., & Liu, Z.-Q. (2018). The interfacial reaction between In-48Sn solder and polycrystalline Cu substrate during solid state aging. *Journal of Alloys and Compounds*, 740, 500-509.
- Tunthawiroon, P., & Kanlayasiri, K. (2019). Effects of Ag contents in Sn–xAg lead-free solders on microstructure, corrosion behavior and interfacial reaction with Cu substrate. *Transactions of Nonferrous Metals Society of China*, 29(8), 1696-1704.
- Vakanas, G., Minhó, O., Dimcic, B., Vanstreels, K., Vandecasteele, B., De Preter, I., . . . Beyne, E. (2015). Formation, processing and characterization of Co–Sn intermetallic compounds for potential integration in 3D interconnects. *Microelectronic Engineering*, 140, 72-80.

- Vianco, P., Rejent, J., & Grant, R. (2004). Development of Sn-based, low melting temperature Pb-free solder alloys. *Materials Transactions*, 45(3), 765-775.
- Wang, F., Chen, H., Huang, Y., Liu, L., & Zhang, Z. (2019). Recent progress on the development of Sn–Bi based low-temperature Pb-free solders. *Journal of Materials Science: Materials in Electronics*, 30(4), 3222-3243.
- Wang, F., Huang, Y., Zhang, Z., & Yan, C. (2017). Interfacial reaction and mechanical properties of Sn-Bi solder joints. *Materials*, 10(8), 920.
- Wang, F., Li, D., & Huang, Y. (2017). *The influence of adding different Sn-based solder coating into Sn-58Bi/Cu interface on the growth of intermetallic compound*. In 2017 18th International Conference on Electronic Packaging Technology (ICEPT). 266-270, doi: 10.1109/ICEPT.2017.8046452
- Wei, Y., Liu, Y., Zhang, L., & Zhao, X. (2021). Effects of endogenous Al and Zn phases on mechanical properties of Sn58Bi eutectic alloy. *Materials Characterization*, 175, 111089.
- Yakymovych, A., Mudry, S., Shtablavyi, I., & Ipsier, H. (2016). Effect of nano Co reinforcements on the structure of the Sn-3.0Ag-0.5Cu solder in liquid and after reflow solid states. *Materials Chemistry and Physics*, 181, 470-475.
- Yang, C.-h., Zhou, S., Lin, S.-k., & Nishikawa, H. (2019). A Computational Thermodynamics-Assisted Development of Sn-Bi-In-Ga Quaternary Alloys as Low-Temperature Pb-Free Solders. *Materials*, 12(4), 631.
- Yang, F., Zhang, L., Liu, Z.-q., Zhong, S.-j., Ma, J., & Bao, L. (2016). Properties and Microstructures of Sn-Bi-X Lead-Free Solders. *Advances in Materials Science and Engineering*, 2016, 9265195
- Yang, L., Zhou, W., Ma, Y., Li, X., Liang, Y., Cui, W., & Wu, P. (2016). Effects of Ni addition on mechanical properties of Sn58Bi solder alloy during solid-state aging. *Materials Science and Engineering: A*, 667, 368-375.
- Yang, L., Zhu, L., Zhang, Y., Zhou, S., Wang, G., Shen, S., & Shi, X. (2019). Microstructure, IMCs layer and reliability of Sn-58Bi solder joint reinforced by Mo nanoparticles during thermal cycling. *Materials Characterization*, 148, 280-291.
- Yang, T., Zhao, X., Xiong, Z., Tan, W., Wei, Y., Tan, C., . . . Wang, Y. (2020). Improvement of microstructure and tensile properties of Sn–Bi–Ag alloy by heterogeneous nucleation of β -Sn on Ag₃Sn. *Materials Science and Engineering: A*, 785, 139372.
- Yang, Y., Zhao, X., Ma, L., Zhang, F., Hu, Q., & Guo, F. (2016). *Effects of temperature and humidity on the formation of solder bead and microstructure in Sn-58Bi Solder joint*. In 2016 17th International Conference on Electronic Packaging Technology (ICEPT). 370-374, doi: 10.1109/ICEPT.2016.7583156.
- Zhou, S., Yang, C.-h., Shen, Y.-A., Lin, S.-k., & Nishikawa, H. (2019). The newly developed Sn–Bi–Zn alloy with a low melting point, improved ductility, and high ultimate tensile strength. *Materialia*, 6, 100300.

Zhu, W., Zhang, W., Zhou, W., & Wu, P. (2019). Improved microstructure and mechanical properties for SnBi solder alloy by addition of Cr powders. *Journal of Alloys and Compounds*, 789, 805-813.

Universiti Malaya